# CALIFORNIA INSTITUTE OF TECHNOLOGY

EARTHQUAKE ENGINEERING RESEARCH LABORATORY

# EARTHQUAKE RESPONSE OF STEEL BRACES AND BRACED STEEL FRAMES

BY

WENSHUI GAN

REPORT NO. EERL 96-06

PASADENA, CALIFORNIA

DECEMBER 1996

# Earthquake Response of Steel Braces and Braced Steel Frames

Thesis by

Wenshui Gan

In Partial Fulfillment of the Requirements

for the Degree of

Doctor of Philosophy

California Institute of Technology

Pasadena, California

1997

(Submitted December 6, 1996)

ii

To my parents

# Acknowledgements

My sincere gratitude goes to my advisor Professor John F. Hall for introducing me to some of the most interesting subjects in earthquake engineering and allowing me the latitude to explore different topics while providing generous support and invaluable advice. I also want to thank him for his assistance in many non-academic aspects during my stay at Caltech.

I wish to express my sincere appreciation to Professor James L. Beck, Professor Thomas K. Caughey, Professor Thomas H. Heaton and Professor Ares J. Rosakis for readily agreeing to be on the doctoral committee and for reviewing my dissertation.

The generous financial supports from Caltech, the Charles Lee Powell Foundation, and the Harold Hellwig Foundation are gratefully acknowledged.

I want to thank my friend and office mate Luojia Wang for providing some of the earthquake record data and arranging for computing resource in part of my dissertation research.

My special thanks go to my lovely wife, Shuling, for her many years of understanding, support and sacrifice. Finally, I want to thank my beautiful daughter, Janice Yutao, for bringing me the joy of being a father and for saving me from overwork by giving me frequent excuses to walk away from my desk in the final year of my study at Caltech.

This thesis was written in LaTeX running on the Linux Operating System.

# Abstract

This thesis consists of three parts. Chapter 2 deals with the dynamic buckling behavior of steel braces under cyclic axial end displacement. Braces under such a loading condition belong to a class of "acceleration magnifying" structural components, in which a small motion at the loading points can cause large internal acceleration and inertia. This member-level inertia is frequently ignored in current studies of braces and braced structures. This chapter shows that, under certain conditions, the inclusion of the member-level inertia can lead to brace behavior fundamentally different from that predicted by the quasi-static method. This result is to have significance in the correct use of the quasi-static, pseudo-dynamic and static condensation methods in the simulation of braces or braced structures under dynamic loading. The strain magnitude and distribution in the braces are also studied in this chapter.

Chapter 3 examines the effect of column uplift on the earthquake response of braced steel frames and explores the feasibility of flexible column-base anchoring. It is found that fully anchored braced-bay columns can induce extremely large internal forces in the braced-bay members and their connections, thus increasing the risk of failures observed in recent earthquakes. Flexible braced-bay column anchoring can significantly reduce the braced bay member force, but at the same time also introduces large story drift and column uplift. The pounding of an uplifting column with its support can result in very high compressive axial force.

Chapter 4 conducts a comparative study on the effectiveness of a proposed non-buckling bracing system and several conventional bracing systems. The non-buckling bracing system eliminates buckling and thus can be composed of small individual braces distributed widely in a structure to reduce bracing force concentration and increase redundancy. The elimination of buckling results in a significantly more effective bracing system compared with the conventional bracing systems. Among the conventional bracing systems, bracing

vi

configurations and end conditions for the bracing members affect the effectiveness.

The studies in Chapter 3 and Chapter 4 also indicate that code-designed conventionally braced steel frames can experience unacceptably severe response under the strong ground motions recorded during the recent Northridge and Kobe earthquakes.

# Table of Contents

viii

ix

# List of Figures

xv

# List of Tables

# Chapter 1

# Introduction

Braced frames are often used in steel structures to increase lateral stiffness and reduce drift under such lateral loads as caused by winds and earthquakes. Frame structures with conventional bracing systems have high elastic strength and small-displacement stiffness. However, in seismically active regions, it is common practice to allow inelastic deformation in building structures during a strong earthquake. Bracing members, which give high stiffness to a frame structure, are especially susceptible to inelastic deformation under horizontal earthquake loading. Although the inelastic deformation of a brace provides a means of energy dissipation, it has long been recognized that, under cyclic loading during an earthquake, the energy dissipation and load resisting abilities of the brace can be successively reduced with each load reversal. This reduction, or deterioration, of the energy dissipation and load resisting abilities can seriously impair the functioning of the brace and has been the focus of many experimental and analytical studies at the member level as well as at the structure level.

At the member level, most of the studies have focused on the quasi-static hysteretic force-displacement relationship and its degradation under cyclic end displacement. Earthquake damage surveys [1, 2] and laboratory studies [3–8] have shown that local buckling and rupture, together with connection failure, are the primary modes of brace failures. Large axial strain causes local buckling, which in turn leads to rupture. However, knowledge of the strain magnitude and distribution in bracing members under cyclic end displacement is still very incomplete.

There also have been results from shaking table and pseudo dynamic tests of structures

involving braces. Comparison of the two methods [6, 9] shows that they can give different responses. Strain rate effect has been identified as one of the possible factors that contributes to the differences. Another possible factor that has received little attention is the member-level inertia effect that is not modeled in the pseudo-dynamic testing. This is especially true for a class of structural members termed "inertia magnifying" in which a small motion at the loading point can cause large internal acceleration and hence large inertia in the members. This is what happens in a brace during buckling, and so internal inertia may have significant effect on the dynamic response of braces. However, including internal inertia of braces is impractical in pseudo dynamic testing of braced structures due to the large number of actuators and sensors required. An estimation of the member level inertia effect would facilitate more accurate interpretation of the test results.

In the dynamic analysis of braced structures, including the member level inertia requires the use of mass-containing internal degrees of freedom along each member. Internal degrees of freedom without mass have been employed to accurately compute the nonlinear force-deflection behavior of braces [10], and such degrees of freedom can be condensed out [11] to provide an efficient solution procedure. However, this technique only applies when the effect of internal inertia is small; otherwise the mass of the internal degrees of freedom must be retained, and the analysis becomes more costly. How the inertia affects the response of a brace, and under what conditions static condensation is applicable, along with the distribution and magnitude of strains in the brace are the subjects of study in Chapter 2.

Damage to braced steel frame structures during the 1994 Northridge earthquake and the 1995 Hyogo-Ken Nanbu (Kobe) earthquake shows that heavy bracing can result in considerable force in the braced bay columns and baseplates. During the Northridge earthquake, for example, dramatic failures were observed in the X-braced perimeter frames of the four-story Oviatt Library at the California State University, Northridge campus [2]. Many of the heavy baseplates fractured across the width and through the thickness. In addition to the baseplate fractures, horizontal cracks were also observed along the welds connecting column flanges to the baseplates.

The lateral force resistance of the Oviatt Library building was provided mainly by the braced perimeter frames. The braced frames had a height to bay-width ratio of about 4.0 and had relatively strong braces. It bas been suggested [2] that the heavy floor area combined with small gravity load in the braced frames, and relatively strong bracing members in a small number of braced bays with large height-to-width ratio might have caused large uplift force in the braced bay columns and contributed to the failures.

The damage in the Ashiyahama Seaside Town mega-frame apartment buildings during the 1995 Kobe earthquake also demonstrated the exceedingly large magnitude of member force in braced frames [12, 13]. These buildings, with heights ranging from 14 stories to 29 stories and a footprint approximately 30 meters by 12 meters, consisted of modular blocks of apartments supported by steel truss mega-frames. The mega-frames were composed of two braced towers and transfer trusses. Each tower had a plan dimension of approximately 2.5 meters (longitudinal direction) and 9.5 meters (width direction). The towers were each composed of eight columns: four exterior box columns ($500 \times 500 \times 50$ mm in the first story) and four interior H-columns. After the earthquake, tension failures were observed in many of the box columns.

These failures underscore the danger and difficulty associated with designing structures whose lateral resistance is provided by a relatively small number of braced bays. In light of the failures, the idea of allowing column uplift in the braced bays has been floating around among some practicing engineers. Chapter 3 examines the effect of column uplift and explores the feasibility of flexible column-base anchoring.

The buckling and the subsequent deterioration of conventional braces is one of the major shortcomings of concentrically braced steel frame structures. Small braces are especially susceptible to such shortcomings. However, as mentioned above, strong braces can result in large braced bay member force and increase the risk of failures in the braced bay members and their connections. Since buckling is the cause for brace deterioration, a non-buckling bracing system is proposed in Chapter 4 in an attempt to solve this dilemma. The proposed bracing system eliminates the possibility of brace buckling and the associated deterioration,

thus has a stable hysteretic characteristics and a more even distribution of strain along the length of the brace.

The effectiveness of a bracing system is affected by a number of factors, including the configuration of the bracing system and the end conditions of individual bracing members in the system. The response of braced frame structures under earthquakes has been the subject of many experimental and analytical studies [4–6, 8, 14–20]. These studies are conducted under different conditions and, in most cases, using different structures. It is therefore difficult to compare the effectiveness of different bracing systems. Chapter 4 makes a systematic comparison study of the effectiveness of a steel frame structures with the same basic configuration but different bracing systems, including the proposed non-buckling bracing system.

# Chapter 2

# Individual Bracing Members

## 2.1   General

This chapter deals with the hysteretic behavior of individual steel braces under imposed cyclic axial end displacement, with emphasis on the brace deformation and the effect of internal inertia. Section 2.2 outlines the problem and the method of analysis. Sections 2.3 and 2.4 examine the quasi-static and dynamic hysteretic behaviors of individual steel braces.

## 2.2   Outline of Problem and Analysis

It is common practice to use static condensation at the member level to eliminate the internal degrees of freedom from the global equations in the dynamic analysis of large structures. It is also common practice to ignore the internal inertia of members in pseudo-dynamic testing of structures under seismic loading. In most cases, the error introduced by this type of approximation is insignificant. But for a class of structural members termed "acceleration magnifying," in which a small motion at the loading point can cause large internal acceleration, these techniques may be problematic because of the large inertia force associated with the acceleration. Braces that buckle under axial load exhibit such a characteristic and are the subject of study in this chapter. Explicit dynamic analysis will be used, and the results are compared with those from quasi-static analysis. Another purpose of this chapter is to study the deformation in the braces, the knowledge of which is necessary to understand the failure of the braces.

| Brace | Length (m) | Cross-Sectional Area (m$^2$) | Slenderness Ratio $Kl/r$ | |
|---|---|---|---|---|
| | | | Pin-ended | Clamp-ended |
| □4×4×1/2 | 5.6 | 0.0045 | 153 | 76 |
| □6×6×1/2 | 5.6 | 0.0071 | 98 | 49 |
| □8×8×1/2 | 5.6 | 0.0097 | 72 | 36 |
| □12×12×1/2 | 5.6 | 0.0148 | 47 | 23 |

Table 2.1: Summary of brace geometry.

The study considers square tube steel braces of four different sizes summarized in Table 2.1. The length of all braces is 5.6 meters, which approximately corresponds to the length of a chevron brace extending from a beam-to-column joint to the mid-span of the beam above in a frame with story height of 3.5 m and bay width of 9.8 m. Pinned-pinned and clamped-clamped end conditions are considered for braces of each size. These should bound the end conditions found in actual structures. The slenderness ratios $Kl/r$ for braces with the four cross-sections corresponding to the length are 153, 98, 72 and 47 for pinned-pinned end condition, and 76, 49, 36 and 23 for clamped-clamped end condition, respectively. The yield stress and ultimate stress of the material are taken to be 345 MPa and 448 MPa respectively. For the sake of programming convenience the cross-sections are considered perfectly square and the roundness of the corners is neglected.

The braces are first subjected to monotonic end compression to study the initial buckling and post-buckling behaviors. Only quasi-static analysis is performed for the monotonic end compression. The effect of eccentricity is also studied for braces with pinned ends under such compression. The quasi-static response of the braces under cyclic axial end displacement shown in Figure 2.1 is considered next, which is followed by dynamic analysis under the same cyclic end displacement scaled to different frequencies. The quasi-static and dynamic responses are compared to study the effect of the internal inertia. In all cases a brace is assumed to be positioned horizontally and is initially deflected by its own weight. The

imposed axial end displacement is applied at one end of the braces as shown in Figure 2.2. As a necessity, the mass of a brace is included in the dynamic analysis.

The monotonic axial end compression is applied in steps until it reaches the maximum end displacement of 0.06 meters. The sequence of the cyclic end displacement is comprised of several sinusoid cycles with ramped amplitudes at the beginning and the end, as shown in Figure 2.1. The displacement is intended to simulate the peak cycles in typical response of a structure during an earthquake. In the quasi-static analysis, the frequency of the displacement cycles is of no significance, and the time acts only as a loading parameter. In the dynamic analysis, the time is scaled to achieve displacement histories with different frequencies. The end displacement amplitude of 0.06 m corresponds to approximately 2.1% story drift for a frame with the chevron bracing system mentioned above and 1.1% the length of the braces.
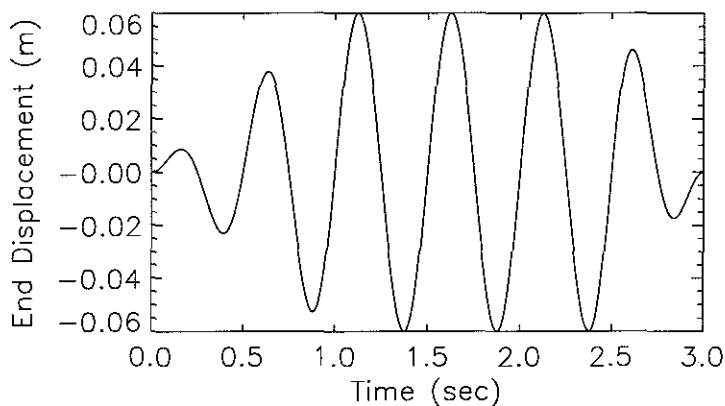
Figure 2.1: Cyclic axial displacement that is imposed on one end of the braces. In dynamic analysis, the time is scaled to achieve displacement histories of different frequencies.

Many analytical methods have been developed to model the cyclic behavior of steel braces in the past decades. These methods vary in accuracy and computational complexity and can be divided into three general categories: physical models, phenomenological models and finite element models. A review of these models can be found in [15].

The phenomenological models try to mimic the observed hysteresis loops using simple

rules derived from experimental results. The use of the models requires a large number of empirical parameters and the accuracy is not satisfactory.

The physical models are comprised of beam segments connected with one or more plastic hinges [10, 21–24]. The plastic hinges usually have an elasto-perfectly plastic moment-curvature relationship. The effect of the axial force on the moment capacity of the plastic hinges is taken into account through an empirical axial force-moment interaction equation. The beam segments between the hinges either allow elastic bending or have infinite flexural stiffness and are capable of elastic and plastic axial deformation. These models require fewer input parameters and yield better accuracy than the phenomenological models. Neither models provide details about the deformation and yielding process in the braces.

This study uses the fiber type finite element model presented in [10]. This model divides a brace into sub-segments along its length and fibers over its cross-section. It employs a realistic hysteretic stress-strain law and includes the effect of large displacement, strain hardening, gradual spread of yielding and proper coupling of the axial and flexural yielding. A summary of this model is included in Appendix A on page 140.

The computer program used in the analysis was originally designed for problems with specified load, not for situations involving specified displacement. To circumvent this limitation, an auxiliary elastic spring with large stiffness (relative to that of the brace) is attached to one end of the brace and a force $F$ is applied to cause the desired end displacement, as illustrated in Figure 2.2. The force $F$ required to generate an end displacement of $\Delta$ is

$$F = F_b + K_s\Delta = (\frac{F_b}{\Delta} + K_s)\Delta \qquad (2.1)$$

where $F_b$ is the axial force in the brace, $K_s$ is the stiffness of the auxiliary spring. Since $|F_b/\Delta| \leq K_b \ll K_s$, where $K_b$ is the initial axial stiffness of the brace, $F$ can be approximated by

$$F = K_s\Delta \qquad (2.2)$$

thus converting a problem with specified displacement into one with specified load.

9



(a) Pinned Ends



(b) Clamped Ends
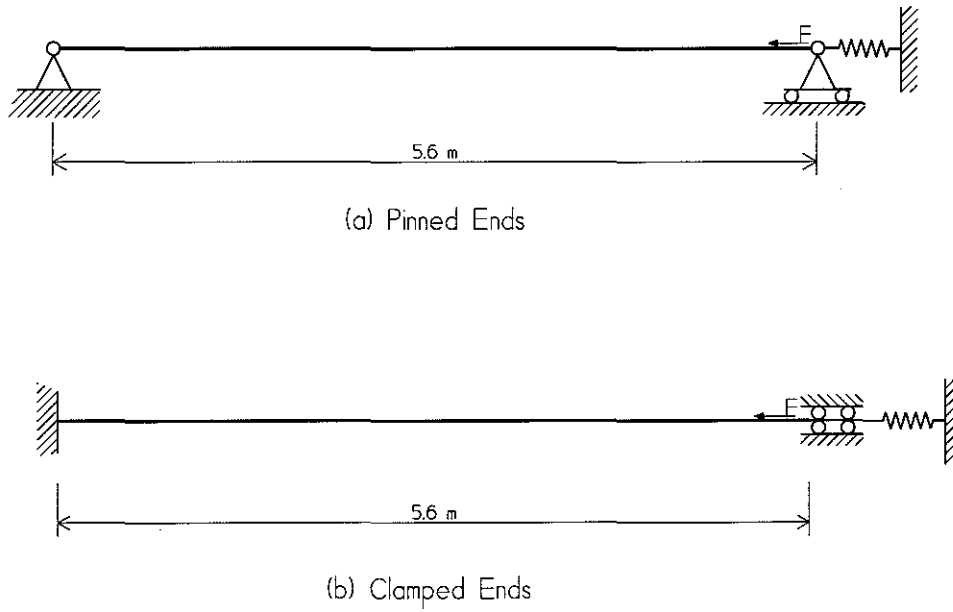
**Figure 2.2**: Analytic models for braces subjected to end displacement. Each brace is divided into 56 sub-elements over its length, and each sub-element is divided into fibers over the cross-section.
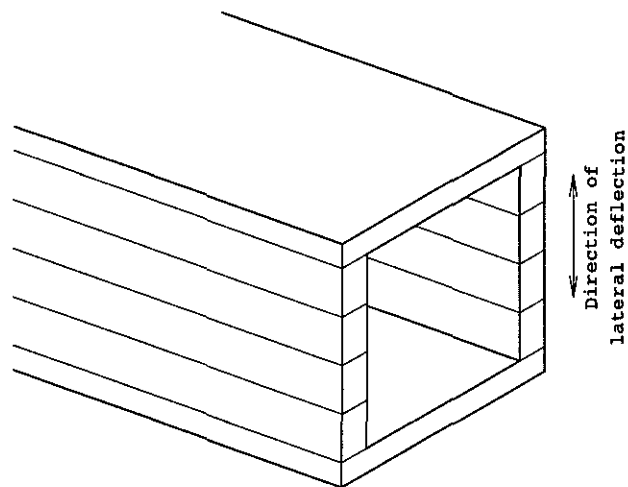


**Figure 2.3**: Fiber representation of a □-section brace for planar bending.

In applying the fiber element model, the braces are divided into 56 sub-elements, and each sub-element is divided into fibers over the cross-section as shown in Figure 2.3. The large number of sub-elements, which is far more than necessary to represent the load-displacement behavior of the braces [25], is adopted here to accurately capture the detailed deformation along the braces. The axial stress-strain rule for a fiber, as shown in Figure A.3 on page 148, includes strain hardening and Bauschinger effect. Initial residual stress is not considered here. The main aspects of the fiber element model and the numerical procedures are summarized in Appendix A on page 140, and more detailed information can be found in [11,26].

## 2.3    Quasi Static Behavior

This section focuses on the quasi-static behavior of the braces listed in Table 2.1 under monotonic and cyclic axial end displacements. Pinned-pinned and clamped-clamped end conditions are considered for braces of each size. Loading eccentricity is also considered for braces with pinned ends under monotonic end compression.

### 2.3.1    Braces Under Monotonic Compression

The braces are subjected to monotonically increasing compression at one end until the displacement reaches 0.06 m. Pin-ended and clamp-ended braces without eccentricity are first considered, followed by pin-ended braces with eccentricity. The incremental steps are adjusted to capture the load-displacement path accurately. This usually means that the steps are smaller in the vicinity along the path where initial buckling occurs.

**Braces Without Eccentricity**

Figures 2.4 to 2.7 show the loading curves for the braces with pinned ends, and Figures 2.9 to 2.12 show the same curves for braces with clamped ends. For all braces, the (absolute) axial force drops off after reaching its peak at a compression displacement between 0.5 cm

and 1.0 cm. This is different from the post-buckling behavior of linearly elastic braces whose axial force always increases with the end displacement. The cause that leads to this drop is the yielding of the braces. The largest fiber stress (or strain) occurs at mid-span in the outer-most fiber of a brace. The correlation of the drop in axial force and the occurrence of yielding can be seen clearly by comparing Figure 2.4 with Figure 2.8, in which the axial force is plotted against the mid-span top fiber strain of the □ 4 × 4 × 1/2 brace. The axial force starts to drop after the fiber strain reaches the yielding strain of 0.00154. Plots for other braces show similar correlation.
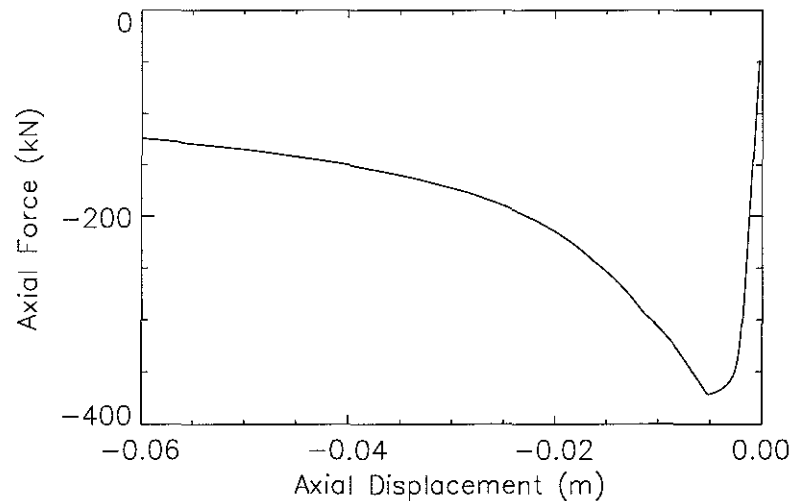


**Figure 2.4**: Loading curve for a □ 4 × 4 × 1/2 brace with pinned ends under monotonic end compression.

Tables 2.2 and 2.3 list the axial force capacities of the braces computed according to different criteria: the Euler critical buckling load, the uniform yield load, and the computed peak axial load. The Euler critical buckling load is calculated from

$$P_{cr} = \frac{\pi^2 EI}{L^2} \tag{2.3}$$

12
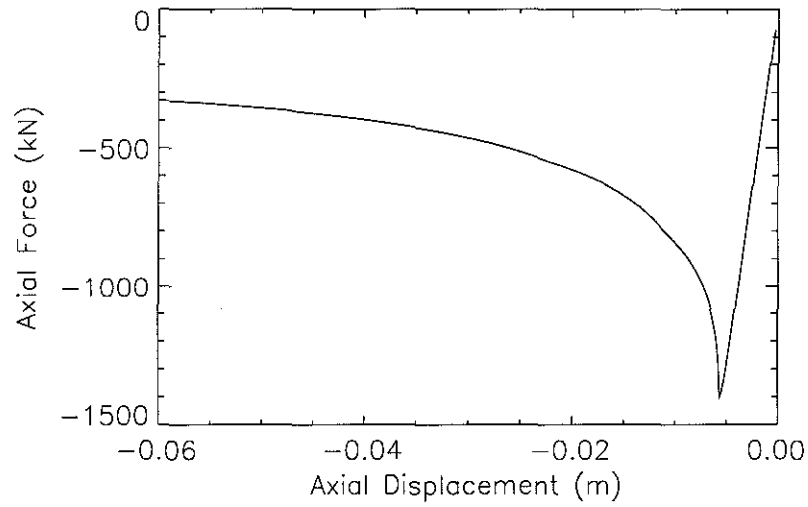


**Figure 2.5**: Loading curve for a □ 6 × 6 × 1/2 brace with pinned ends under monotonic end displacement.
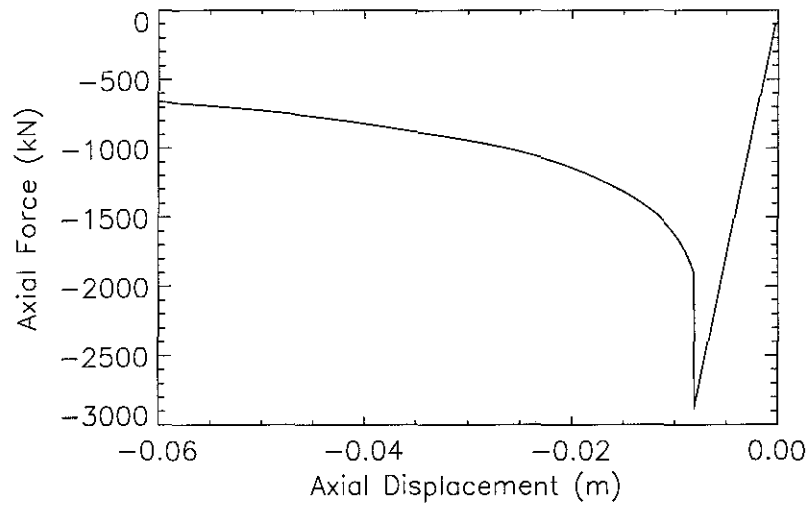


**Figure 2.6**: Loading curve for a □ 8 × 8 × 1/2 brace with pinned ends under monotonic end compression.
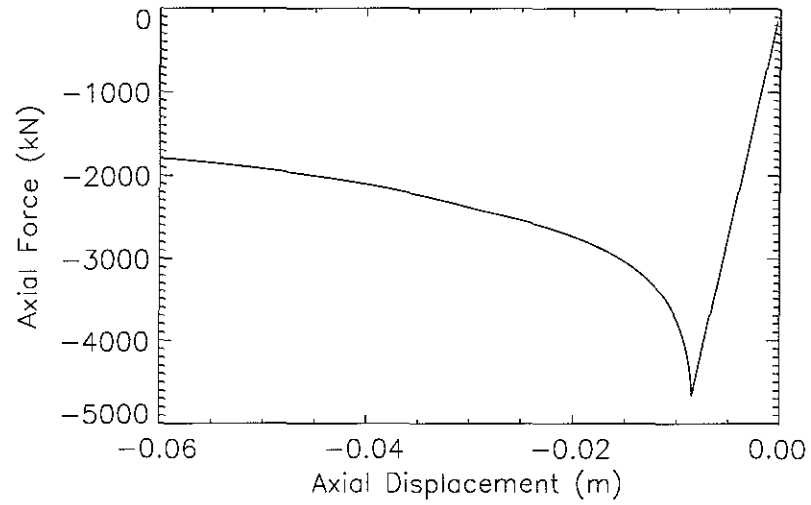
**Figure 2.7**: Loading curve for a □ 12 × 12 × 1/2 brace with pinned ends under monotonic end compression.
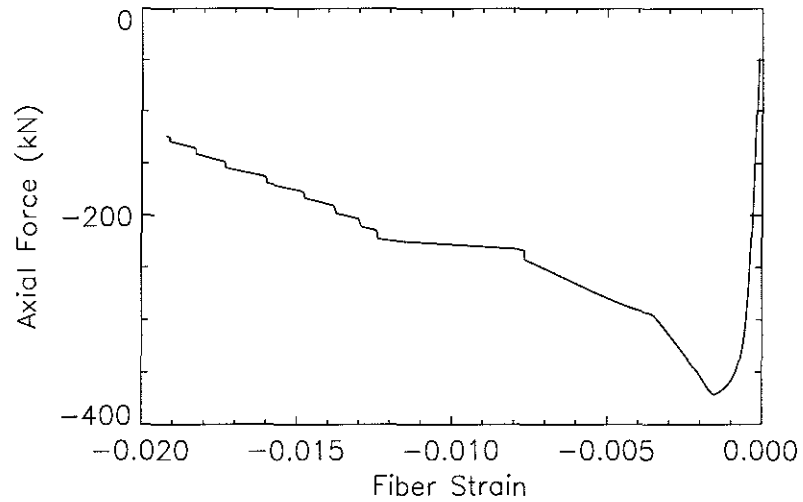


**Figure 2.8**: Axial force versus mid-span top fiber strain curve for a □ 4×4×1/2 brace with pinned ends under monotonic end compression.
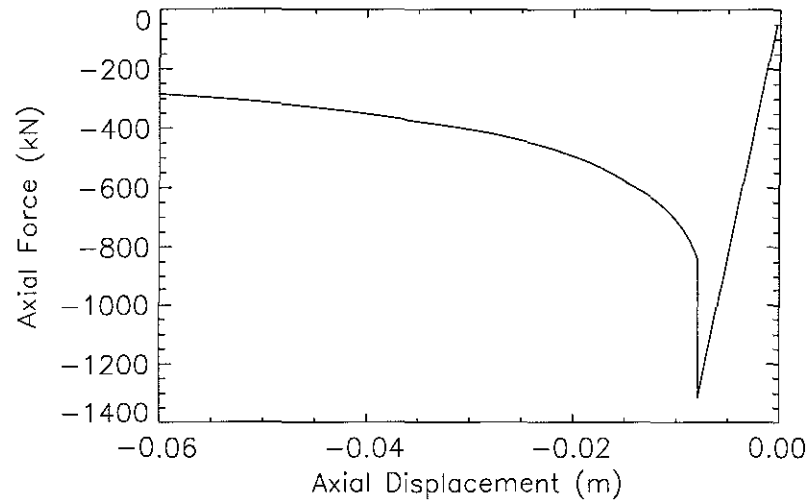
**Figure 2.9**: Loading curve for a □ 4 × 4 × 1/2 brace with clamped ends under monotonic end compression.
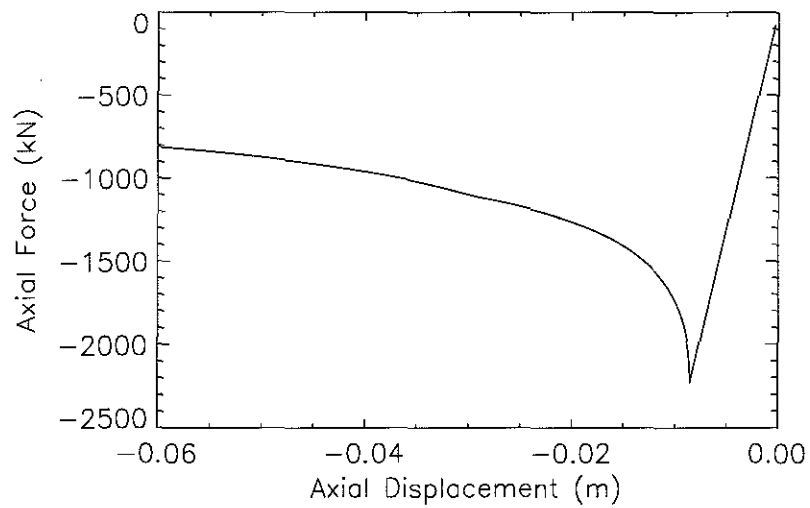


**Figure 2.10**: Loading curve for a □ 6 × 6 × 1/2 brace with clamped ends under monotonic end compression.
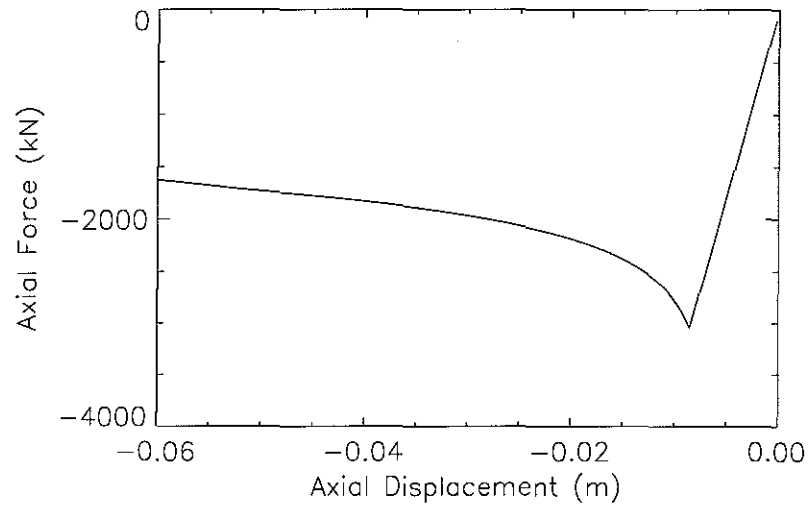
**Figure 2.11**: Loading curve for a □ 8×8×1/2 brace with clamped ends under monotonic end compression.
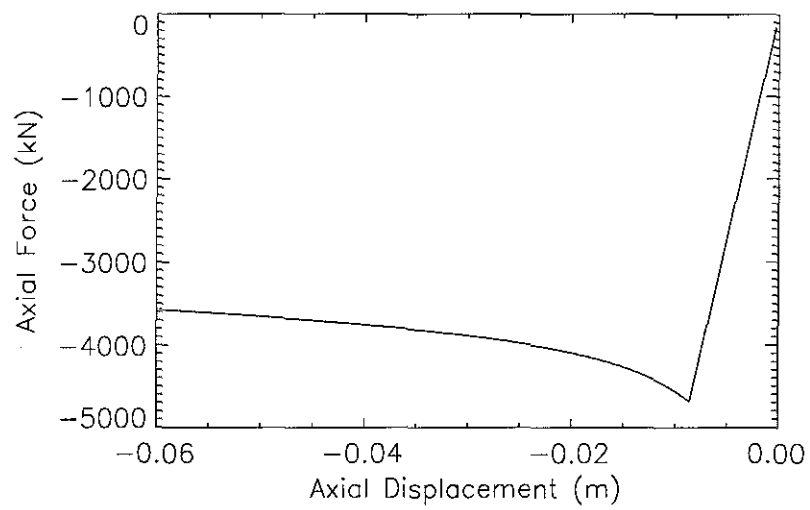


**Figure 2.12**: Loading curve for a □ 12×12×1/2 brace with clamped ends under monotonic end compression.

for braces with pinned ends and from

$$P_{cr} = \frac{\pi^2 EI}{(0.5L)^2} \qquad (2.4)$$

for braces with clamped ends. The uniform yield axial load is calculated from

$$P_y = A\sigma_y. \qquad (2.5)$$

Also shown in the table are the final axial loads and the maximum mid-span lateral deflection at the maximum end compression of 0.06 m.

As is expected, the peak axial force is upper-bounded by the lesser of the Euler critical buckling load and the uniform yield axial load. One interesting observation is that if the difference between the Euler critical buckling load and the uniform yield axial load of a brace is small, the percentage of the post-buckling drop in the axial load is large, as can be seen in the ratio between the final and peak axial forces for braces □ 6×6×1/2 and □ 8×8×1/2 with pinned ends in Table 2.2 and brace □ 4 × 4 × 1/2 with clamped ends in Table 2.3. For these braces the drop in axial force immediately after the peak is also the steepest, as can be seen from Figures 2.5, 2.6 and 2.9. The steep drop is observed in laboratory experiments [3, 22]. The post-buckling drop of the axial force is related to the deterioration of a brace under cyclic end displacement. Large drop often means more serious deterioration, therefore a small post-buckling drop in the axial force is preferable.

Tables 2.2 and 2.3 also list the final mid-span lateral deflections of the braces. The general trend is that braces with larger size have a smaller lateral deflection. This is probably because of a larger plastic shortening of the braces and a more even distribution of curvature over the length of the braces. Figure 2.13 shows a typical mid-span lateral deflection versus axial end displacement curve. A sudden increase in the lateral deflection is observed at the onset of buckling. Since the lateral deflection is several times larger than the corresponding axial displacement, the lateral acceleration is also expected to be large. It is of interest to know how the inertia force associated with the lateral acceleration affects the behavior of

| Brace | Axial Load Capacity (kN) | | | | | Mid-span Deflection (m) |
|---|---|---|---|---|---|---|
| | Euler | Yield | Peak | Final | Final/Peak | |
| □ 4×4×1/2 | 394 | 1433 | 367 | 124 | 34% | 0.385 |
| □ 6×6×1/2 | 1509 | 2251 | 1391 | 320 | 23% | 0.373 |
| □ 8×8×1/2 | 3812 | 3075 | 2836 | 660 | 23% | 0.349 |
| □ 12×12×1/2 | 13706 | 4704 | 4600 | 1800 | 39% | 0.290 |

**Table 2.2**: Summary results for braces with pinned ends under monotonic end compression. In the table, *Euler* refers to the Euler critical loads, *Yield* to the axial yielding loads, *Peak* to the computed peak axial loads, and *Final* to the computed axial loads at the maximum end compression.

| Brace | Axial Load Capacity (kN) | | | | | Mid-span Deflection (cm) |
|---|---|---|---|---|---|---|
| | Euler | Yield | Peak | Final | Final/Peak | |
| □ 4×4×1/2 | 1576 | 1433 | 1303 | 280 | 21% | 0.360 |
| □ 6×6×1/2 | 6036 | 2251 | 2205 | 805 | 37% | 0.300 |
| □ 8×8×1/2 | 15248 | 3075 | 3018 | 1600 | 53% | 0.240 |
| □ 12×12×1/2 | 54824 | 4704 | 4636 | 3564 | 77% | 0.167 |

**Table 2.3**: Summary results for braces with clamped ends under monotonic end compression. In the table, *Euler* refers to the Euler critical loads, *Yield* to the axial yielding loads, *Peak* to the computed peak axial loads, and *Final* to the computed axial loads at the maximum end compression.
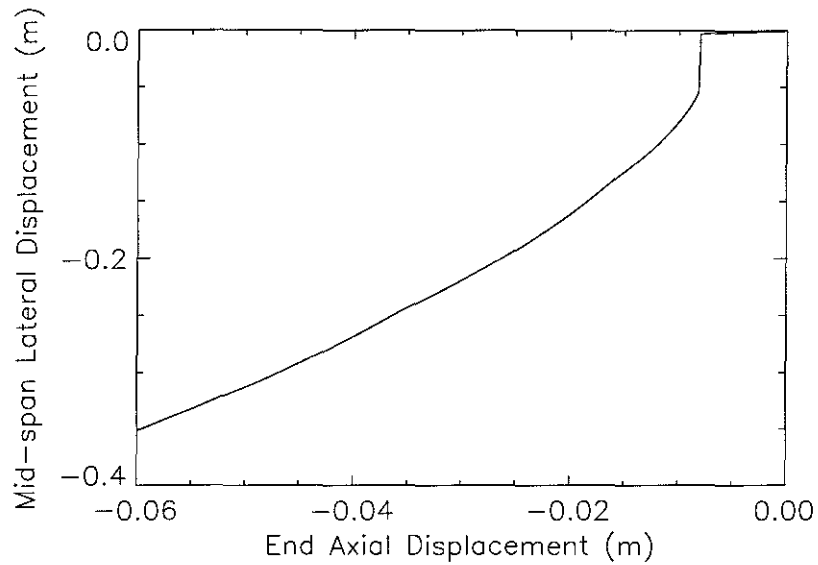
**Figure 2.13**: Mid-span lateral deflection versus axial end displacement curve for a □ 8 × 8 × 1/2 brace with pinned ends under monotonic end compression.

the brace during earthquake motions. This topic will be addressed later in this chapter.

Comparing Table 2.2 with Table 2.3 indicates that clamped ends increase the peak axial force capacity of slender braces by a large margin over braces of the same size with pinned ends. But for stocky braces, whose peak axial force capacity depends more on the yield axial force, this increase is smaller. In fact for the □ 12 × 12 × 1/2 brace, the increase is barely noticeable. However it is interesting to note that for all 4 braces under study, a clamped end condition increases the post buckling axial load capacity by roughly 100% over that of pin-ended braces, which conforms with experimental data [27]. This result can also be predicted with the simple plastic hinge model shown in Figure 2.14, which ignores the axial deformation and the interaction between the moment capacity of the hinge and the axial force of a brace. Consider a small increment $\Delta\theta$ in the angle $\theta$. The corresponding decrease in $l$ is

$$\Delta l = L \sin\theta \, \Delta\theta \tag{2.6}$$

where $L$ is the length of the undeformed brace. For a brace with clamped ends, the energy

balance equation is

$$P\Delta l = (M + 2M + M)\Delta\theta \tag{2.7}$$

where $P$ is the axial force and $M$ the plastic moment capacity of the brace. Solving the above equations yields

$$P = \frac{4M}{L\sin\theta}. \tag{2.8}$$

For a brace with pinned ends, the same process produces

$$P = \frac{2M}{L\sin\theta}, \tag{2.9}$$

which shows that the axial force for a brace with pinned ends is half of that for one of the same size with clamped ends. It can also be easily seen from above that the energy dissipation by a brace with clamped ends is twice of that by a brace with pinned ends under the same end displacement.



(a) Pinned Ends          (b) Clamped Ends
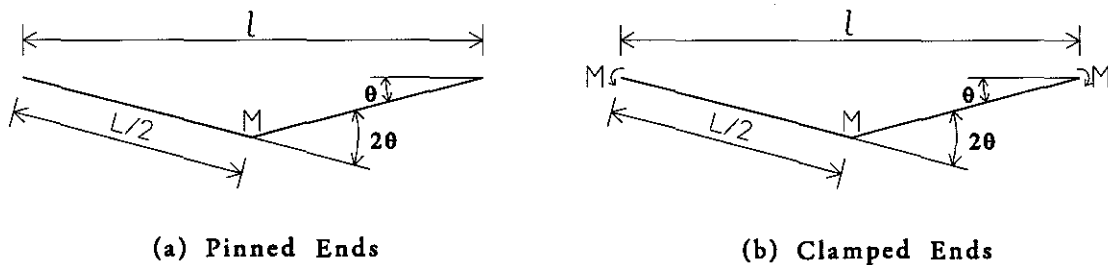
Figure 2.14: A simple plastic hinge model for estimating the post-buckling axial force and energy dissipation of braces.

A clamped end condition also reduces the lateral deflection, especially for stocky braces, which can not be predicted by the above simple model. Clearly the above equations only applies to relatively large $\theta$ since $P$ approaches infinite as $\theta$ approaches 0.

Experiment results [3,7,28] and earthquake damage surveys [1,2,12] show that braces frequently fail as a result of local buckling that leads to severe local deformation and eventually cracking. Since large compressive deformation is the primary cause of local buckling and rupture, it is therefore of interest to study the deformation of the braces under axial end displacement. Figures 2.15~2.20 plot the distribution of fiber strains in the top and bottom

of braces with different sizes and end conditions at different stages of the compression. An envelope curve is also plotted so that the maximum strain is reflected in the figures.
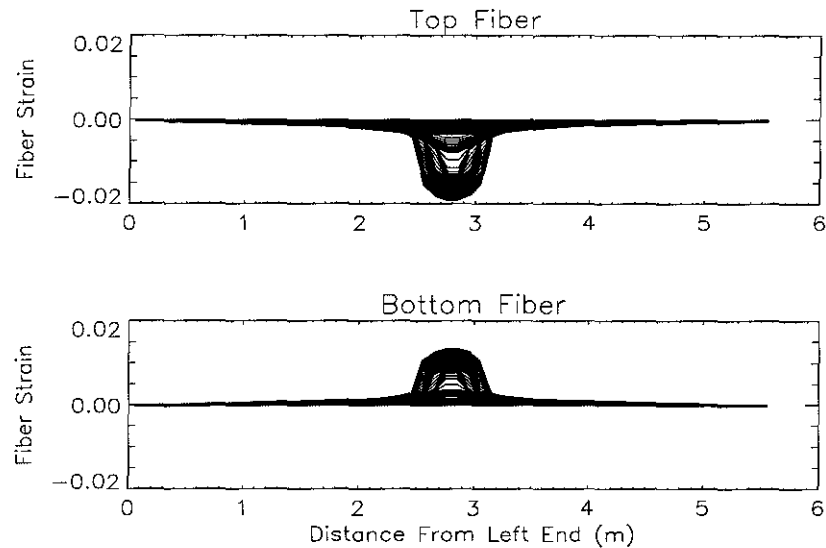


**Figure 2.15**: Distribution of top and bottom fiber strains over the length of a □ 4 × 4 × 1/2 brace with pinned ends at different stages of the monotonic end compression.

It is seen from the figures that for braces with pinned ends, the deformation is mostly concentrated on a short segment near the mid-span. For braces with clamped ends, the deformation is concentrated in short segments near the two ends as well as the mid-span. It is noted that braces with clamped ends, because of symmetry, the deformation in each half-length is anti-symmetrical about the quarter point. The concentration of deformation is especially acute for braces of small cross-section, although this does not necessarily lead to larger strain in a brace of smaller size than in one of larger size, mainly because the outermost fibers in a smaller brace are closer to the centroid of the cross-section. The typical magnitude of maximum strain for the braces is several times the average axial strain (1.1%), which could be enough to cause local buckling.

Table 2.4 summarizes the mid-span strains in the top and bottom fibers of the braces. The compressive strains, which causes local buckling, are higher in braces with clamped ends than in braces with pinned ends for 3 of the 4 sizes. For braces with pinned ends, the maximum compressive strain seems to increase with the size, while for braces with clamped
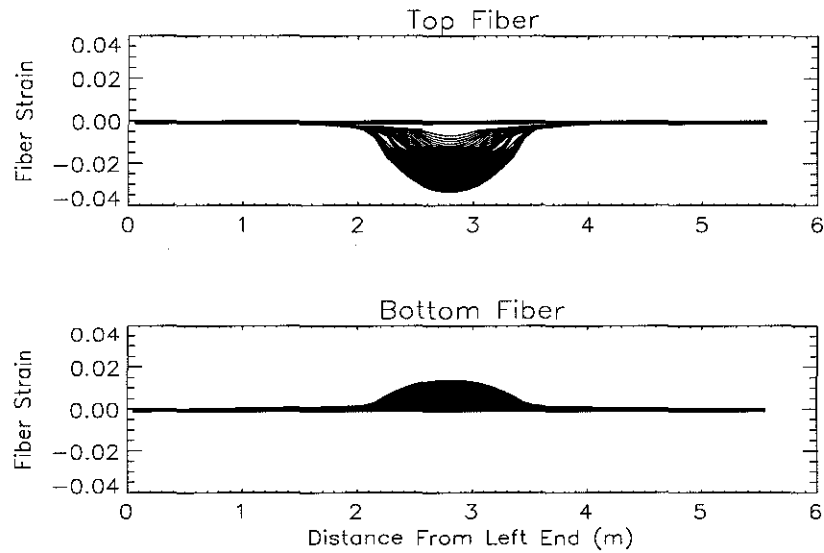
**Figure 2.16**: Distribution of top and bottom fiber strains over the length of a □ 8×8×1/2 brace with pinned ends at different stages of the monotonic end compression.
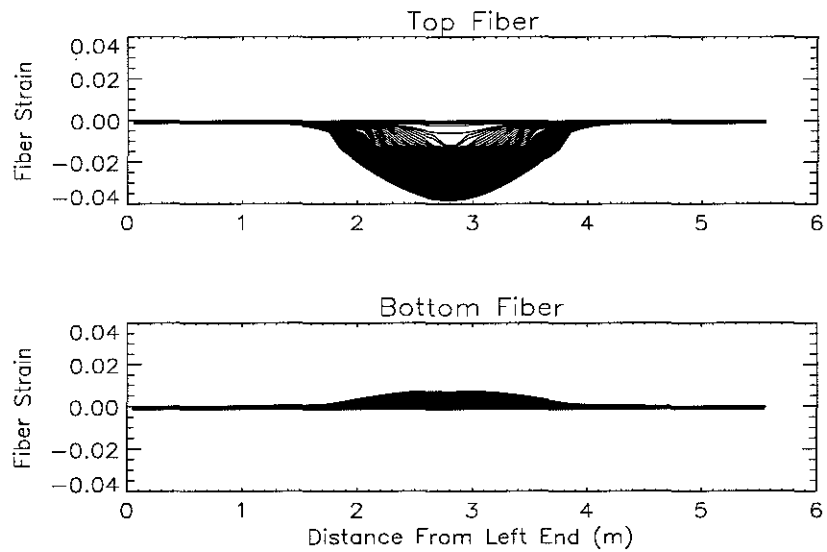


**Figure 2.17**: Distribution of top and bottom fiber strains over the length of a □ 12×12×1/2 brace with pinned ends at different stages of the monotonic end compression.
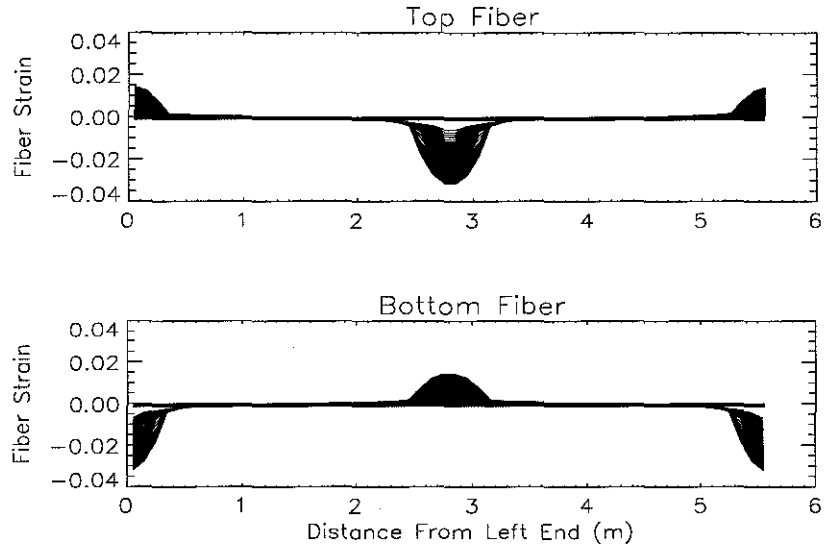
**Figure 2.18**: Distribution of top and bottom fiber strains over the length of a □ 4×4×1/2 brace with clamped ends at different stages of the monotonic end compression.
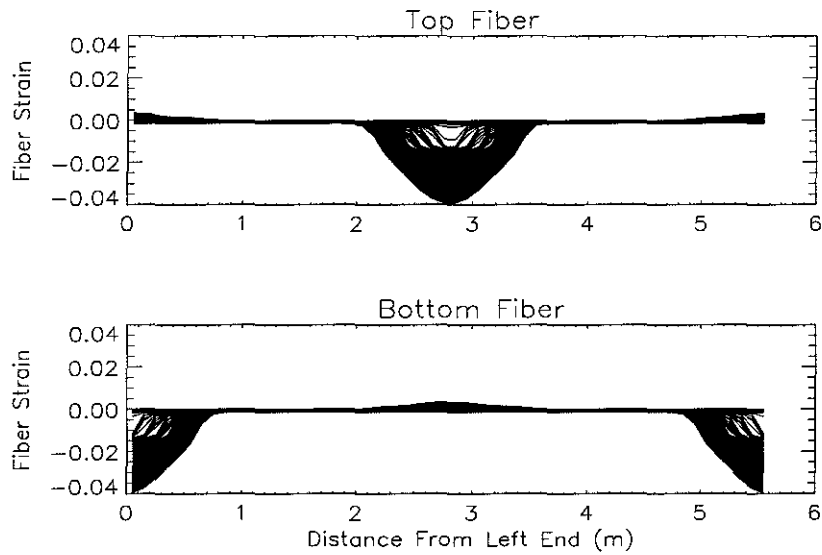


**Figure 2.19**: Distribution of top and bottom fiber strains over the length of a □ 8×8×1/2 brace with clamped ends at different stages of the monotonic end compression.
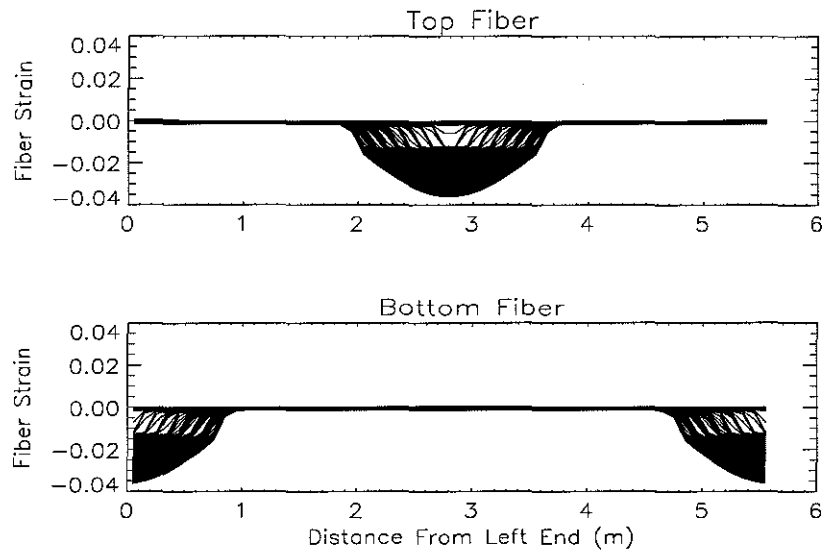
**Figure 2.20**: Distribution of top and bottom fiber strains over the length of a □ 12×12×1/2 brace with clamped ends at different stages of the monotonic end compression.

| Brace | Pin-Ended | | Clamp-Ended | |
|---|---|---|---|---|
| | Top | Bottom | Top | Bottom |
| □ 4 × 4 × 1/2 | -1.9% | 1.4% | -3.1% | 1.4% |
| □ 6 × 6 × 1/2 | -2.6% | 1.5% | -3.8% | 0.9% |
| □ 8 × 8 × 1/2 | -3.4% | 1.6% | -4.0% | 0.3% |
| □ 12 × 12 × 1/2 | -3.8% | 0.8% | -3.7% | 0.1% |

**Table 2.4**: Maximum mid-span fiber strains in braces with pinned or clamped ends under monotonic end compression.

ends the trend is less clear. It is also noted that, even though the braces are under compression, significant tensile strain can develop in the bottom fibers.

## Braces With Eccentricity

The end conditions in the above cases were applied without eccentricity. However in engineering practice eccentricity is inevitable. It is therefore of interest to examine the effect of eccentricity on the behavior of braces with pinned ends. Braces with eccentricity ranging from 5% to 15% of the side width are subjected to the same end compression used above, and their axial force versus axial end displacement curves are compared with those of braces with concentric loading.
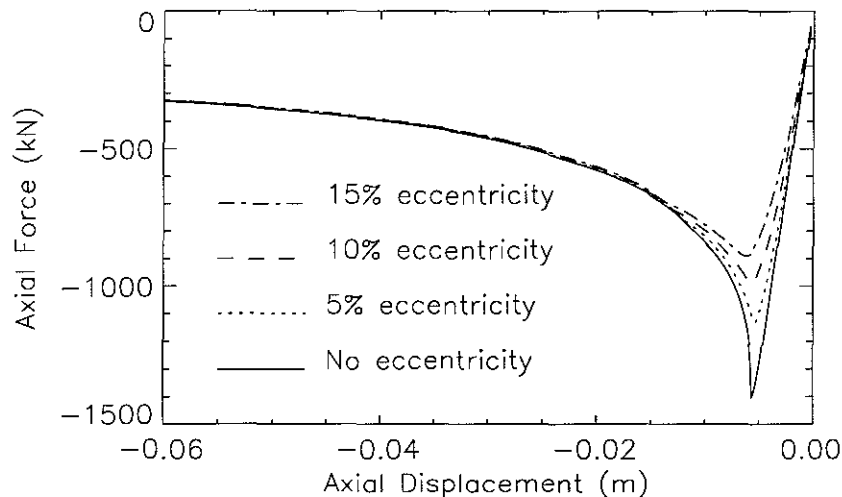
**Figure 2.21**: Loading curves for a □ 6 × 6 × 1/2 brace with pinned ends and different eccentricities under monotonic end compression.

Figure 2.21 shows the axial force versus end displacement curves for a □ 6×6×1/2 brace with different levels of eccentricity: no eccentricity, with 5%, 10% and 15% eccentricity. It is seen that the peak compressive load of the brace is very sensitive to the eccentricity. But the effect of eccentricity on the axial force is significant only around the peak, and beyond this point the effect is almost unnoticeable. Braces of other sizes show similar results. Based on this result, from here on all braces will be considered to be loaded concentrically.

## 2.3.2 Braces Under Cyclic End Displacement

The quasi-static behavior of braces under cyclic axial end displacement is the focus of this sub-section. The four braces in Table 2.1 on page 6 are subjected to the displacement sequence shown in Figure 2.1 on page 7. Both pinned-pinned and clamped-clamped end conditions are considered.

### Braces With Pinned Ends

Figures 2.22~2.25 show the hysteresis loops of the braces with pinned ends under cyclic end displacement. Serious deterioration after initial buckling is observed in all four braces. In the post-buckling cycles, the maximum axial force that can be supported by a brace under compression is often only a small fraction of its initial buckling load and becomes even smaller with each cycle as a consequence of the accumulating residual lateral deflection and the Bauschinger effect which reduces the tangent modulus of the fibers.
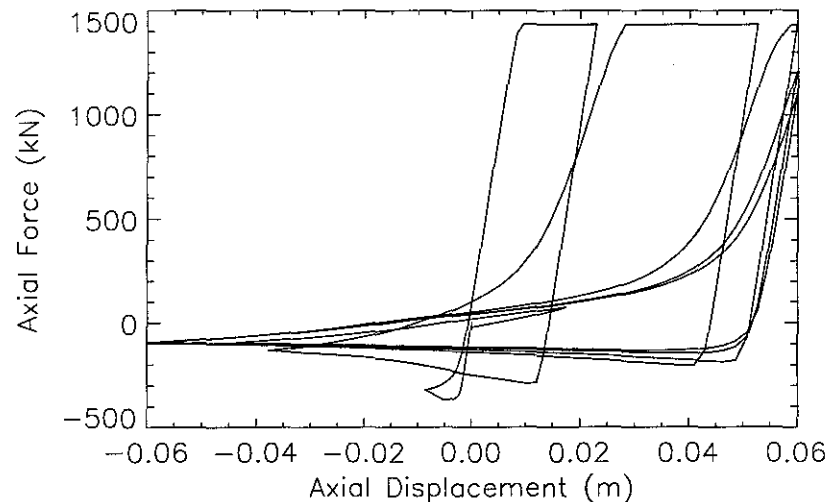


**Figure 2.22**: Static response: Hysteresis loops of a □ 4 × 4 × 1/2 brace with pinned ends under cyclic end displacement.

The upper portions of the hysteresis loops, which correspond to the elongation phase of the cycles, are severely pinched because of the residual inelastic elongation and lateral de-

26
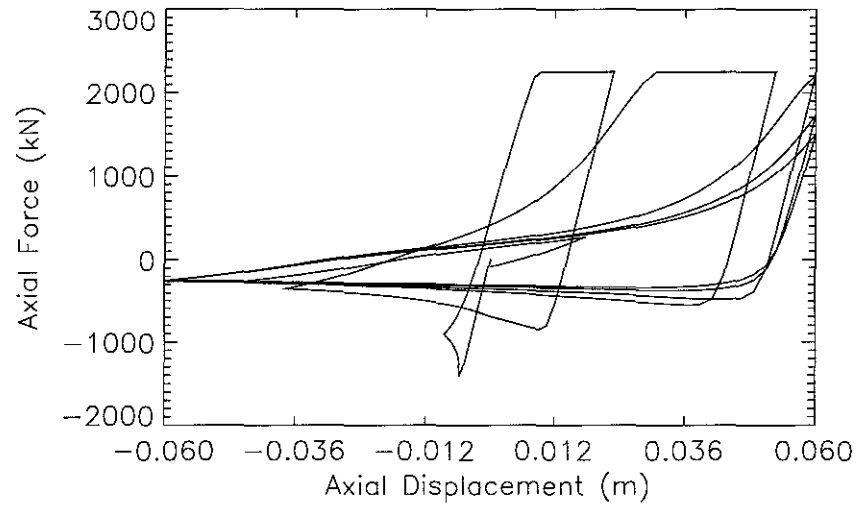


**Figure 2.23**: Static response: Hysteresis loops of a □ 6 × 6 × 1/2 brace with pinned ends under cyclic end displacement.
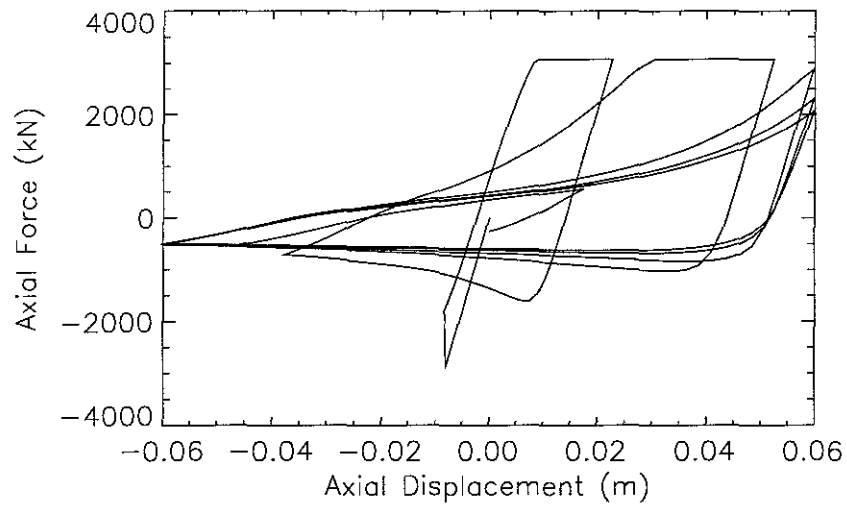


**Figure 2.24**: Static response: Hysteresis loops of a □ 8 × 8 × 1/2 brace with pinned ends under cyclic end displacement.

27
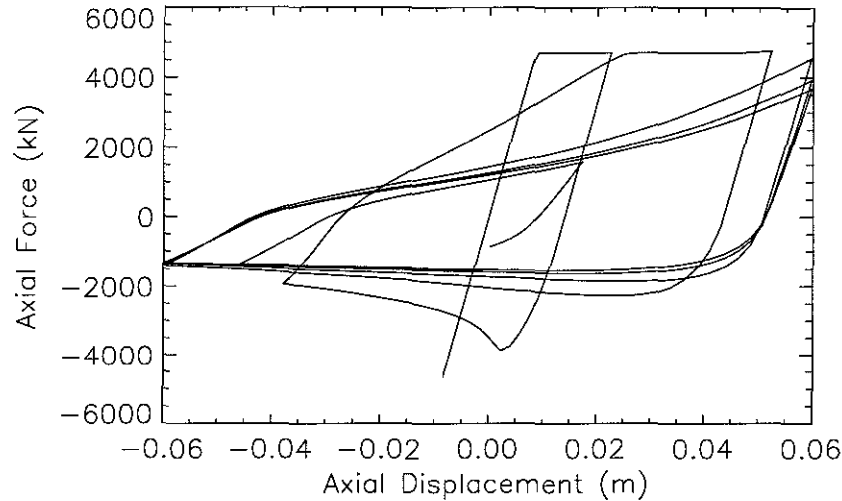
**Figure 2.25**: Static response: Hysteresis loops of a □ 12 × 12 × 1/2 brace with pinned ends under cyclic end displacement.

flection of the braces. As a result, the area enclosed by the hysteresis loop in a cycle, which is equivalent to the energy dissipated through inelastic deformation in the cycle, experiences a large reduction. The severity of the deterioration is strongly related to the slenderness of a brace, with deterioration of slender braces more severe than stocky ones, as can be seen by comparing the hysteresis loops shown in the figures.

The accumulation of inelastic axial elongation also affects the magnitude of the lateral deflection of the braces. As a result, the braces experience a larger lateral deflection under cyclic end displacement than under monotonic one of the same magnitude, as can be seen by comparing the maximum lateral deflections listed in Table 2.5 on page 31 and Table 2.2 on page 17. The effect of elongation on the lateral deflection can be seen clearly in Figure 2.26, which shows a typical mid-span lateral deflection versus end axial displacement relation. After each elongation (the straight line segments near the top) the reversal curve traces a path of larger lateral deflection (absolute value). The reason for this is that the brace becomes longer as a result of inelastic elongation, and it has to bend more to accommodate the additional length when it is compressed. This results in a larger mid-span lateral deflection than when the brace is subjected to monotonic end displacement of the same magnitude.

The same can also be seen in the time history of the mid-span lateral deflection shown in Figure 2.27. One can see that the lateral deflection does not vanish even when the brace is subjected to its maximum tensile force, and when the end displacement finally returns to zero there remains a 35 cm residual mid-span lateral deflection.
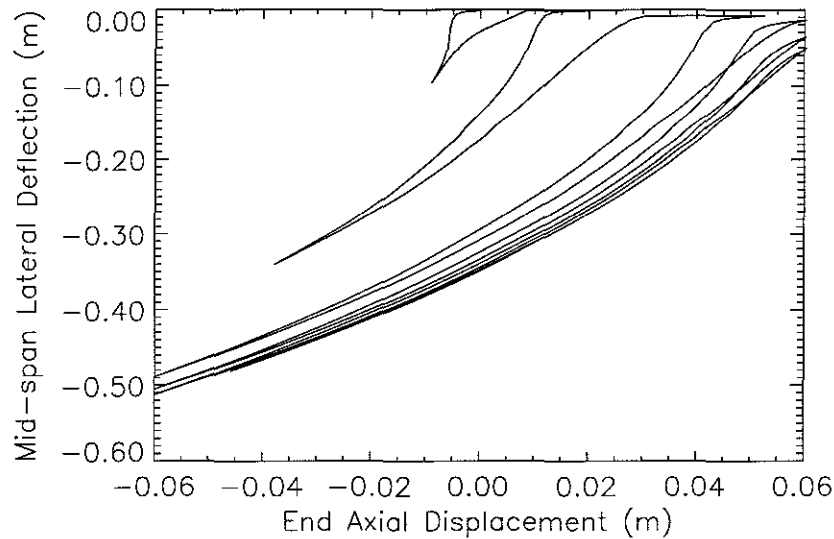


**Figure 2.26**: Static response: Mid-span lateral deflection versus axial end displacement curves for a □ 6×6× 1/2 brace with pinned ends under cyclic end displacement.

Shown in Figures 2.28 to 2.31 are the distributions of fiber strains over the length of these braces. Similar to braces under monotonic end compression, the strains are mostly concentrated near the mid-span of the braces, although the shape of the distribution is more complicated. Maximum compressive strains always occur at the top, and the maximum tensile strains at the bottom of the braces. Because of the residual plastic bending deformation, the stain distribution is not uniform even under tensile force.

The maximum tensile and compressive strains for the braces under cyclic end displacement are summarized in Table 2.5 on page 31. Compared with Table 2.4 on page 23, the effect of brace size on the maximum compressive strain is more pronounced: there are larger compressive strains in braces of larger size. For example, under cyclic end displacements, the maximum strain in the □ 12×12×1/2 brace is 3.6 times that of the □ 4×4×1/2 brace, while
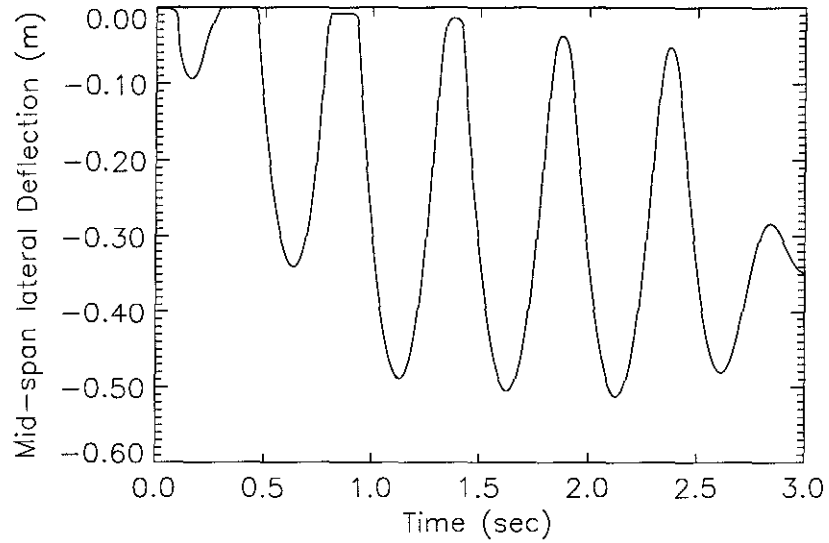
**Figure 2.27**: Static response: Mid-span lateral deflection of a □ 6×6×1/2 brace with pinned ends under cyclic end displacement.
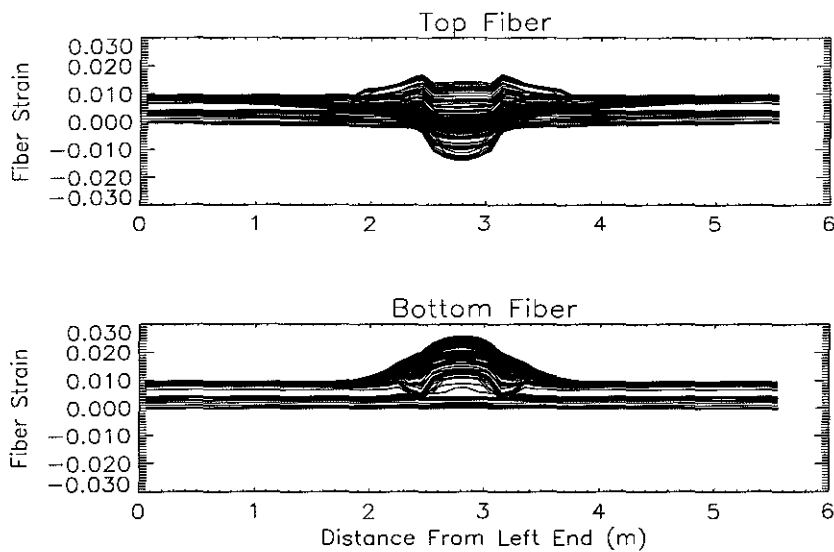


**Figure 2.28**: Static response: Distribution of top and bottom fiber strains over the length of a □ 4 × 4 × 1/2 brace with pinned ends under cyclic end displacement.

30
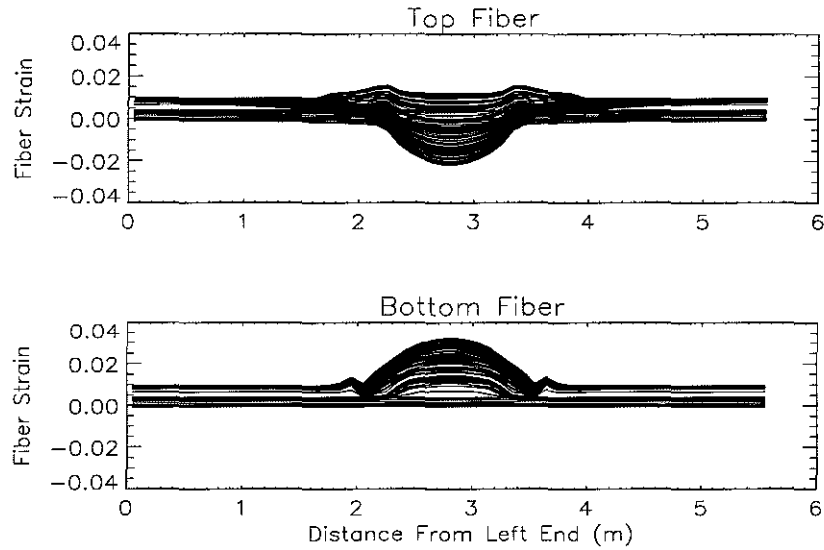


**Figure 2.29**: Static response: Distribution of top and bottom fiber strains over the length of a □ 6 × 6 × 1/2 brace with pinned ends under cyclic end displacement.
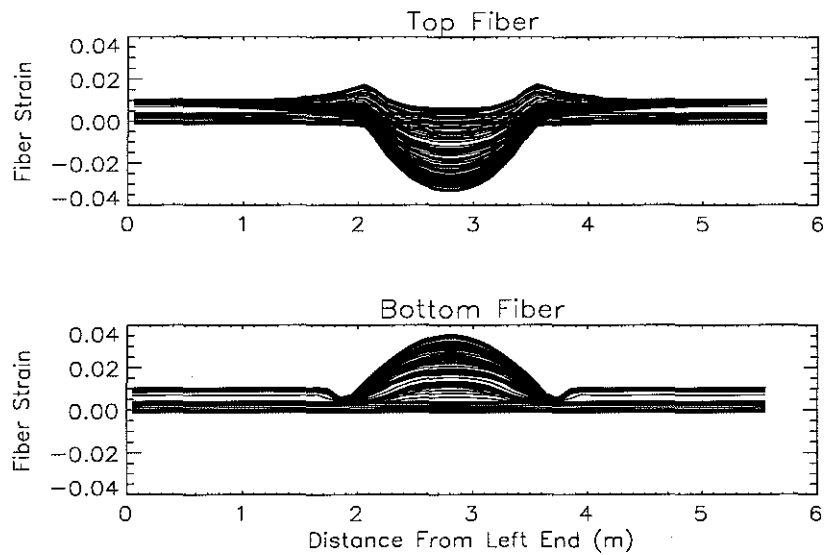


**Figure 2.30**: Static response: Distribution of top and bottom fiber strains over the length of a □ 8 × 8 × 1/2 brace with pinned ends under cyclic end displacement shown in Figure 2.1 on page 7.
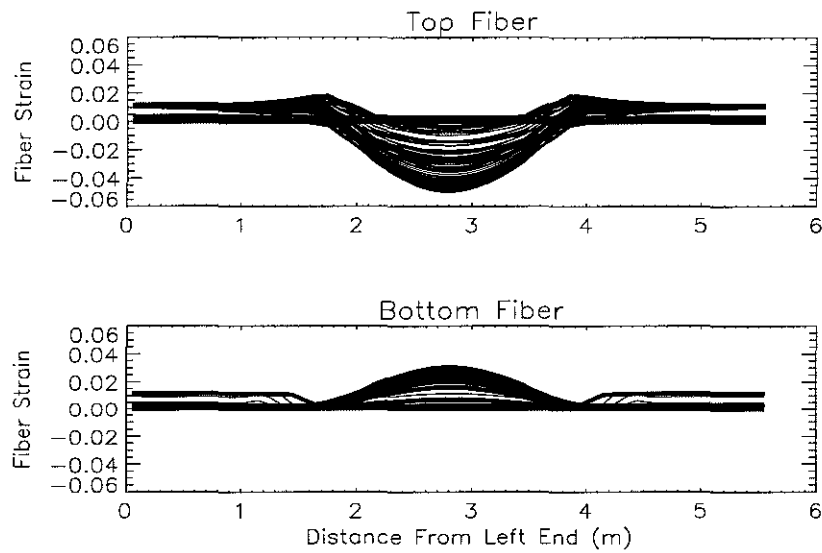
**Figure 2.31**: Static response: Distribution of top and bottom fiber strains over the length of a □ 12×12×1/2 brace under cyclic end displacement.

the ratio under monotonic compression is 2. Excessive compressive strain poses the danger of causing local buckling and rupture of a brace. But it should be noted that the comparison is based on the assumption that all braces are subjected to the same end displacement. The end displacement which a brace in a structure is subjected to also depends on the strength of the brace itself.

The maximum tensile strain for braces under cyclic displacement is about 3 times of the

| Brace | Tensile Strain | Compressive Strain | Lateral Deflection (m) |
|---|---|---|---|
| □ 4×4×1/2 | 2.6% | -1.4% | 0.52 |
| □ 6×6×1/2 | 3.2% | -2.2% | 0.51 |
| □ 8×8×1/2 | 3.6% | -3.3% | 0.50 |
| □ 12×12×1/2 | 3.3% | -5.0% | 0.46 |

**Table 2.5**: Summary of maximum responses for braces with pinned ends under cyclic end displacement. Maximum compressive strains always occur in top fiber, and maximum tensile strains in bottom fiber.
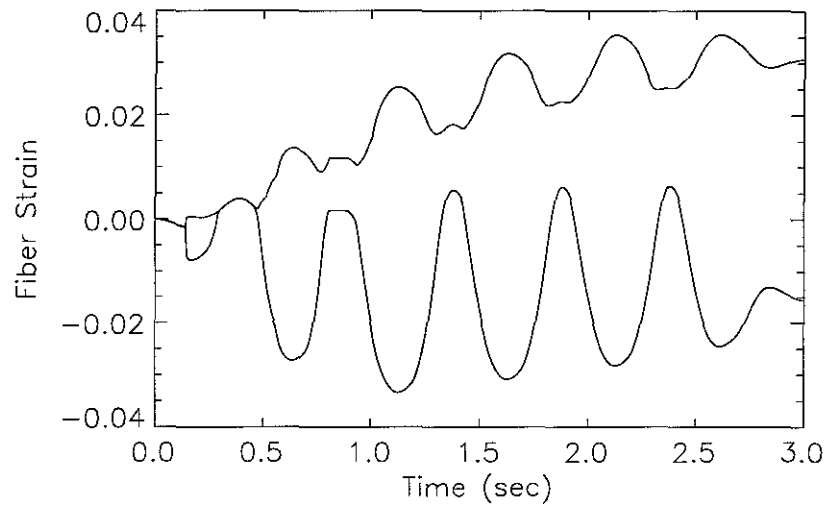
**Figure 2.32**: Static response: Fiber strain histories for a □ 8×8×1/2 brace with pinned ends under cyclic end displacement. The upper curve is for strain in the bottom fiber, and the lower one is for that in the top fiber.
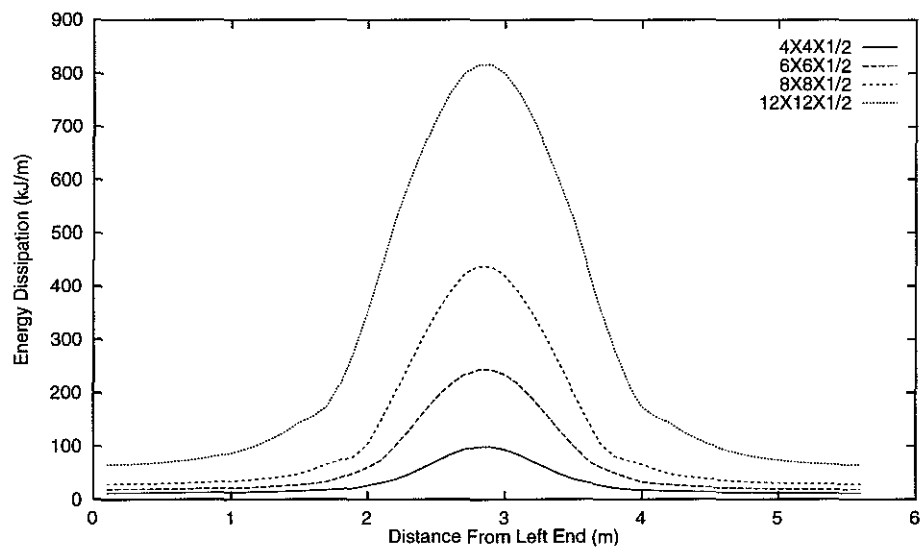


**Figure 2.33**: Static response: Distribution of energy dissipation over the length of □ 4×4×1/2, □ 6×6×1/2, □ 8×8×1/2 and □ 12×12×1/2 braces with pinned ends under cyclic end displacement.

uniform tensile strain, which is, understandably, also larger than its counterpart for braces under monotonic end compression (Table 2.4 on page 23). One interesting characteristic to note is that the maximum tensile strain tends to accumulate when the fibers experience repeated plastic deformation. As shown in Figure 2.32, the tensile strain in the bottom fibers continues to grow after about $T = 1.0$ second even though the end displacement amplitude remains constant, as can be seen by comparing with Figure 2.1 on page 7. The strain remains positive even when the end displacement is negative.

The distribution of energy dissipation over the length of the braces is shown in Figure 2.33. It is seen that the energy dissipation occurs mainly in a small region near the mid-span of the braces.

**Braces With Clamped Ends**

It has been shown in Section 2.3.1 on page 10 that under monotonic end compression, clamped ends can roughly double the post-buckling load capacity of a brace. In this subsection, the effect of clamped end condition on the hysteretic behavior of braces under cyclic end displacement is studied. Except for the end condition, everything else is identical to the case of pinned end condition.

Figures 2.34~2.36 show the hysteresis loops of braces with clamped ends. Compared with braces with pinned ends, braces with clamped ends develop fuller hysteresis loops, which means that they experience less deterioration and will be able to dissipate more energy in each cycle. Similar to braces with pinned ends, the hysteresis loops of large size braces appear more stable than those of smaller size ones.

Shown in Figures 2.37~2.39 are the typical distribution of strains in the top and bottom fibers over the length of braces with clamped ends. Similar to the case of braces under monotonic end compression, the deformation is mostly concentrated in short segments near the mid-span and the two ends, and there is a mirror symmetry between the top fiber strain and the bottom fiber strain about the quarter-span of the braces. However the maximum compressive strains are much larger for braces under cyclic end displacement, as can be
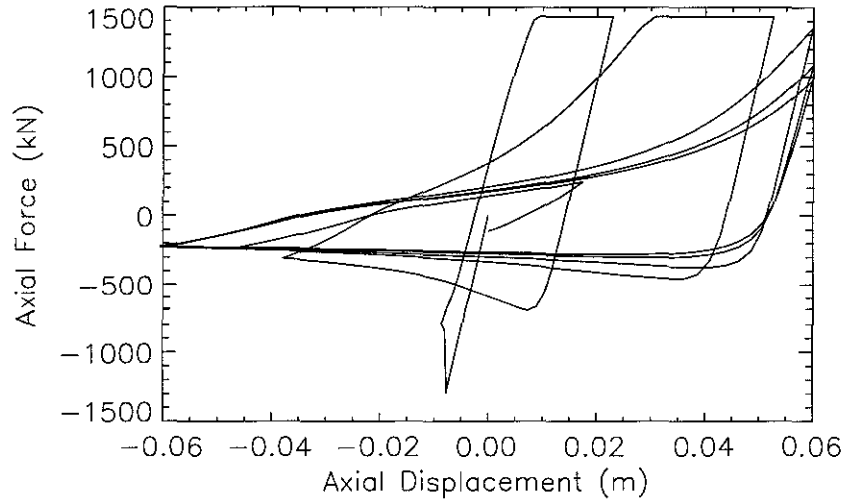
**Figure 2.34**: Static response: Hysteresis loops of a □ 4 × 4 × 1/2 brace with clamped ends under cyclic end displacement.
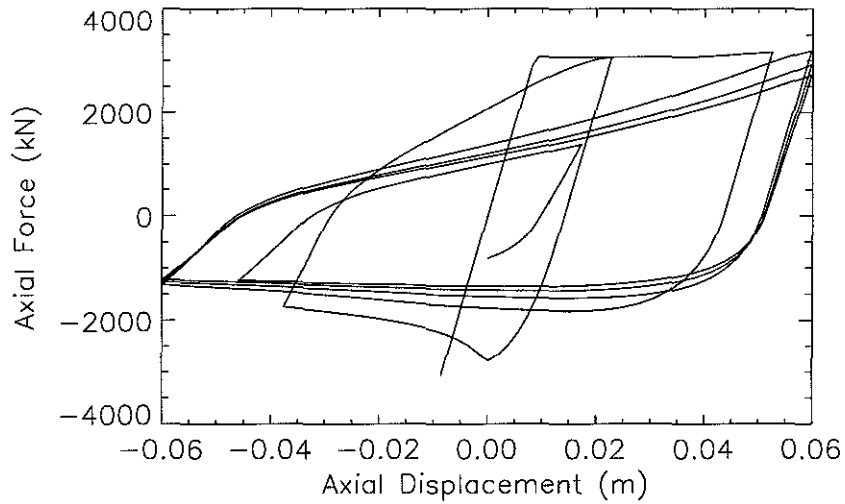


**Figure 2.35**: Static response: Hysteresis loops of a □ 8 × 8 × 1/2 brace with clamped ends under cyclic end displacement.

35
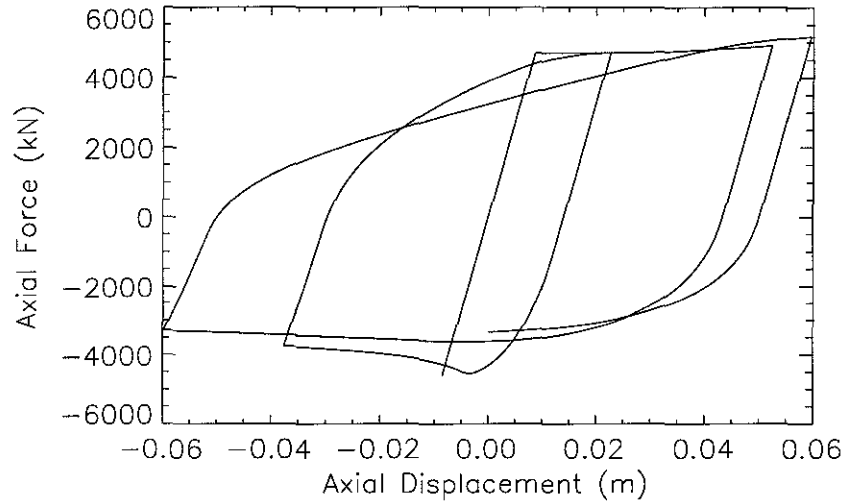


**Figure 2.36**: Static response: Hysteresis loops of a □ 12×12×1/2 brace with clamped ends under cyclic end displacement.
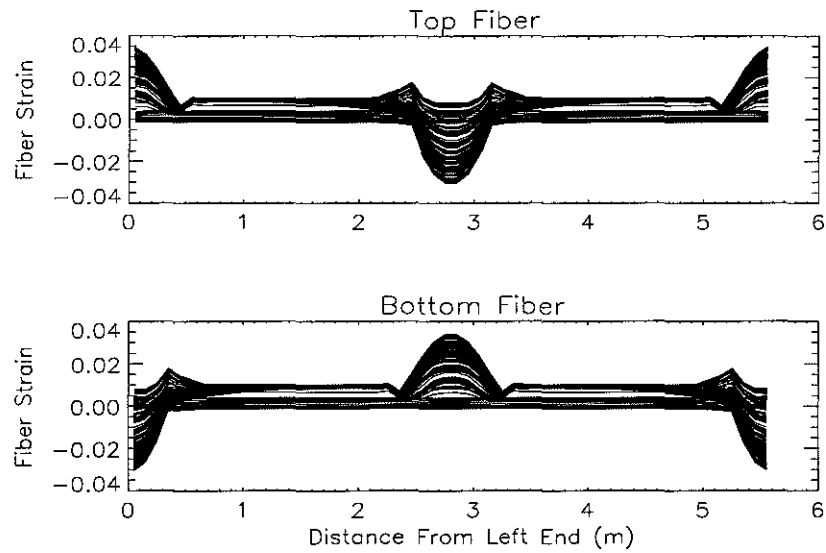


**Figure 2.37**: Static response: Distribution of fiber strains in the top and bottom fibers over the length of a □ 4×4×1/2 brace with clamped ends under cyclic end displacement.
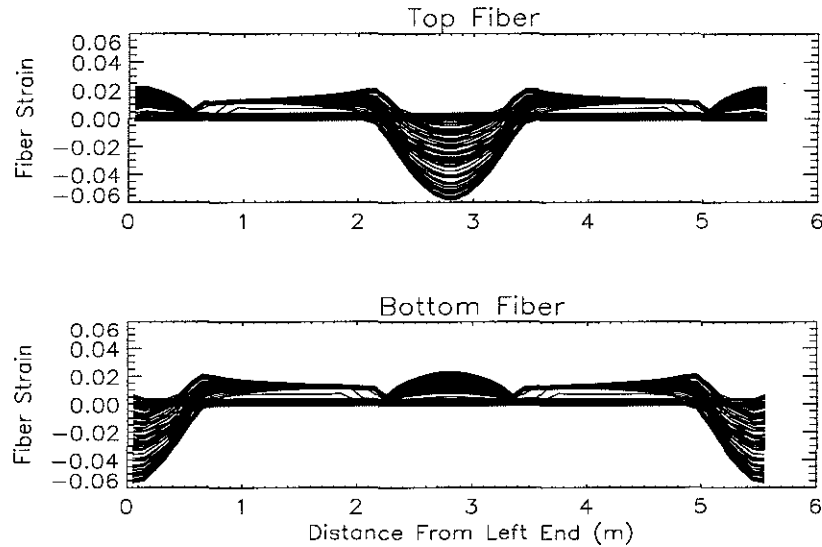
**Figure 2.38**: Static response: Distribution of fiber strains in the top and bottom over the length of a □ 8×8×1/2 brace with clamped ends under cyclic end displacement.
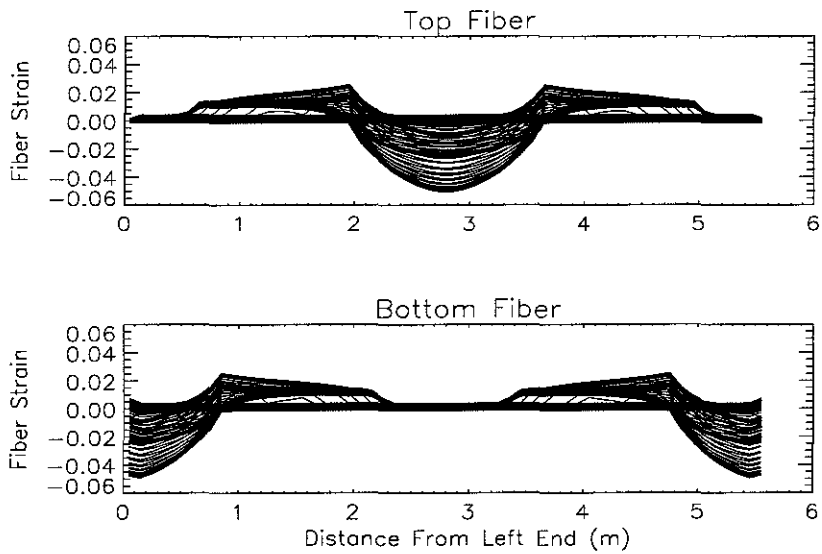


**Figure 2.39**: Static response: Distribution of fiber strains in the top and bottom over the length of a □ 12 × 12 × 1/2 brace with clamped ends under cyclic end displacement.

| Brace | Tensile Strain | Compressive Strain | Lateral Deflection (m) |
|---|---|---|---|
| □ 4 × 4 × 1/2 | 3.5% | -3.1% | 0.50 |
| □ 6 × 6 × 1/2 | 3.4% | -4.7% | 0.47 |
| □ 8 × 8 × 1/2 | 2.3% | -5.8% | 0.41 |
| □ 12 × 12 × 1/2 | 2.5% | -5.0% | 0.25 |

**Table 2.6**: Summary of maximum responses for braces with clamped ends under cyclic end compression.

seen by comparing Table 2.6 with Table 2.4 on page 23. The maximum compressive strains for the braces with clamped ends are also higher than those of the braces of the same size with pinned ends shown in Table 2.5 on page 31.
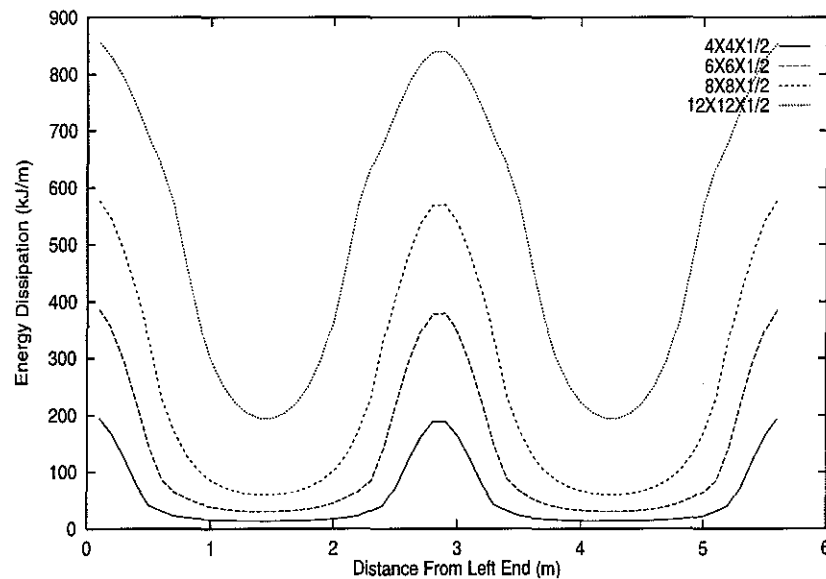


**Figure 2.40**: Static response: Distribution of energy dissipation over the length of the □ 4×4×1/2, □ 6×6×1/2, □ 8 × 8 × 1/2 and □ 12 × 12 × 1/2 braces with clamped ends under cyclic end displacement.

Figure 2.40 shows the distribution of energy dissipation through inelastic deformation over the length of the four braces with clamped ends under cyclic end displacement. Comparing with Figure 2.33 on page 32 shows that the maximum energy dissipations per unit length for braces with pinned and clamped ends are about the same. The total inelastic

| Brace | Energy Dissipation (kJ) | |
|---|---|---|
| | Pinned Ends | Clamped Ends |
| □4×4×1/2 | 165 | 301 |
| □6×6×1/2 | 376 | 720 |
| □8×8×1/2 | 678 | 1328 |
| □12×12×1/2 | 1556 | 2835 |

**Table 2.7**: Summary of energy dissipation through plastic deformation for braces with different end conditions under cyclic end displacement.

energy dissipation for each of the four braces with different end conditions is listed in Table 2.7. It is seen that the energy dissipated by a clamp-ended brace is about twice that dissipated by a pin-ended brace of the same size. This ratio agrees with the approximate result given by the plastic hinge model on page 19. Large braces dissipate more energy per unit cross-sectional area, as can be seen by comparing the energy dissipation in Table 2.7 with the cross-sectional areas in Table 2.1 on page 6.

## 2.3.3 Summary

The quasi static responses of four individual braces under monotonic and cyclic end displacements have been studied in this section, with emphasis on the magnitude and distribution of axial strains in the braces. The main results are summarized as follows.

The distribution of strains in the braces is highly uneven and strain concentration occurs. For braces with pinned ends, the strains are concentrated near the mid-span; for braces with clamped ends, the strains are concentrated both near the mid-span and the two ends. The maximum strain is usually several times the uniform strain. The size of a brace has significant effect on the strain distribution and magnitude. This is especially true for the compressive strain which causes local buckling. The axial strains in braces of smaller size tend to concentrate in a smaller length of the brace, however the magnitudes of (especially the

compressive) strains in braces of large size tend to be larger.

The end conditions have a strong effect on the initial buckling load of a slender brace, while the effect of the yield stress dominates the initial buckling load for stocky ones. However for braces of all sizes, clamped ends significantly increase the post-buckling compressive load and energy dissipation capacities. There is usually a steep drop in the axial load immediately after the initial buckling of a slender brace, and the post buckling axial load is usually only a small fraction of the initial buckling load with the exception of braces with very small slenderness ratio. The drop in axial load for very stocky braces is small and the hysteresis loops are quite stable. It is also noted that the drop in axial load after the initial buckling is affected by the closeness of the Euler critical buckling load and the yield axial load. The drop seems steeper for braces whose Euler critical buckling load and yield axial load are close.

The maximum strains and lateral deflections of braces tend to be larger when subjected to cyclic end displacement than when subjected to monotonic end displacement of the same magnitude. Some response quantities, notably the lateral deflection and the tensile strain in the bottom fiber, tend to grow with each cycle even when the amplitude of the cycling end displacement remains constant. The magnitude of the lateral deflection is much larger than the axial end displacement, which suggests that the effect of the lateral inertia force under certain conditions may be important.

## 2.4   Dynamic Behavior

As was seen in the previous section, a brace can develop quite a large lateral deflection when it buckles. Judging from this there is reason to believe that the lateral acceleration can also be large, and the inertia force associated with the acceleration could have significant effect on the behavior of the brace. This is beyond what the above quasi-static analysis can account for and is the subject of this section. The goal of this section is to determine how, under what condition and to what extent, the inertia force affects the response of a brace under cyclic

end displacement.

The dynamic responses of three braces with sizes of □ 4×4×1/2, □ 6×6×1/2 and □ 8×8×1/2 are obtained by including the mass of the braces in the analysis. One important and complicated issue in dynamic analysis of structures is damping. According to the form in which it appears in the differential equations of motion, damping in building structures can usually be divided into two categories: viscous damping and hysteretic damping. Viscous damping is used to model energy dissipation that is dependent on the velocity of a structure, and hysteresis damping to model energy dissipation associated with permanent deformation of a structure. But in many practical problems the two are difficult to distinguished and are often lumped together.

The viscous damping in discrete systems is frequently represented by the Caughey Series [29], especially in its simplified form:

$$[C] = \alpha[M] + \beta[K] \tag{2.10}$$

where $[M]$ is the mass matrix and $[K]$ the stiffness matrix of the system. The viscous damping associated with the mass term is related to the absolute motions of the mass, while that associated with the stiffness term is related to the relative motion among the nodes in the system.

The damping coefficients $\alpha$ and $\beta$ in the above equation for a specific structure are usually computed from modal damping ratios based on available experimental data for similar structures. The experiments are usually conducted under elastic conditions. Because of this and its linearity, viscous damping in the above form is more appropriate to be used to model damping in structures under linear small amplitude vibrations. The portion of the damping associated with inelastic deformation is accounted for by a hysteresis model.

Great amount of efforts have been directed towards the acquisition and accumulation of viscous damping data for various structures. Nevertheless, little information in this regard is available for structural elements like individual braces. Yet preliminary study indicates that the linear viscous damping represented by Equation 2.10 has significant effect on the

response of a brace under imposed cyclic end displacement. A 2% equivalent damping ratio, calculated at $T = 0.5$ sec and $T = 1.5$ sec, can increase the plastic energy dissipation of a brace by several fold over that of an undamped one. The increase of post-buckling axial load capacity caused by the damping is also significant.

The damping ratio used for steel structures is normally in the range of 2%~5%, depending on factors like the types of wall fillings and beam-to-column joints used in the structures. It is believed that much of the damping of a complete steel structure in elastic vibration can be attributed to the non-structural components. Moreover, the suitability of linear viscous damping in cases where the structure develops large plastic deformation is questionable because under such situation the viscous damping terms can cause excessive energy dissipation and internal forces [30]. Based on this argument, a damping ratio of 0.2% for the individual braces is assumed in this study.

Braces of three different sizes listed in Table 2.1 on page 6 are used in this part of the study: □ 4×4×1/2, □ 6×6×1/2 and □ 8×8×1/2, and only the pinned-pinned end condition is considered. The braces are subjected to three end displacement histories of different frequencies as listed in Table 2.8. One of them is plotted in Figure 2.1 on page 7, and the other two are derived from it through temporal scaling. The unscaled displacement history (H-05) has a period of 0.5 seconds. The two scaled displacement histories have a period of 0.2 seconds (H-02) and 0.8 seconds (H-08), respectively. All of them have an identical peak amplitude of 0.06 meters. Since the differences between the responses of the braces under H-05 and H-08 are small, only the results under the latter, along with the results for H-02, will be discussed in detail.

## 2.4.1 Under Displacement H-08

Figures 2.41 and 2.42 show the typical dynamic time history of axial force and the hysteresis loops, respectively, of the □ 6×6×1/2 brace under displacement H-08. From both figures one can see the high frequency vibrations that follow each buckling of the brace. Comparing Figure 2.42 with the static hysteresis loops of the same brace shown in Figure 2.23 re-

| End Displacement History | Peak Amplitude (m) | Period (sec) |
|:---:|:---:|:---:|
| H-02 | 0.06 | 0.2 |
| H-05 | 0.06 | 0.5 |
| H-08 | 0.06 | 0.8 |

Table 2.8: End displacement histories used in the study of the dynamic behavior of braces. History H-05 is the same as that shown in Figure 2.1 on page 7 and the other two are derived from it through temporal scaling.

veals two distinct differences: For the dynamic case, the peak compressive loads are higher (1750 kN versus 1350 kN), and the hysteresis loops are no longer smooth because of the high frequency vibrations that follow each buckling of the brace. But the areas covered by the loops do not seem to differ much. The higher dynamic buckling loads are attributed to the lateral inertia force which counters the bending of the shallow arch formed by the bent brace.

The dynamic responses of the other two braces compare similarly with their static counterparts, but the degree of difference is dependent on the size of the braces. The effect of dynamics on the maximum compressive axial force is greater for slender braces than for stocky ones. For example, the dynamic peak compressive axial load for the $\square$ 4 × 4 × 1/2 brace is 780 kN, compared with its static counterpart of 480 kN, while the comparison for the $\square$ 8×8×1/2 brace is 2930 kN versus 2836 kN. More detailed comparison can be found in Table 2.9 on page 55.

High frequency vibrations are also observed in the time history plot of the mid-span lateral deflection in Figure 2.43 when the brace is straightened under tensile force. However, little of the vibrations are reflected in the axial force time history because the deflection is small and the brace vibrates more like a straight beam than an arch. It is interesting to observe that the high frequency vibrations diminish with each displacement cycle, probably because the tensile force is changing less abruptly with each cycle, both when the brace buckles under compression and when it is straightened under tension, as can be observed
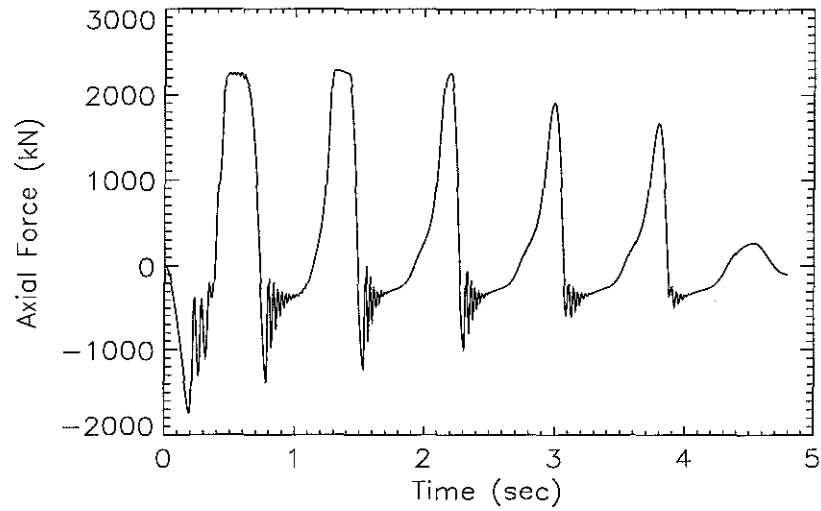
**Figure 2.41**: Dynamic response: Axial force time history for a □ 6 × 6 × 1/2 brace with pinned ends under end displacement H-08.
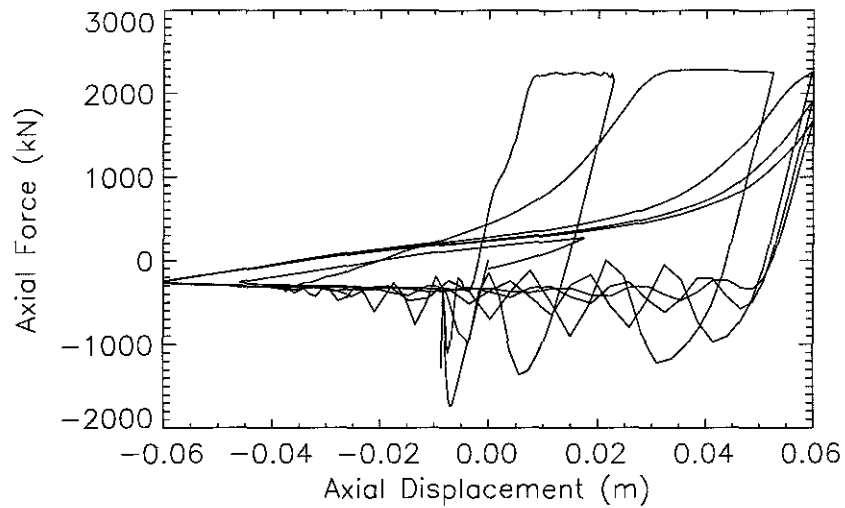


**Figure 2.42**: Dynamic response: Hysteresis loops for a □ 6 × 6 × 1/2 brace with pinned ends under end displacement H-08.
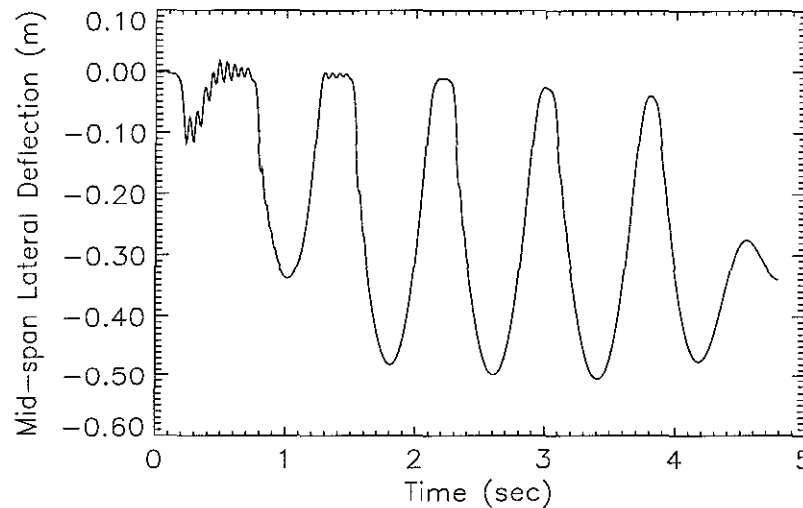
**Figure 2.43**: Dynamic response: History of mid-span lateral deflection for a □ 6×6×1/2 brace with pinned ends under end displacement H-08.

in Figure 2.42. Overall, the dynamic lateral deflection history does not differ much from the static one: The deflection is almost one-sided (mainly downward bending) and there is a significant residual lateral deflection after the end displacement vanishes.

The magnitude and distribution of fiber strains differ very little from those in static analysis, as can be seen by comparing Figure 2.44 with Figure 2.29 on page 30, both of which show the fiber strain distributions of the □ 6×6×1/2 brace from dynamic analysis and static analysis respectively. The same is also true for the other two braces.

Figure 2.45 shows the distribution of energy dissipation over the length of the 3 braces. Again, compared with the static analysis results shown in Figure 2.33 on page 32, not much difference can be observed.

The braces respond similarly to displacement history H-05, so the results are not discussed in detail. Summary results can be found in Figures 2.56~2.58 and Table 2.9 on page 55 in the later part of this section.

The above results show that the effect of inertia force under relatively long period end displacement inputs is mainly to increase the peak compressive force of the braces. As far as the global response of a braced structure is concerned, the effect of inertia on the brace
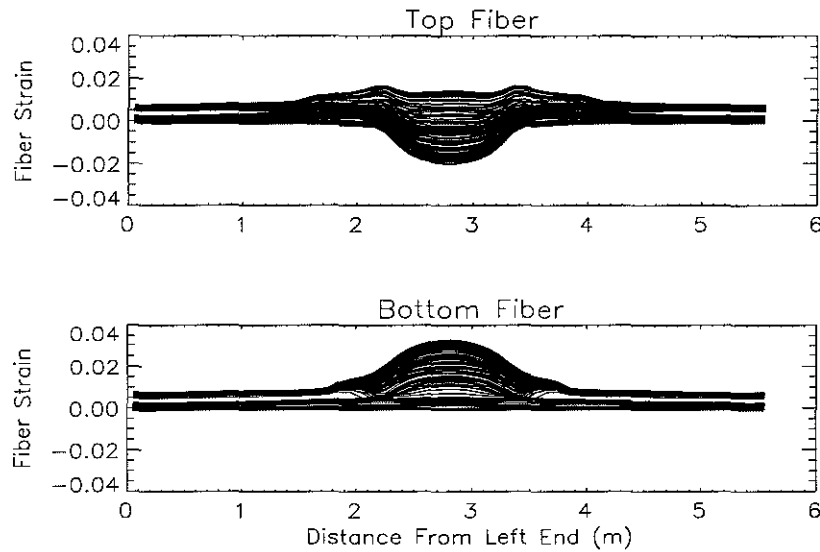
**Figure 2.44**: Dynamic response: Distribution of strains in the top and bottom fibers over the length of a □ 6×
6 × 1/2 brace with pinned ends under end displacement H-08.
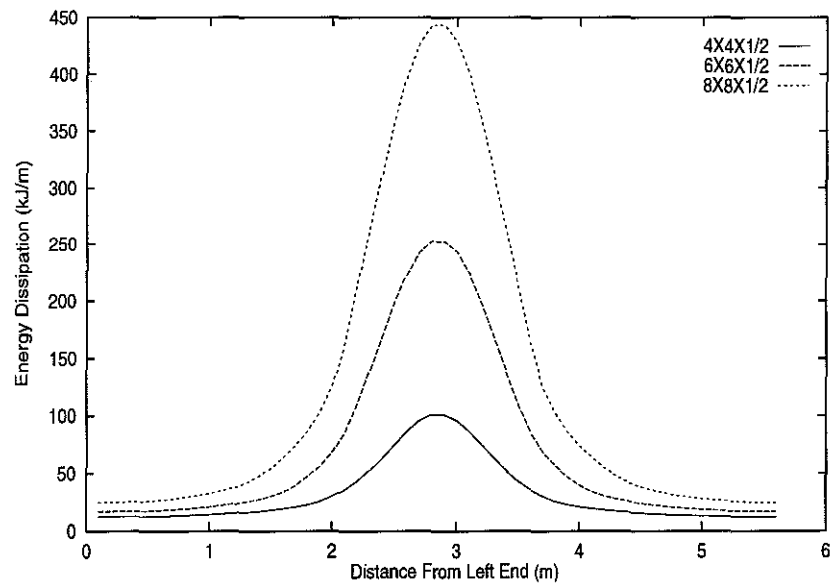


**Figure 2.45**: Dynamic response: Distribution of energy dissipation for □ 4×4×1/2, □ 6×6×1/2 and □ 8×8×1/2
braces with pinned ends under end displacement H-08 with 0.8 seconds period.

axial force can be viewed as a high frequency disturbance superimposed on the quasi-static response. Since the increase is momentary and the frequency of the disturbance is much higher than the frequency of the input, these effects are not expected to cause significant difference in the overall response of the whole structure. But localized effect on structural components adjacent to the braces is expected to be stronger. Based on this observation, neglecting the inertia of the braces and applying static condensation to the internal degrees of freedom would be appropriate for such a case. To be conservative, the compressive axial load capacity of the braces can be increased in the calculation of the internal forces of the immediately adjacent structural members to account for the dynamic effect.

## 2.4.2 Under Displacement H-02

Figures 2.46 and 2.47 show the axial force time history and the hysteresis loops, respectively, of the □ $6 \times 6 \times 1/2$ brace under end displacement history H-02. Compared with the results under end displacement history H-08, the effect of dynamics is more pronounced. The high frequency vibrations that accompany each buckling of the brace have larger amplitudes. The peak dynamic compressive axial force is much higher than its static counterpart (1200 kN versus 480 kN). The dynamic hysteresis loops bear much less resemblance to the static ones, as can be seen by comparing Figure 2.47 with Figure 2.23 on page 26.

Besides the above differences, the dynamic responses of the braces under H-02 show a number of fundamental differences compared with the foregoing results. The difference between the dynamic and static lateral deflections is more striking than in the case with H-08 and H-05. Under H-05 and H-08 the lateral deflections are basically one-sided downward bending because of the initial deflection caused by the weight of a brace. But under H-02 the □ $4 \times 4 \times 1/2$ brace is flipped over at about 0.45 sec in the time history and starts to bend mainly upward as shown in Figure 2.48, in despite of the initial downward deflection. The distribution of fiber strains over the length of the brace in Figure 2.49 shows that the deformation of the brace is still symmetric, although the shape is quite different from the result for static analysis shown in Figure 2.28 on page 29.
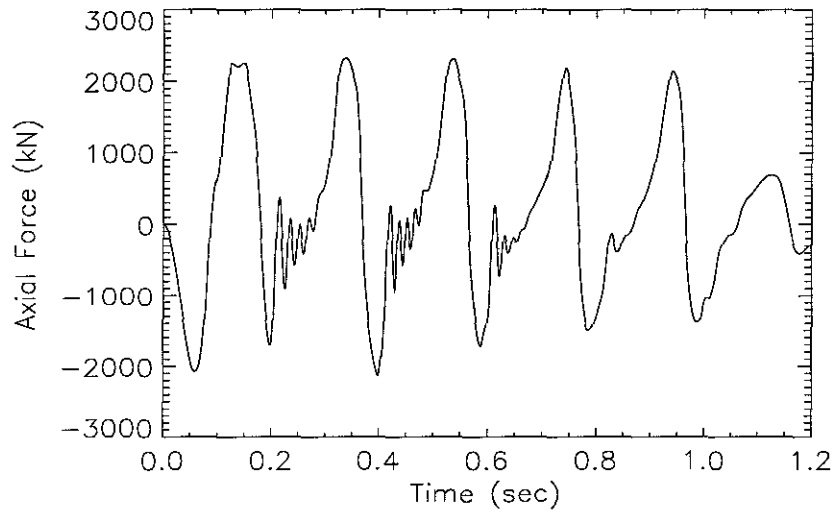
**Figure 2.46**: Dynamic response: Axial force time history for a □ 6 × 6 × 1/2 brace under end displacement H-02.
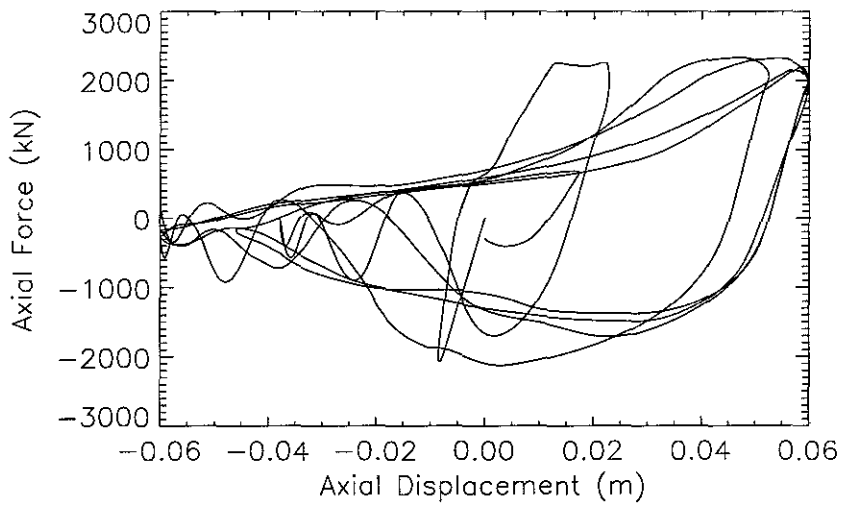


**Figure 2.47**: Dynamic response: Hysteresis loops for a □ 6 × 6 × 1/2 brace under end displacement H-02.

48
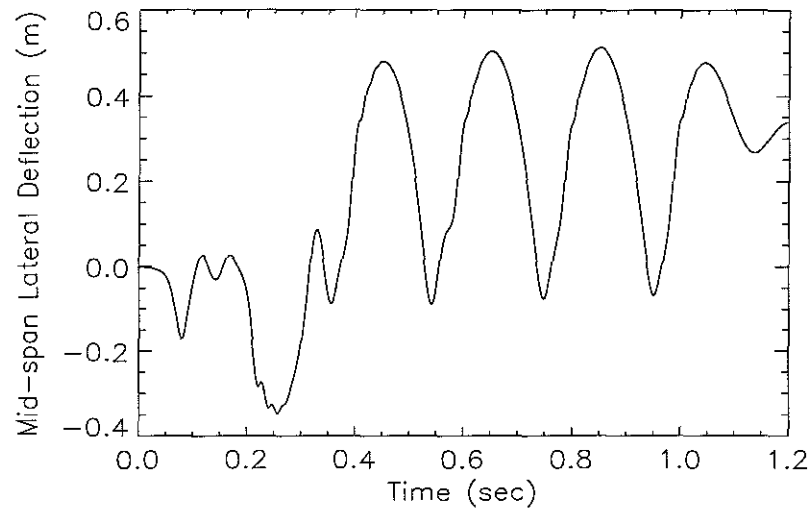


**Figure 2.48**: Dynamic response: History of mid-span lateral deflection for a □ 4 × 4 × 1/2 brace under end displacement H-02.
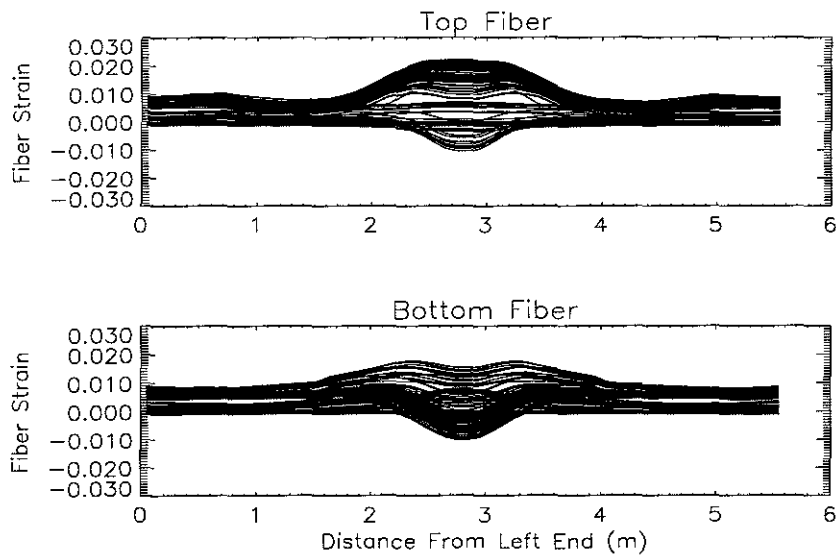


**Figure 2.49**: Dynamic response: Distribution of fiber strains in the top and lower over the length of a □ 4 × 4 × 1/2 brace under end displacement H-02.
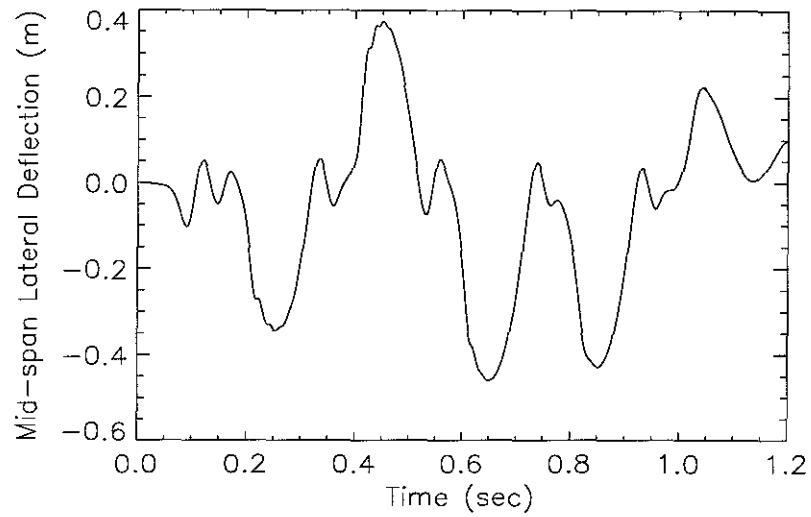
**Figure 2.50**: Dynamic response: History of the mid-span lateral deflection of a □ 6×6×1/2 brace with pinned ends under end displacement H-02.
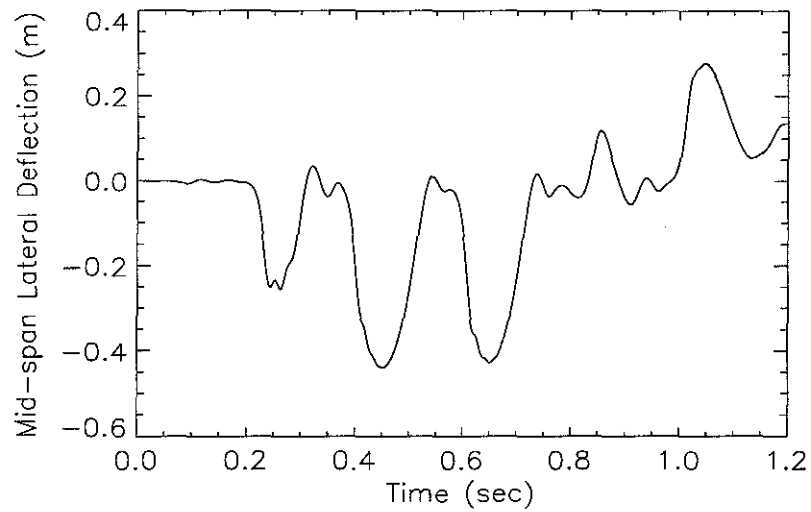


**Figure 2.51**: Dynamic Response: History of the mid-span lateral deflection for a □ 8 × 8 × 1/2 brace with pinned ends under end displacement H-02.

50
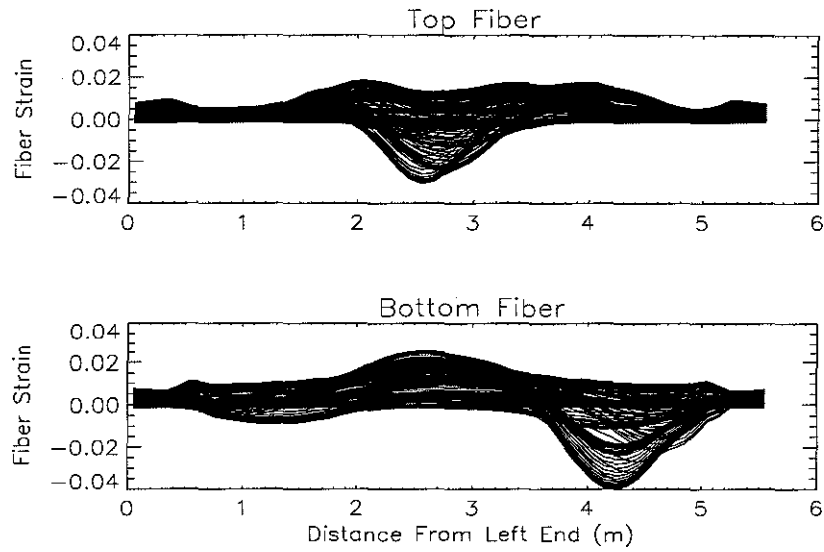


**Figure 2.52**: Dynamic response: Distribution of fiber strains in the top and lower over the length of a □ 6 × 6 × 1/2 brace with pinned ends under end displacement H-02.
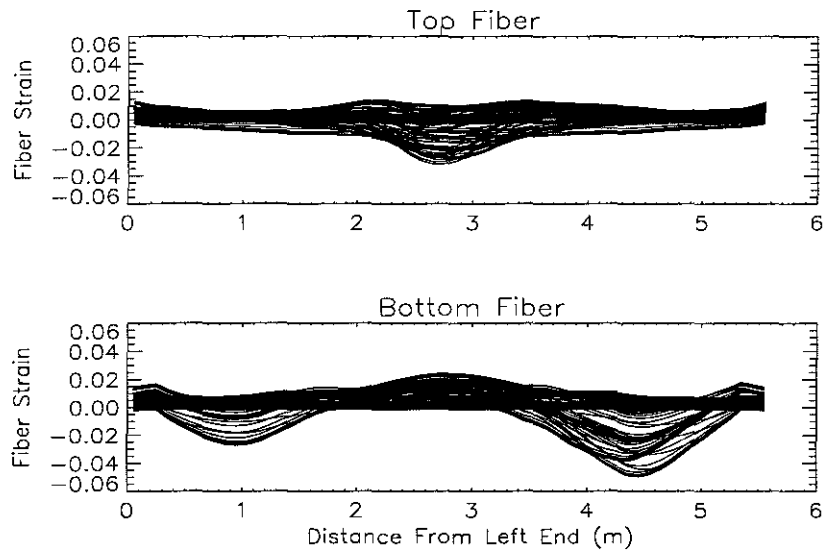


**Figure 2.53**: Dynamic response: Distribution of fiber strains in the top and lower over the length of a □ 8 × 8 × 1/2 brace with pinned ends under end displacement H-02.
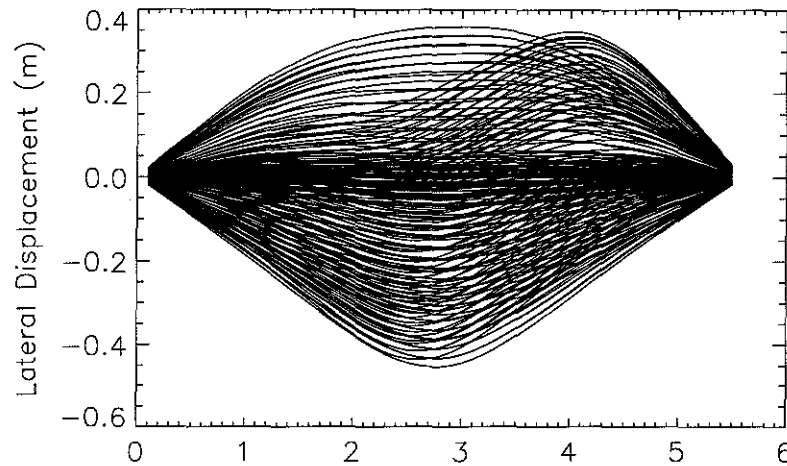
**Figure 2.54**: Dynamic response: Distribution of lateral deflection over the length of a □ 6×6×1/2 brace with pinned ends under end displacement H-02.

The same phenomenon also occurs in the other two braces, as is evidenced by the mid-span lateral deflection histories shown in Figures 2.50 and 2.51. But more fundamental departure from the quasi-static behavior is revealed in Figures 2.52 and 2.53 which plot the fiber strain distribution over the length of the braces. The figures show that the deformation of the two braces is no longer symmetrical and the maximum compressive fiber strain occurs at a point away from the mid-span. For the □ 6×6×1/2 brace, the unsymmetrical deformation can be clearly seen in Figure 2.54, which plots the distribution of the lateral deflection of the brace at different stages of the time history. The unsymmetry is also reflected in the distribution of energy dissipation in Figure 2.55.

It is not entirely clear why the braces develop unsymmetrical deformation. One possible explanation is that this is the result of anti-symmetrical buckling that often occurs in arches under distributed lateral load. When a brace is bent under axial compression, it may behave like such an arch, with the inertia force acting as the lateral load. For an arch whose height to chord ratio is within a certain range, the lowest buckling mode is anti-symmetric. The buckling load can be small in for the braces under study because of significant yielding. This result indicates that even a perfect brace can fail at some point other than the mid-span
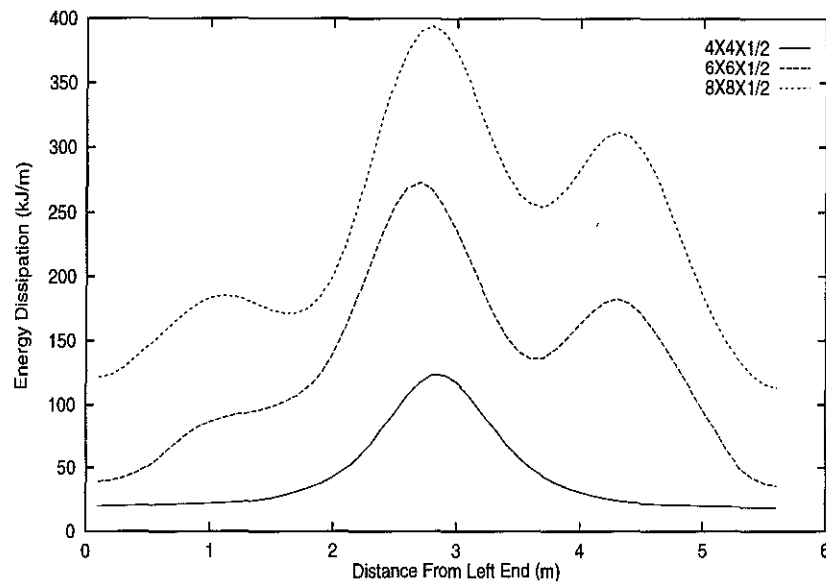
**Figure 2.55**: Dynamic response: Distribution of energy dissipation of braces under end displacement H-02.

since the maximum compressive strain occurs about a quarter of the length away from one of the ends, as is shown in Figures 2.52 and 2.53. Obviously this mode of deformation can not be predicted by static analysis.

## 2.4.3 Summary Comparison

The dynamic response of individual braces under a set of end displacement inputs with different frequencies has been the focus of this section. The study shows that the dynamic behavior of the braces under high frequency displacement inputs can be significantly different from that predicated by static analysis. Among the most striking differences are the phenomena of flip-over and unsymmetrical deformation which occur only when the inertia force of the braces is included in the analysis.

To facilitate comparison, some of the important response quantities are plotted against the frequencies of the inputs in Figures 2.56~2.58 and summarized in Table 2.9 on page 55. Each response quantity in the figures is normalized to the corresponding quasi-static value. The quasi-static response can be viewed as a special case of dynamic response under end displacement input with infinitely long period.
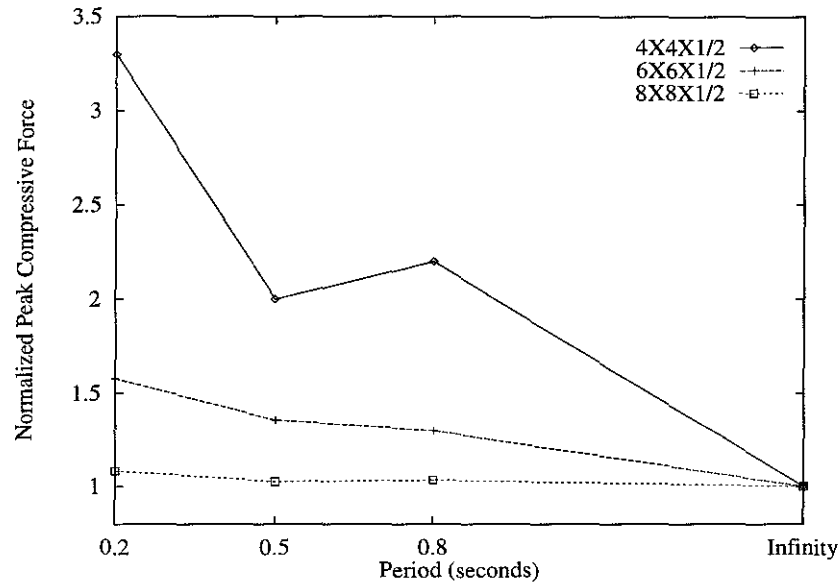
**Figure 2.56**: Normalized peak compressive axial forces of braces □ 4×4×1/2, □ 6×6×1/2 and □ 8×8×1/2 with pinned ends under different end displacement inputs. The peak compressive force of each brace under different inputs is normalized to the corresponding quasi-static value.

Figure 2.56 illustrates the dependence of the maximum peak compressive axial forces of the braces on the period of the end displacement inputs. It is seen that higher frequency normally means larger peak compressive axial force. But the degree of dependency is different for braces of different sizes, with the axial force of slender braces more susceptible to the effect of the input frequencies. For the □ 4×4×1/2 brace, the peak compressive axial force (1200 kN) under H-02 is about 3.3 times that from quasi-static analysis (362 kN), much higher than the Euler critical load (394 kN) and approaching the yielding axial load of the brace (1433 kN, see Table 2.2 on page 17). But for the □ 8×8×1/2 brace, the effect of the frequency on its peak axial force is barely noticeable.

The insensitivity of the axial force of the stocky □ 8×8×1/2 brace to the input frequencies is attributed to the fact that the peak compressive axial force capacity of 2836 kN under quasi-static loading is already close to its axial yield force of 3075 kN (Table 2.2). There is little room for the axial force to increase any further when inertia is considered. The axial force capacity of a brace is limited by its axial yield capacity because the axial acceleration is relatively small.
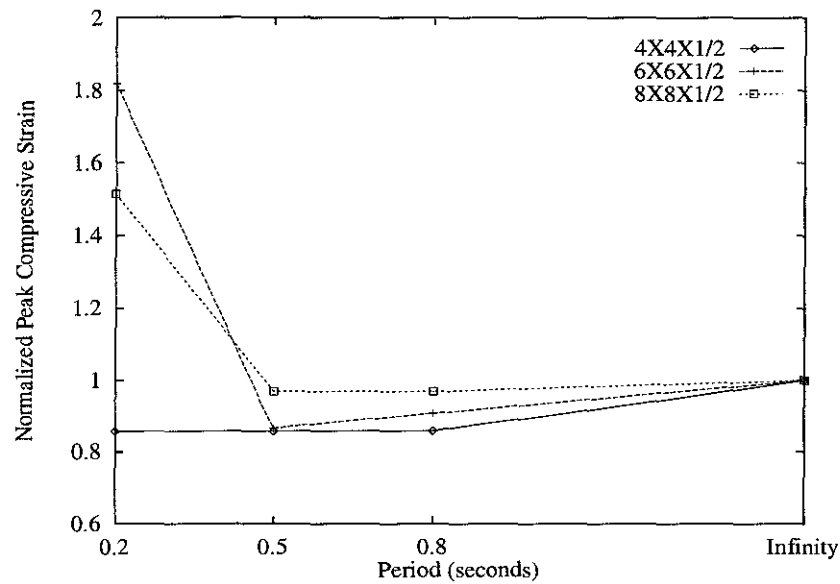
**Figure 2.57**: Normalized peak compressive strains of braces □ 4 × 4 × 1/2, □ 6 × 6 × 1/2 and □ 8 × 8 × 1/2 with pinned ends under different end displacement inputs. The peak compressive strain of each brace under different inputs is normalized to the corresponding quasi-static value.

The closeness between the peak compressive axial force and the axial yield capacity for the □ 6 × 6 × 1/2 and □ 8 × 8 × 1/2 braces also explains why they develop unsymmetrical displacement under input H-02, while the slenderer □ 4 × 4 × 1/2 brace does not. The reasoning is that, when the axial force in a brace is close to its yield capacity, yielding will occur over a large part of its cross-section. To maintain the axial force level, when further bending occurs, most of the fibers over the cross-section will experience new plastic incursion, thus resulting in small tangent bending stiffness and unsymmetrical buckling of the arched brace ensues under the lateral inertia force. For a slender brace, bending moment dominates, and when further bending occurs, significant portion of the fibers will experience unloading, thus resulting in higher tangent bending stiffness and higher buckling load.

The effect of the input frequencies on the peak compressive fiber strains of the braces is less uniform than on the peak axial force, as shown in Figure 2.57. In all cases, the effect is small for period longer than 0.5 seconds. However, under H-02, which has a period of 0.2 seconds, the peak compressive fiber strains in the □ 6×6×1/2 and □ 8×8×1/2 braces are about 80% and 50% higher, respectively, than the corresponding values from quasi-static

55

| Size of Braces | | □ 4×4×1/2 | □ 6×6×1/2 | □ 8×8×1/2 |
|---|---|---|---|---|
| Static | Energy Dissipation (kJ) | 165 | 376 | 678 |
| | Energy Dissip. Eff. | 0.52 | 0.76 | 1.00 |
| | Peak Compression (kN) | 362 | 1350 | 2836 |
| | Peak Tensile Strain | 2.6% | 3.2% | 3.6% |
| | Peak Compressive Strain | -1.4% | -2.2% | -3.3% |
| $T = 0.8$ sec | Energy Dissipation (kJ) | 177 | 396 | 704 |
| | Energy Dissip. Eff. | 0.54 | 0.77 | 1.00 |
| | Peak Compression (kN) | 780 | 1750 | 2930 |
| | Peak Tensile Strain | 2.5% | 3.2% | 3.6% |
| | Peak Compressive Strain | -1.2% | -2.0% | -3.2% |
| $T = 0.5$ sec | Energy Dissipation (kJ) | 174 | 405 | 779 |
| | Energy Dissip. Eff. | 0.48 | 0.71 | 1.00 |
| | Peak Compression (kN) | 720 | 1830 | 2910 |
| | Peak Tensile Strain | 2.8% | 3.2% | 3.2% |
| | Peak Compressive Strain | -1.2% | -1.9% | -3.2% |
| $T = 0.2$ sec | Energy Dissipation (kJ) | 238 | 742 | 1302 |
| | Energy Dissip. Eff. | 0.39 | 0.79 | 1.00 |
| | Peak Compression (kN) | 1200 | 2130 | 3070 |
| | Peak Tensile Strain | 2.2% | 2.6% | 2.5% |
| | Peak Compressive Strain | -1.2% | -4.0% | -5.0% |

Table 2.9: Summary of dynamic responses of braces with pinned ends under cyclic end displacements that have the same peak amplitude but different frequencies. The energy dissipation efficiency is defined by dividing the energy dissipation of a brace with its cross-sectional area and normalized such that the efficiency of the □ 8×8×1/2 brace is 1.

analysis, although the peak fiber strain in the □ 4 × 4 × 1/2 brace is slightly lower. The difference is probably related to the fact that the former two braces develop unsymmetrical deformation. In terms of absolute value, the peak compressive fiber strains in the □ 4×4× 1/2, □ 6×6×1/2 and □ 8×8×1/2 braces under H-02 are 1.2%, 4.0% and 5.0%, respectively. The last two braces have particularly large fiber strains, and there is reason to doubt that they can survive the deformation without local buckling and rupture.
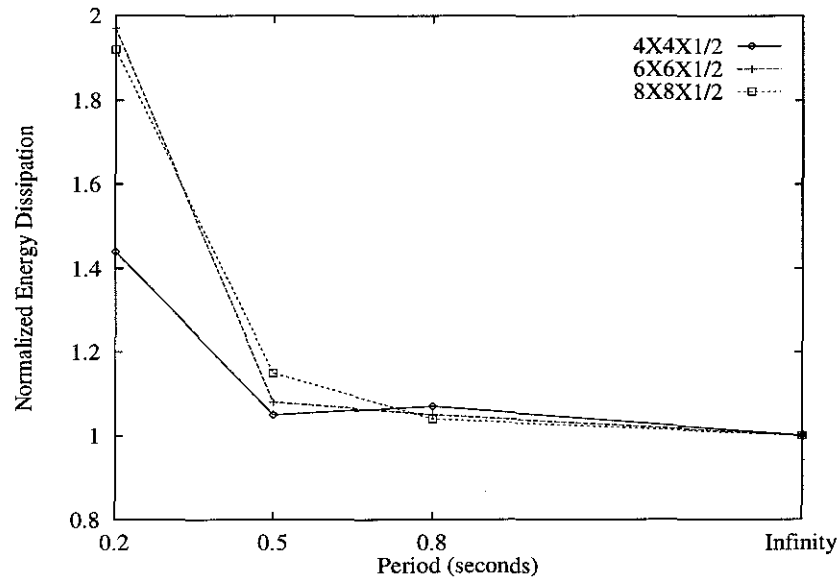
**Figure 2.58**: Normalized energy dissipations of braces □ 4×4×1/2, □ 6×6×1/2 and □ 8×8×1/2 with pinned ends under different end displacement inputs. The energy dissipation of each brace under different inputs is normalized to the quasi-static value.

The energy dissipation of the braces is shown in Figure 2.58. Generally, higher frequency of the end displacement input increases the energy dissipation of a brace. This is especially true for the □ 6 × 6 × 1/2 and □ 8 × 8 × 1/2 braces. Again, for the braces considered the difference is small for periods longer than 0.5 seconds.

# 2.5 Conclusions

The quasi-static and dynamic behaviors of individual bracing members under different end displacement inputs have been studied using a fiber element model. The study focuses on

the internal deformation and the effect of dynamics on the response of the braces and has yielded some interesting findings, based on which the following conclusions are made:

1. For displacement inputs with relatively long period (greater than 0.5 seconds for the braces considered in this study), the inertia force of the braces does not have significant effect on the peak fiber strain, energy dissipation and deformation pattern. However the effect on the peak compressive axial force can be significant. The effect of inertia on the axial force time history of a brace takes the form of high frequency disturbance superimposed on the quasi-static response. Since this increase is momentary and the disturbance has a frequency much higher than that of the input, it is not expected to have significant impact on the overall response of the entire structure except for the localized effect on the internal forces of the structural components adjacent to the braces. Base on this observation, static condensation used to eliminate the internal degrees of freedom of the braces seems to be a reasonable approximation if the possible effect on the adjacent structural components is properly accounted for.

2. For displacement inputs with relatively short period (less than 0.2 seconds for the braces considered in this study), the effect of lateral inertia on most response quantities is significant. Specifically, it can substantially increase the peak compressive axial force, compressive fiber strains and energy dissipation, and static treatment would be seriously in error. In stocky braces whose peak compressive force is close to the uniform yield axial force, high frequency input can result in unsymmetrical deformation that can not be predicted by quasi-static analysis. This unsymmetrical deformation seems to increase the maximum compressive fiber strain and the energy dissipation of such braces. Compared with the strain rate effect [31], the effect of inertia can be more significant for braces under certain conditions.

3. The distribution of fiber strain over a brace under axial end displacement is highly uneven, and strain concentration occurs. The maximum strain can be several times the equivalent uniform strain. The size of a brace affects its strain distribution and mag-

nitude. Slender braces often have more severe strain concentration. But the maximum compressive strain, which is related to local buckling and is therefore more important, is often higher in stocky braces.

4. The lateral deflection and fiber strain of a brace under cyclic end displacement are usually larger than under monotonic end displacement of the same magnitude, and the maximum lateral deflection is about an order larger than the corresponding axial end displacement.

5. Eccentricity of a brace has significant effect on its compressive axial load capacity only in the vicinity of initial buckling since after the buckling occurs the lateral deflection is much larger than the eccentricity.

Some aspects of the response of braces under cyclic end displacement are not considered in this study. Among these are the consideration of cross-sectional deformation and local buckling, both of which have been observed in laboratory testings [3, 7, 28]. The effect of the dynamics of the braces on the overall response of a structure also needs to be further studied.

# Chapter 3

# Frames With Column Uplift

## 3.1 General

In light of the failures of braced steel frame structures during the Northridge and Kobe earthquakes, the idea of allowing column uplift in the braced bays has been floating around among some practicing engineers. The purpose of this chapter is to study the effect of column uplift and to explore the feasibility of flexible column anchoring. The fiber element model in [10] is used in the analysis of this chapter.

## 3.2 Frames With Column Uplift

A special six-bay four-story steel frame, which represents one of the two longitudinal frames of a one-bay by six-bay building, was designed for the purpose of this study. The configuration and dimensions of the frame are shown in Figure 3.1. The loading condition for the frame is as following: 1771 kN dead load and 518 kN effective live load for each floor, 1484 kN dead load and 518 kN effective live load for the roof. The dead loads contribute to both the reactive mass and the static load, while the live loads contribute only to the static load. The material used for the beams and columns has a yield strength of 248 MPa and an ultimate strength of 400 MPa. The corresponding values for the braces are 345 MPa and 448 MPa, respectively.

The frame consists of five vertical load-carrying (VLC) bays and one X-braced bay. The VLC bays are designed to carry primarily vertical load and to be ductile and flexible in the

horizontal direction, while the horizontal resistance of the frame is to be resisted primarily by the X-braced bay. The ductility of the beam-to-column connections in the VLC bays, other than their strength, will dictate the type of connections to be used. Because of this condition, bolted connections are likely to be a more suitable choice than welded ones, but due to lack of suitable model, the beam-to-column connections of the VLC bays are simulated with the panel zone model in [10], with the strength reduced by half to consider the lower strength requirement.
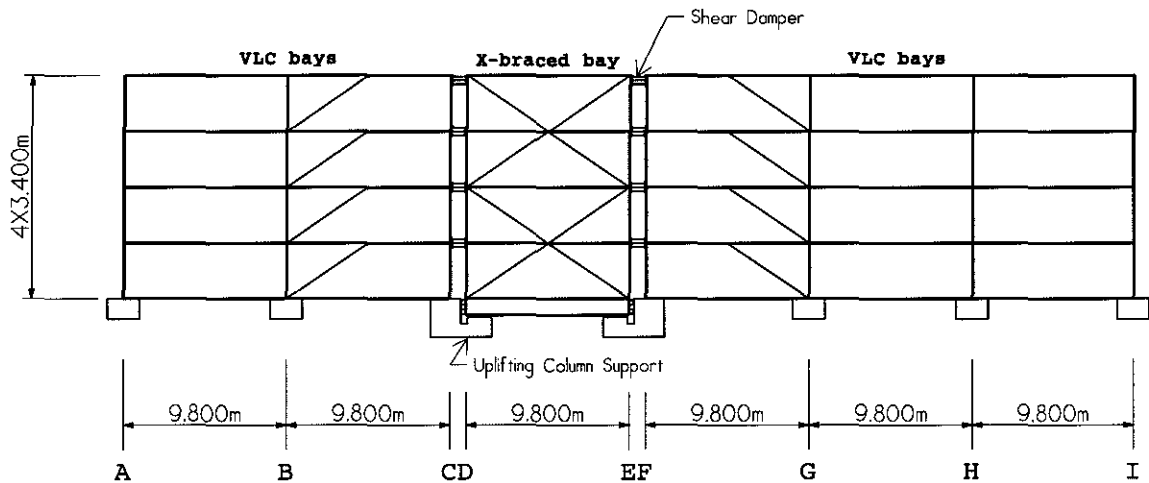


Figure 3.1: Frame considered in Chapter 3.

While the VLC bays will have the usual fully anchored column bases, several column-base anchoring conditions, with one being fully anchored and the others allowing uplift, are considered for the X-braced bay. For frames with uplifting columns, to isolate the uplift displacement to the X-braced bay, the VLC bays and the X-braced bay are separated by a slide mechanism which permits the two adjacent columns between the two types of bays to have different vertical displacements but maintains the same horizontal displacement. In all cases, the bases of the X-braced-bay columns are always fixed in the horizontal direction. Based on the vertical column-base anchoring conditions of the X-braced bay, the following versions of the frame are considered:

FIXED:    All columns have completely anchored bases. This frame is intended to simulate conventional frames without column uplift.

UPLIFT1:  Columns in the X-braced bay are free to uplift. The supporting surface is sta-
tionary and pounding is possible. This type of column-base support condition
is simulated by a bi-linear spring with a loading curve shown in Figure 3.2(a).

UPLIFT2:  Columns in the X-braced bay are flexibly anchored with steel tie-down tendons
prestressed to their yield stress. The supporting surface is assumed to follow a
column as it lifts off, so the uplift is cumulative and there is no pounding. This
type of column-base support condition is simulated by a spring with a loading
curve shown in Figure 3.2(b). Since the tie-down tendons are fully prestressed,
they have a rigid-perfectly plastic loading curve. Tendon force capacities ran-
ging from 500 kN to 3000 kN for each column are considered.

UPLIFT3:  Columns have similar base support as in frame UPLIFT1, but the X-braced-
bay column at each side is connected with the adjacent VLC-bay column with
shear dampers. The dampers have a loading curve shown in Figure 3.3. As
with UPLIFT2, total damper shear capacities at each side of the X-braced bay
ranging from 500 kN to 3000 kN are considered. The yield displacement of the
dampers is taken to be 0.014 meters, and the linear stiffness is calculated from
the shear capacity and the yield displacement.



(a) Up-and-down Support          (b) Up-only Support
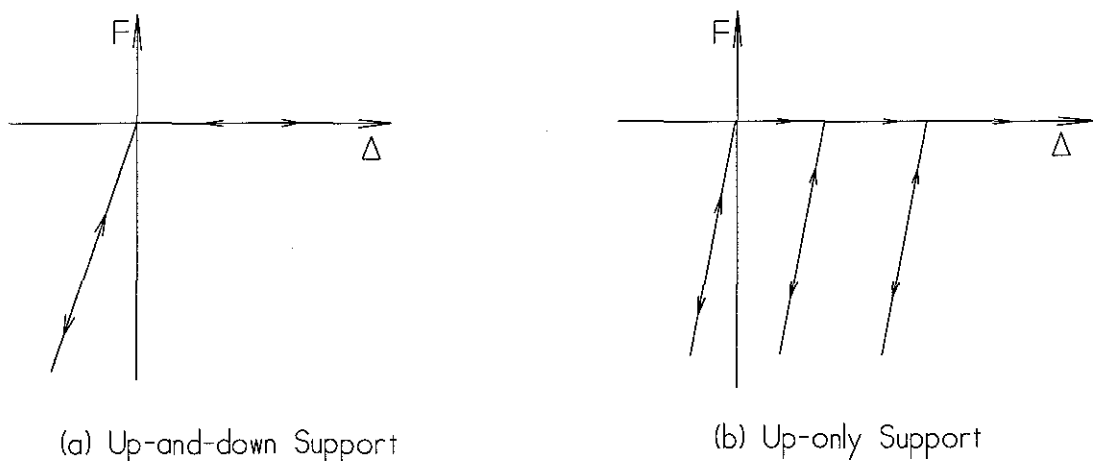
Figure 3.2: Loading curves for springs that simulate two types of supports for uplifting columns.
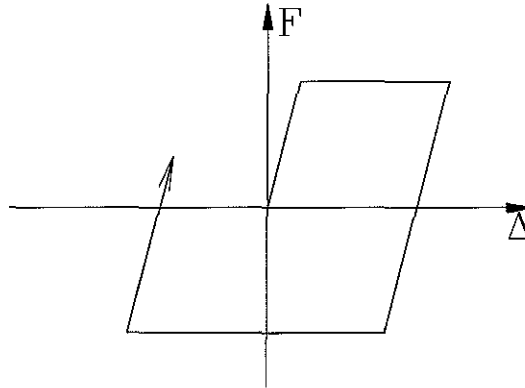
**Figure 3.3**: Loading curves for shear dampers.

For the frames that allow column uplift, the uplifting X-braced bay is designed to have high stiffness and strength and remain elastic during an earthquake to force deformation into the tie-down tendons in the case of frame UPLIFT2, or into the shear dampers in the case of frame UPLIFT3. Based on this concept the member sizes for the frames are designed as shown in Table 3.1. For comparability, the same member sizes are used for frame FIXED, although they exceed code requirement by a large margin, as can be seen in the push-over results shown in Figure 3.4.

The push-over results were obtained by subjecting the frames to static lateral forces with a vertical distribution calculated according to the Uniform Building Code. For frames UP-LIFT2 and UPLIFT3, an uplift restraint of 1500 kN under each uplifting column is used. The base shear coefficient in the figure is defined as the ratio between the base shear and the total reactive weight of a frame and is related to the value

$$C_s = \frac{ZIC}{R_w} \tag{3.1}$$

in the Uniform Building Code. The push-over loading curves in Figure 3.4 were traced up to the point where the program reported "fiber rupture", which often means that the fiber strain has exceeded the maximum allowable value because of the oscillation in the iteration process.

The one-legged braces in the VLC bays are intended to provide lateral resistance reserve

| Story | Columns | | Braces | |
|---|---|---|---|---|
| | VLC bays | X-braced bays | VLC bays | X-braced bays |
| 4th | 10W33 | 14W43 | □6×6×3/8 | □12×12×1/2 |
| 3rd | 12W40 | 14W74 | □6×6×3/8 | □12×12×1/2 |
| 2nd | 12W50 | 14W145 | □6×6×3/8 | □16×16×1/2 |
| 1st | 14W61 | 14W159 | □6×6×3/8 | □16×16×1/2 |

(a) Columns and braces

| Floor | 1st | 2nd | 3rd | 4th | Roof |
|---|---|---|---|---|---|
| VLC Bays | 16W40 | 16W40 | 16W40 | 16W40 | 14W30 |
| X-braced Bay | 14W132 | 16W100 | 16W100 | 16W67 | 16W40 |

(b) Beams

**Table 3.1**: Member sizes for the frames.
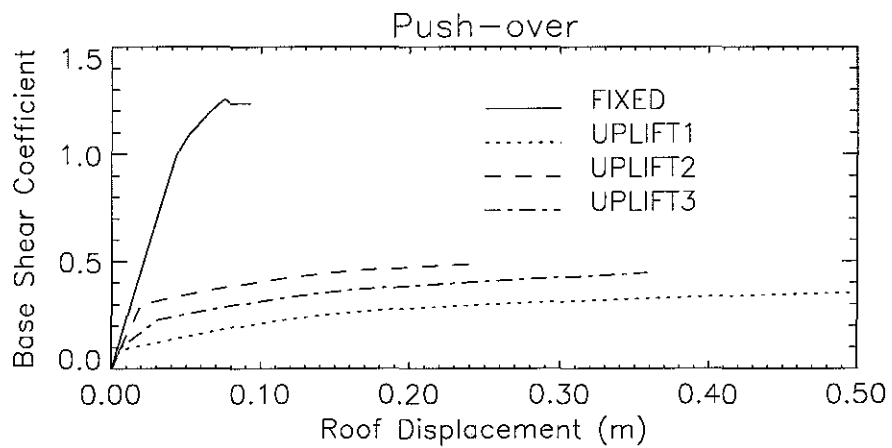


**Figure 3.4**: Push-over results for the four frames. The figure plots the base shear coefficient versus the roof displacement. The uplift restraint per column for frames UPLIFT2 and UPLIFT3 is 1500 kN.
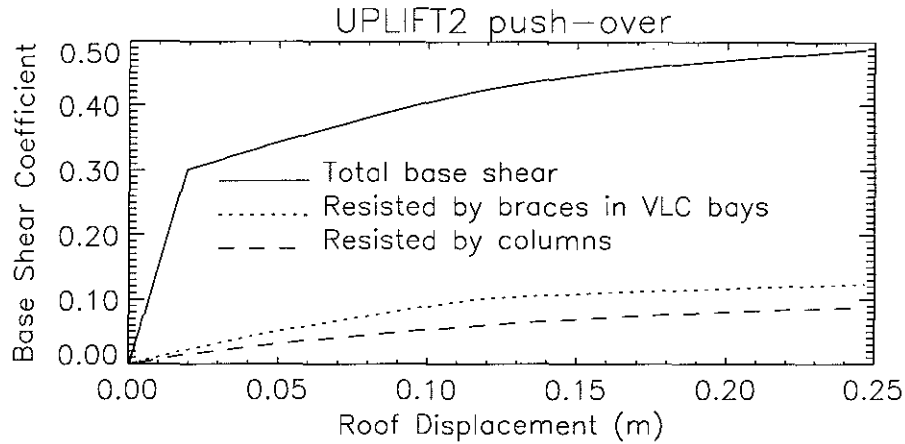
**Figure 3.5**: Base shears resisted by different parts of frame UPLIFT2 during push-over. The uplift restraint per column is 1500 kN.

once column uplift occurs. These braces provide base shear resistance that has a large elastic range because of the flexibility of the beams above them. Before column uplift occurs, they provide only a very small fraction of the total base shear. But their share of the base shear increases after column uplift occurs, as shown in Figure 3.5 for frame UPLIFT2. It is seen from the figure that the base shear resisted by these braces increases almost linearly up to a roof displacement of 0.11 meters, while the total base shear curve exhibits yielding at a roof displacement of 0.02 meters.

The magnitude of the anchoring force for the X-braced bay is the most important parameter that affects the behavior of the frame. It determines the maximum horizontal resistance that the X-braced bay can provide. It also affects the maximum internal forces produced in the members of the X-braced bay. A small anchoring force makes uplifting easy and thus provides less horizontal resistance. A very large anchoring force turns the X-braced bay into a completely anchored bay. With optimal anchoring force the X-braced bay may provide sufficient horizontal resistance and at the same time keep the forces in its members below an acceptable level. The column uplift restraint also provides an energy dissipation mechanism.

# 3.3   Effect of Uplift Restraint

Uplift restraint is an important parameter in frames that allows column uplift. Before studying the behavior of such frames, a basic understanding of this parameter's effect is necessary. For the X-braced bay with up-only support, the uplift restraint is provided by tie-down tendons prestressed to their yield capacity. For the X-braced bay with up-and-down support, the restraint is provided by shear dampers. The effect of the uplift restraint force on the response of the frames is studied by varying the tension capacity of the tie-down tendons or the shear capacity of the dampers and subjecting the frames to ground acceleration time history B-1 [32] scaled to 1.0 g peak acceleration. The seemingly exceedingly large peak acceleration is partially justified by two recent earthquake ground motion records, which produce response of similar level in the structures as can be seen later in this chapter. The scaling here does not affect the frequency contents of the ground motions. Details on the ground motions and their scaling are included in Appendix B on page 151.

## 3.3.1   Tie-Down Tendons

Frame UPLIFT2 with uplift restraint force (tie-down tendon capacity in this case) ranging from 500 kN to 3000 kN under each column of the X-braced bay was subjected to the above ground motion. Response parameters, including energy dissipation, peak base shear, member forces and story drifts, are plotted versus the uplift restraint capacity.

Figure 3.6 shows the effect of the tie-down tendon capacity on the energy demand on different structural components of the frame, excluding the energy dissipated by the tie-down tendons themselves. It is seen that increasing the tie-down tendon capacity generally reduces the overall plastic energy demand, but the reduction is insignificant when the capacity is over 1500 kN. In fact, here the energy demand on the beam-column connections increases slightly with the increase of the tie-down tendon capacity. In the range of tie-down tendon capacity considered, no buckling or yielding of the braces occurs, and so the plastic energy demand on the braces is zero. From this figure, it is concluded that allowing free column

uplift in the X-braced bay results in large energy demand on the frame and so is not acceptable.
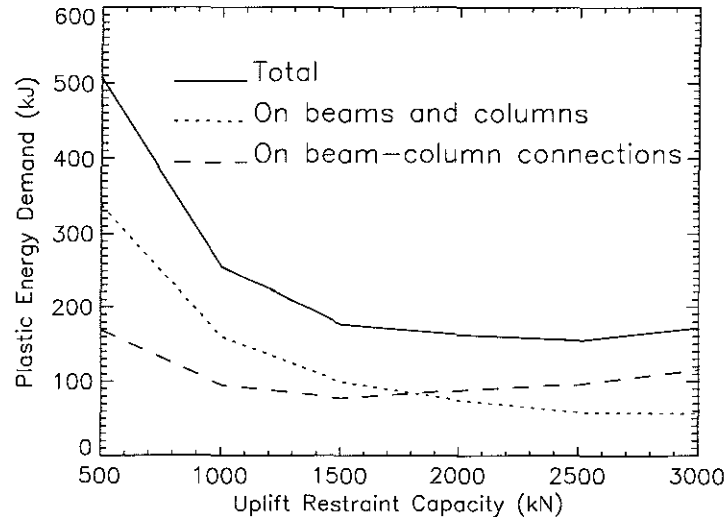


**Figure 3.6**: Effect of tie-down tendon capacity on the plastic energy demand on structural components for UPLIFT2 under ground motion $B_1$ scaled to 1.0g peak acceleration.

Figure 3.7 shows the effect of the uplift restraint force on the energy that is converted into plastic energy of the tie-down tendon and into gravitational potential of the X-braced-bay through uplift. The energy dissipated through uplift increases with the increase of the tie-down tendon capacity until it peaks at about 2500 kN, after which the energy thus dissipated decreases with the increase of tie-down tendon capacity. This is what one would expect since larger column uplift restraint makes the behavior of the frame more like that of a completely-anchored frame.

Plotted in Figure 3.8 are the peak total base shear and its breakdown into the amounts carried by the VLC bays and the X-braced bay. Both the total peak base shear and the base shear carried by the X-braced bay increases with the uplift restraint force, while the peak base shear in the VLC bays follows an opposite trend. Note that the sum of the peak base shears in the VLC bays and the X-braced bay does not equal the peak total base shear because the two peaks do not always occur at the same time. In fact the time history of the X-braced-bay base shear has a higher frequency content than that of the base shear in the
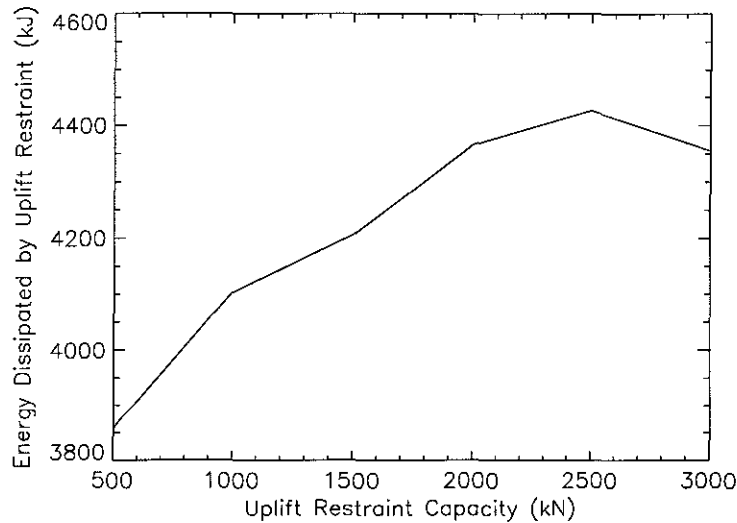
**Figure 3.7**: Relation between tie-down tendon capacity and the energy dissipated by the tendons and gravity in frame UPLIFT2 under ground motion B-1 scaled to 1.0g peak acceleration.

VLC bays. The increase of uplift restraint also increases the axial force in the X-braced-bay columns, as is shown in Figure 3.9.

Figures 3.10 and 3.11 show the story drifts of the VLC bays and the deformational story drifts of the X-braced bay, respectively, under different tie-down tendon capacities. The deformational drift of a story in the X-braced bay is the part of the story drift due to deformation of the frame, and is defined as the total story drift minus the drift associated with rigid rotation caused by uplift. From the figure one can see that increasing the tie-down tendon capacity reduces the story drifts of the VLC bays but increases the deformational story drifts of the X-braced bay, but the magnitude of the latter is much smaller than the former.

The final column uplifts of the X-braced bay with different tie-down tendon capacities are plotted in Figure 3.12. As is expected, increasing the uplift restraint reduces the amount of column uplift. But the magnitude of uplift is very significant even with a restraint force capacity of 3000 kN. A more realistic indication of the uplift magnitude will be obtained with the Sylmar and Kobe earthquake ground motions later in this chapter.
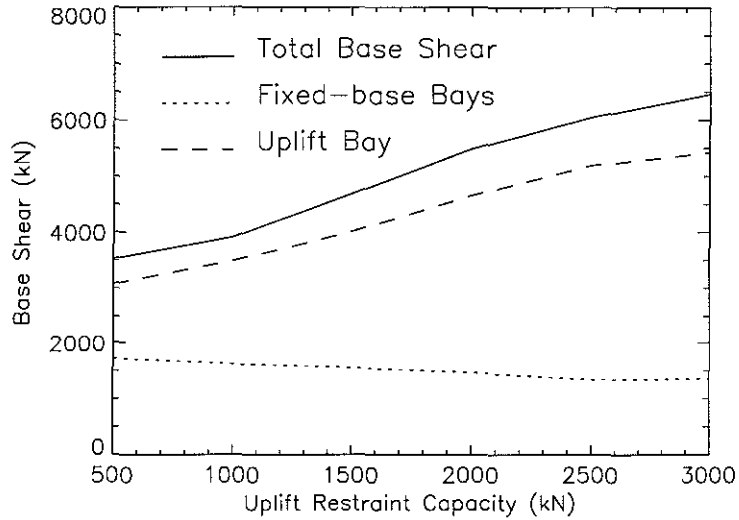
**Figure 3.8**: Effect of tie-down tendon capacity on the peak base shears of frame UPLIFT2 under ground motion B-1 scaled to 1.0g peak acceleration.
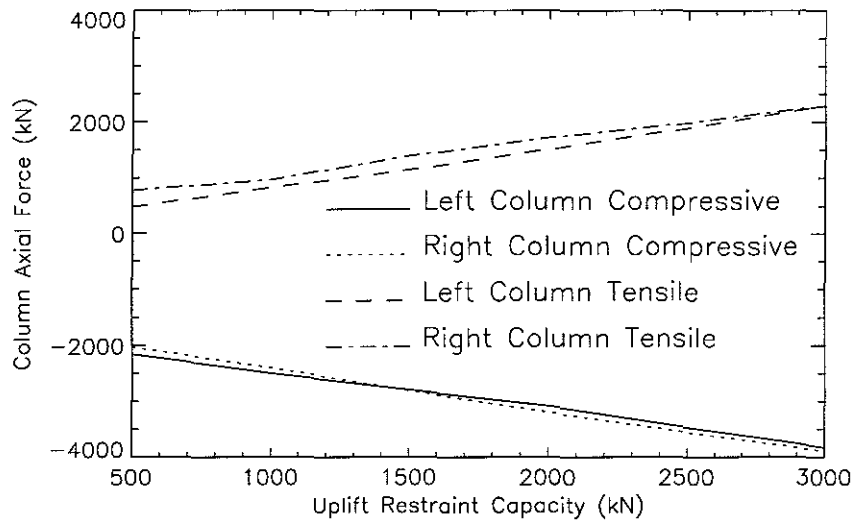


**Figure 3.9**: Peak axial force in the first story columns of the X-braced bay under different tie-down tendon capacities in frame UPLIFT2 under ground motion B-1 scaled to 1.0g peak acceleration.
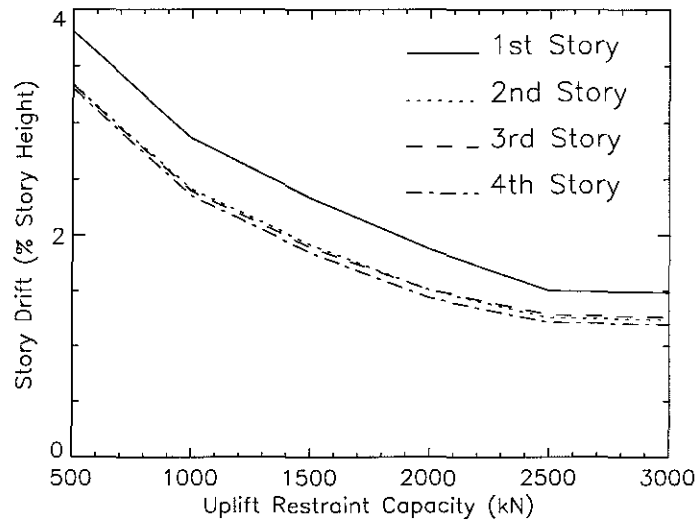
**Figure 3.10**: Effect of tie-down tendon capacity on the peak story drifts of the VLC bays of frame UPLIFT2 under ground motion B-1 scaled to 1.0g peak acceleration.
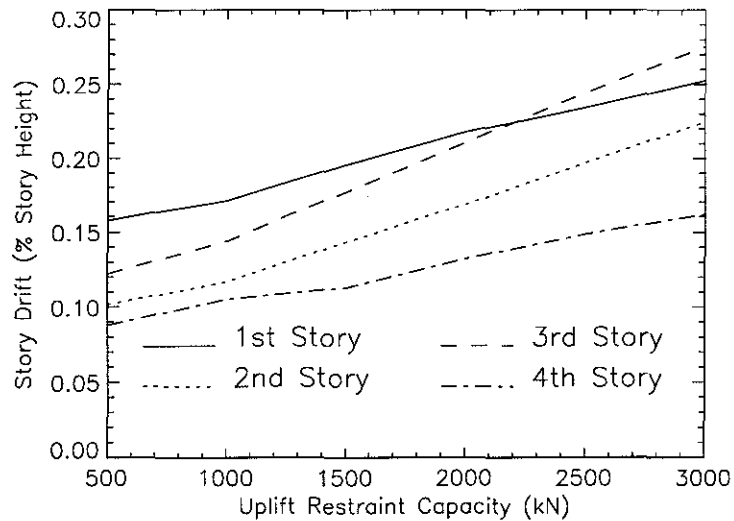


**Figure 3.11**: Effect of tie-down tendon capacity on the peak deformational story drifts of the X-braced bays in frame UPLIFT2 under ground motion B-1 scaled to 1.0g peak acceleration.
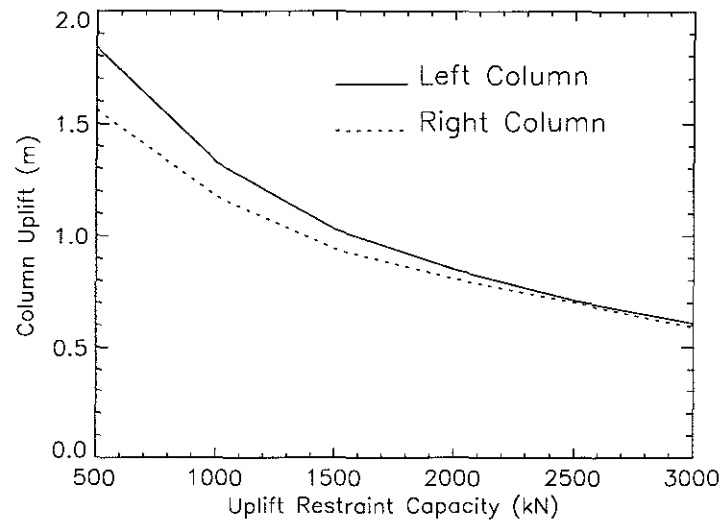
**Figure 3.12**: Effect of tie-down tendon capacity on the final amount of column uplift in frame UPLIFT2 under ground motion B-1 scaled to 1.0g peak acceleration.

## 3.3.2 Shear Dampers

The shear dampers between the uplifting X-braced bay and its adjacent VLC bays provide uplift restraint and energy dissipation. To study the effect of the shear capacity of the dampers, frame UPLIFT3 with a combined damper shear capacity on each side of the X-braced bay ranging from 500 kN to 3000 kN was subjected to B-1 ground motion scaled to a peak acceleration of 1.0 g. The yield displacement of the shear dampers is fixed at 0.014 meters, which was determined from numerical simulation of a steel plate damper. Assuming that the shear capacity is adjusted by adding or removing identical individual damper plates, the yield displacement is the same even though the shear capacity can be different.

Figure 3.13 shows the energy demand on different structural components (excluding the shear dampers) of the frame with different damper shear capacities. It is seen that larger damper shear capacities reduce energy demand on the structural components. But the effect is significant only for shear capacity under about 1500 kN. Above this level the shear capacity has very little effect on the energy demands. This behavior is similar to that of frame UPLIFT2. The difference between UPLIFT3 and UPLIFT2 lies in the amounts of plastic
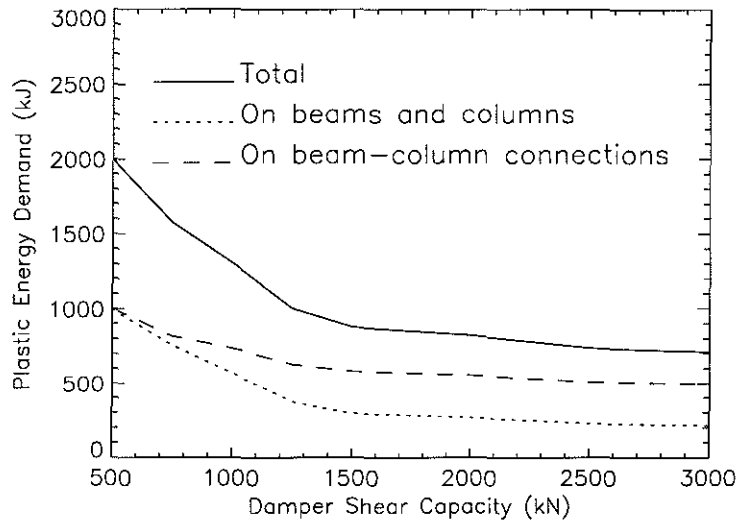
**Figure 3.13**: Plastic energy demand on frame UPLIFT3 with different damper shear capacities under B-1 ground motion scaled to 1.0 g peak acceleration.

energy demand, as is seen by comparing Figure 3.13 and Figure 3.6 on page 66. Since the shear dampers cause large axial force and moment in the columns that separate the VLC bays and the X-braced bay, the energy demand on the frame with shear dampers is greater than that on the frame with tie-down tendons.

Other responses quantities are plotted versus the damper shear capacity in Figure 3.14 to Figure 3.18. Except for a few instances, they are similar to their counterparts with the prestressed steel tie-down tendons discussed in the previous section. One such exception is the peak first-story column axial force in the X-braced bay. The peak tensile column axial forces in the X-braced bay are much smaller than those with tie-down tendons. Also, the peak compressive axial forces are larger, and the relation with the damper shear capacity is less monotonic, probably because of the impact between the columns and the supporting surface. It should be noted that the column uplift shown in Figure 3.18 for frame UPLIFT3 is the *peak* value, while that for frame UPLIFT2 shown in Figure 3.12 is the *cumulative* value.
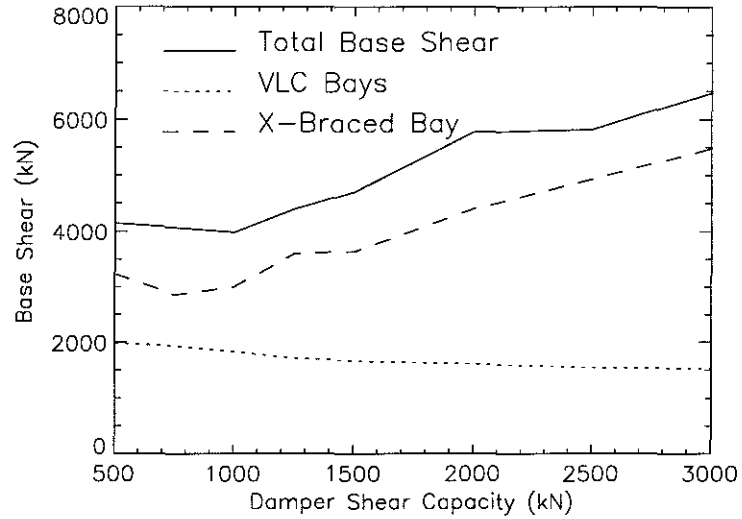
**Figure 3.14**: Peak base shears for UPLIFT3 with different damper shear capacities under B-1 ground motion scaled to 1.0 g peak acceleration.
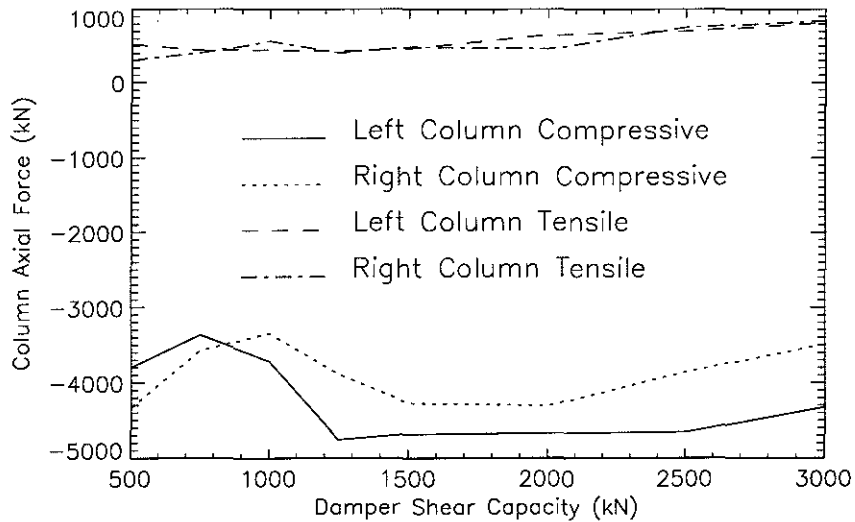


**Figure 3.15**: Peak first-story X-braced bay column axial forces for frame UPLIFT3 with different damper shear capacities under B-1 ground motion scaled to 1.0 g peak acceleration.
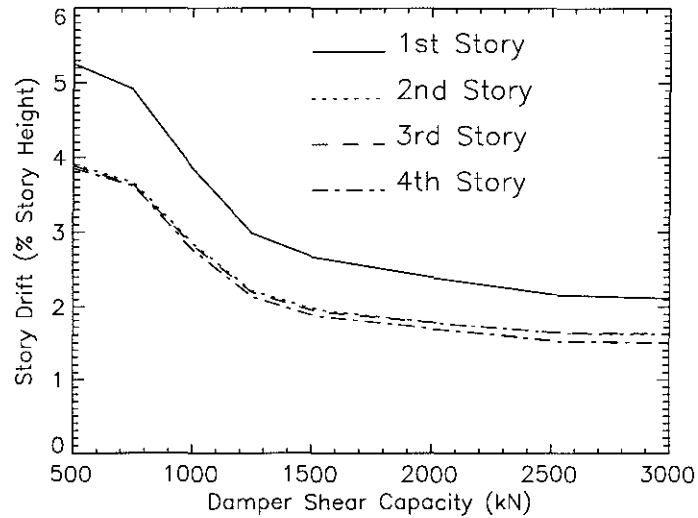
**Figure 3.16**: Peak story drifts of the VLC bays in frame UPLIFT3 with different damper shear capacities under B-1 ground motion scaled to 1.0 g peak acceleration.
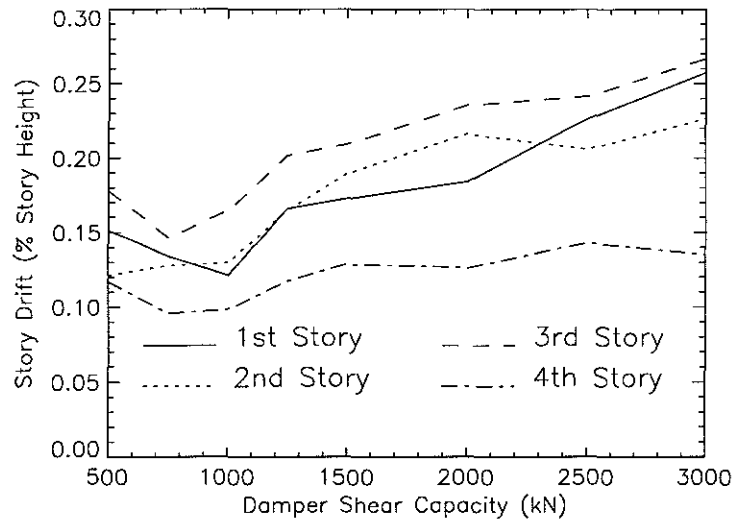


**Figure 3.17**: Peak net story drifts of the X-braced bay in frame UPLIFT3 with different damper shear capacities under B-1 ground motion scaled to 1.0 g peak acceleration.
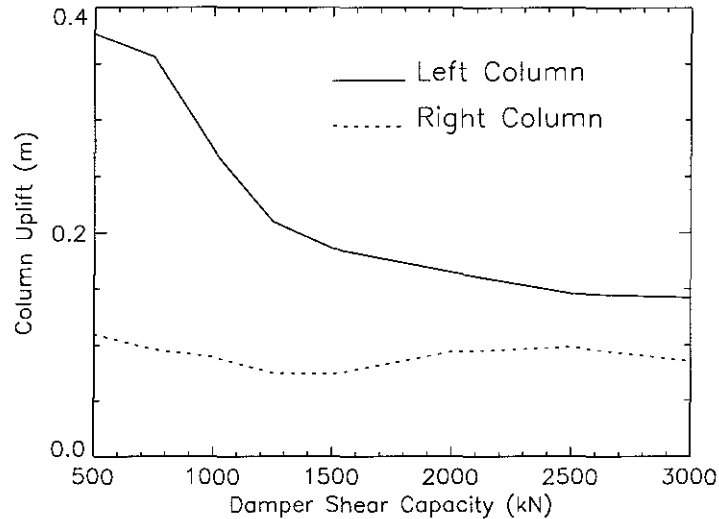
**Figure 3.18**: Peak column uplift for frame UPLIFT3 with different damper shear capacities under B-1 ground motion scaled to 1.0 g peak acceleration.

### 3.3.3  Summary

In this section the effect of the X-braced-bay uplift restraint has been studied. The results show that increasing the restraint capacity usually reduces the responses of the VLC bays, but this is efficient only for restraint capacity under a certain level. As is expected, increasing the uplift restrain capacity increases the lateral force resistance as well as the member forces and deformations in the X-braced bay. One beneficial effect of allowing column uplift is the reduction in the forces in the X-braced bay. But the magnitude of column uplift can be very significant even under the maximum amount of uplift restraint considered here. This is especially true for the frame with up-only column support for which the uplift is accumulative.

## 3.4   Responses Under Various Ground Motions

The responses of the four frames (FIXED, UPLIFT1, UPLIFT2 and UPLIFT3) under various ground motions are considered in this section. The ground motions to which these

frames are subjected include a scaled artificial ground motion acceleration time history [32] and two ground motion records, one from the 1994 Northridge earthquake and the other from the 1995 Hyogo-Ken Nanbu (Kobe), Japan earthquake.

## 3.4.1   Ground Motions of Different Amplitudes

Frames FIXED and UPLIFT2 (with 2500 kN tie-down tendon capacity for each uplifting column) were subjected to a set of ground motions with peak accelerations ranging from 0.1 g to 1.0 g. This set of ground motions was derived from the artificial ground acceleration time history B-1 [32] through amplitude scaling. No temporal scaling was performed, so the frequency content of these ground motions is identical. The focus of this part of the study is the behavior of the two frames under ground motions of different intensities.

Figure 3.19 shows the cumulative column uplifts of UPLIFT2 under the ground motions. It is seen that uplift occurs at a quite low level of ground motion (about 0.2 g), but the amount of cumulative uplift is significant only for ground motions with scaled peak acceleration above 0.4 g.
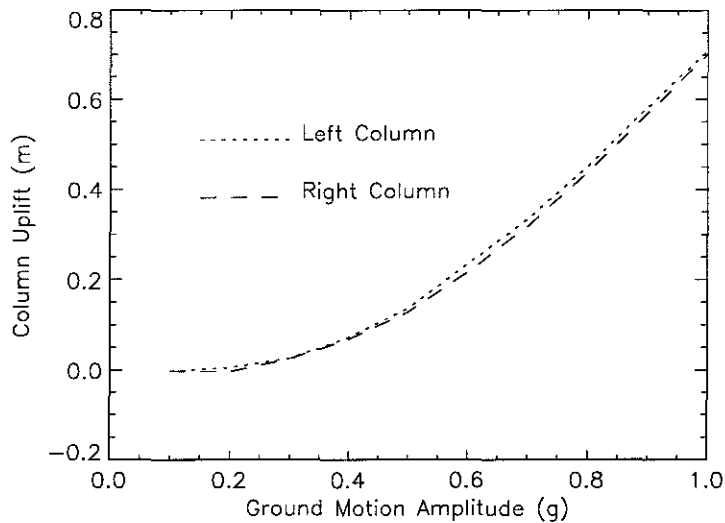


**Figure 3.19**: Cumulative column uplifts in the X-braced bay of UPLIFT2 with 2500 kN tendon capacity under ground motion B-1 scaled to different amplitudes.

Figure 3.20 illustrates the relation between the peak base shear in UPLIFT2 and the ground motion amplitude. The portions of the base shear carried by braces and by columns are plotted against the ground motion amplitude. Both increase with the ground motion amplitude. Because of uplift, the rate of increase for the base shear carried by the braces becomes lower for scaled ground motions with an amplitude greater than 0.2 g. The effect of uplift on the rate of increase for the base shear carried by the columns is not significant.
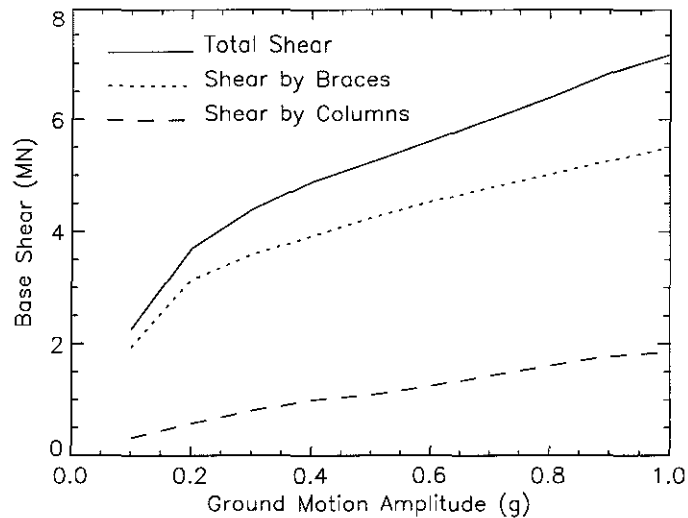


**Figure 3.20**: Peak base shears in frame UPLIFT2 with 2500 kN tendon capacity under ground motion B-1 scaled to different amplitudes.

The slenderness ratios of the braces in the X-braced bay are in the range of plastic buckling, and hence plastic deformation always accompanies brace buckling. None of the braces in frame UPLIFT2 buckle or yield in the range of amplitudes considered and they do not dissipate any energy as seen from the plots of energy dissipation in Figure 3.21. In contrast, braces in frame FIXED buckle and yield for scaled ground motions with an amplitude greater than 0.5 g, and the energy dissipation versus amplitude plots Figure 3.22 show a rapid increase in the plastic energy demand on the braces as the amplitude increases. The energy demands on beams, columns and beam-to-column connections for frame FIXED are higher than those for frame UPLIFT2.

Similar comparison applies to the peak base shear, as can be seen by comparing Fig-
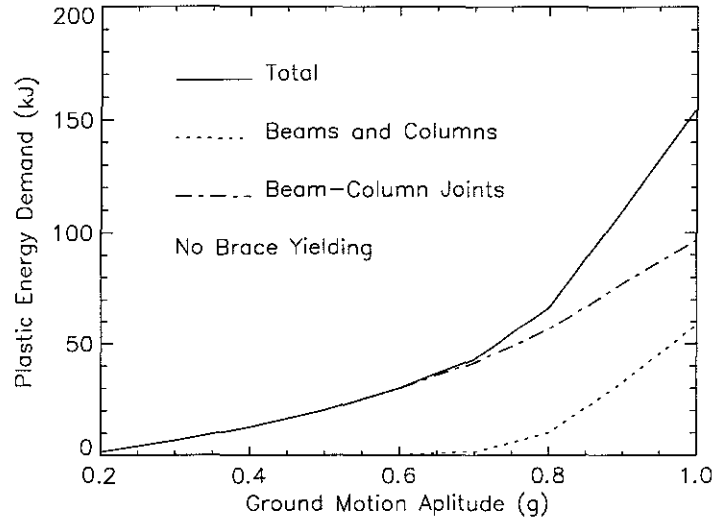
**Figure 3.21**: Plastic energy demand on structural components of frame UPLIFT2 with 2500 kN tie-down tendon capacity under ground motion B-1 scaled to different amplitudes.
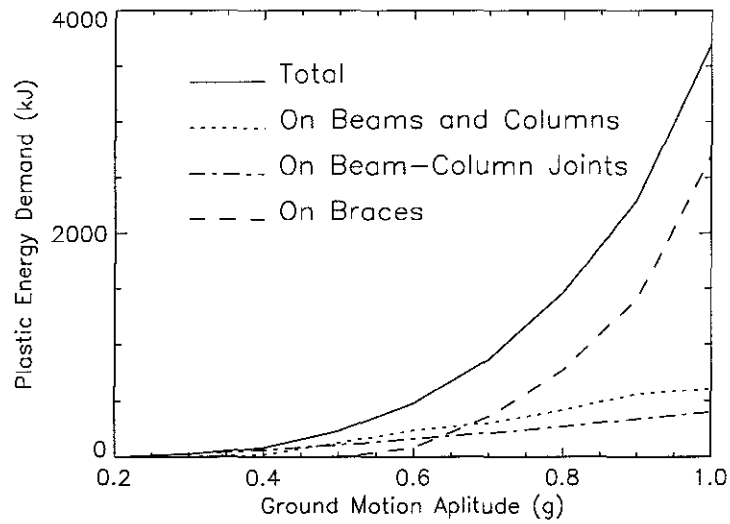


**Figure 3.22**: Plastic energy demand on structural components of frame FIXED under ground motion B-1 scaled to different amplitudes.

ure 3.20 and Figure 3.23. It is of interest to note that, after the braces in frame FIXED buckle, the shear in the columns increases more rapidly with the ground motion amplitude, apparently as a result of shear redistribution since the base shear carried by the braces effectively remains constant under scaled ground motions with an amplitude greater than 0.5 g.
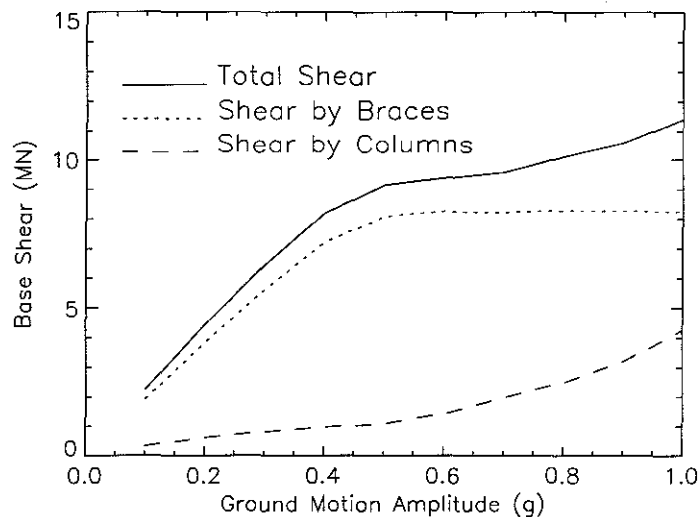


**Figure 3.23**: Peak base shears in frame FIXED under ground motion B-1 scaled to different amplitudes.

Shown in Figures 3.24 and 3.25 are the peak axial forces in the first-story columns in frames UPLIFT2 and FIXED, respectively. It is seen that uplift reduces the the axial forces in the columns in the X-braced bay. The axial forces change little for ground motions with scaled amplitudes from 0.2 to 1.0 g. The buckling of the braces in frame FIXED also limits the magnitude of the axial forces in columns connected to the braces, but these forces are much higher than those in frame UPLIFT2.

## 3.4.2 Equal-Intensity Scaled Artificial Ground Motions

Frames FIXED, UPLIFT1, UPLIFT2 and UPLIFT3 were subjected to ground motions that were derived from artificial acceleration time history B-1 through temporal and amplitude scaling as described in Appendix B on page 151. The scaling was applied to obtain ground motions with a wide range of frequency content and approximately the same intensity. A
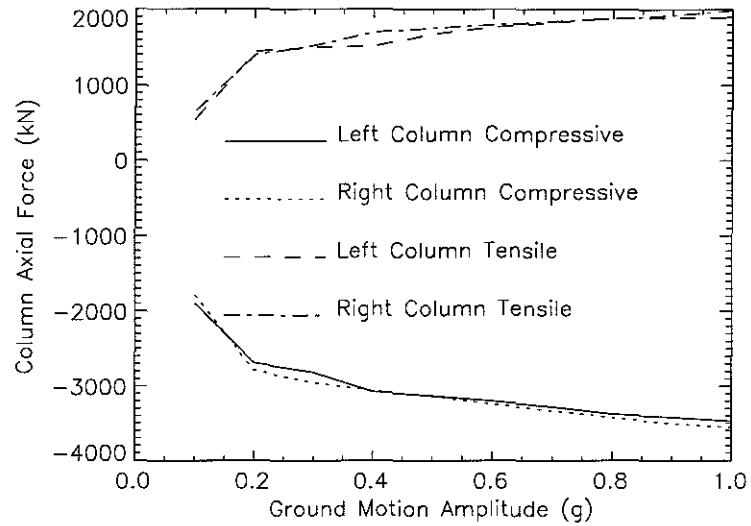
**Figure 3.24**: Peak first-floor X-braced bay column axial forces in frame UPLIFT2 with 2500 kN tie-down tendon capacity under ground motion B-1 scaled to different amplitudes.
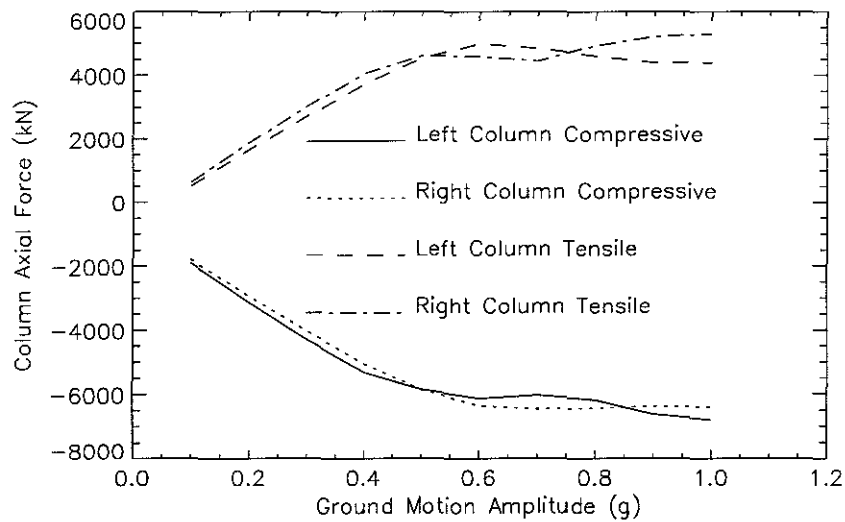


**Figure 3.25**: Peak first-floor X-braced-bay column axial forces in frame FIXED under ground motion B-1 scaled to different amplitudes.

tie-down tendon capacity of 1500 kN for frame UPLIFT2 and the same amount of damper shear capacity for UPLIFT3 are used in this section.

Shown in Figure 3.26 are the plastic energy demands on different structural components in the four frames under the equal-intensity scaling. The energy dissipated by the tie-down tendons in UPLIFT2 and by the shear dampers in UPLIFT3 are not included in the plots. From the figure it is seen that the energy demands on different components in UPLIFT2 are the lowest among the four frames and are quite insensitive to the frequency content of the ground motion input. The energy demands on the beams, columns and beam-to-column connections for frame UPLIFT1 are high because its uplifting bay provides little horizontal resistance. Frame UPLIFT3 has a high energy demand on its beam-to-column connections, probably due to the extra moment and axial force caused by the shear dampers. The braces in frame FIXED buckled and they did so over a large range of the scaling, resulting in large energy demand on both the braces and other structural components.

Figure 3.27 shows the peak total base shear and the peak base shears carried by the VLC bays and the X-braced bay, respectively, of the four frames. In all frames, the VLC bays carry only a small portion of the total base shear, while the majority is carried by the X-braced bay. For the range of scaling considered, the total base shear in frame FIXED is about twice as large as those in the other three frames with an uplifting bay.

Plotted in Figure 3.28 are the peak story drifts of the VLC bays of the four frames. As is expected, the frame without uplift restraint (UPLIFT1) has the largest story drifts among the four because of its low lateral resistance. Frame FIXED has the smallest story drifts except in its first story where the X-braces buckled for some of the scaling factors. Because the buckled braces reduce the shear force delivered to the upper stories, these stories experienced relatively small story drifts. Frame UPLIFT2 has lower story drifts than does frame FIXED in the stories where the latter's X-braces buckled and has higher story drifts in the stories where these X-braces did not buckle.

Figure 3.29 compares the peak axial forces in the first-story X-braced-bay columns in the four frames. It is seen that frame FIXED always has the largest compressive as well as

81
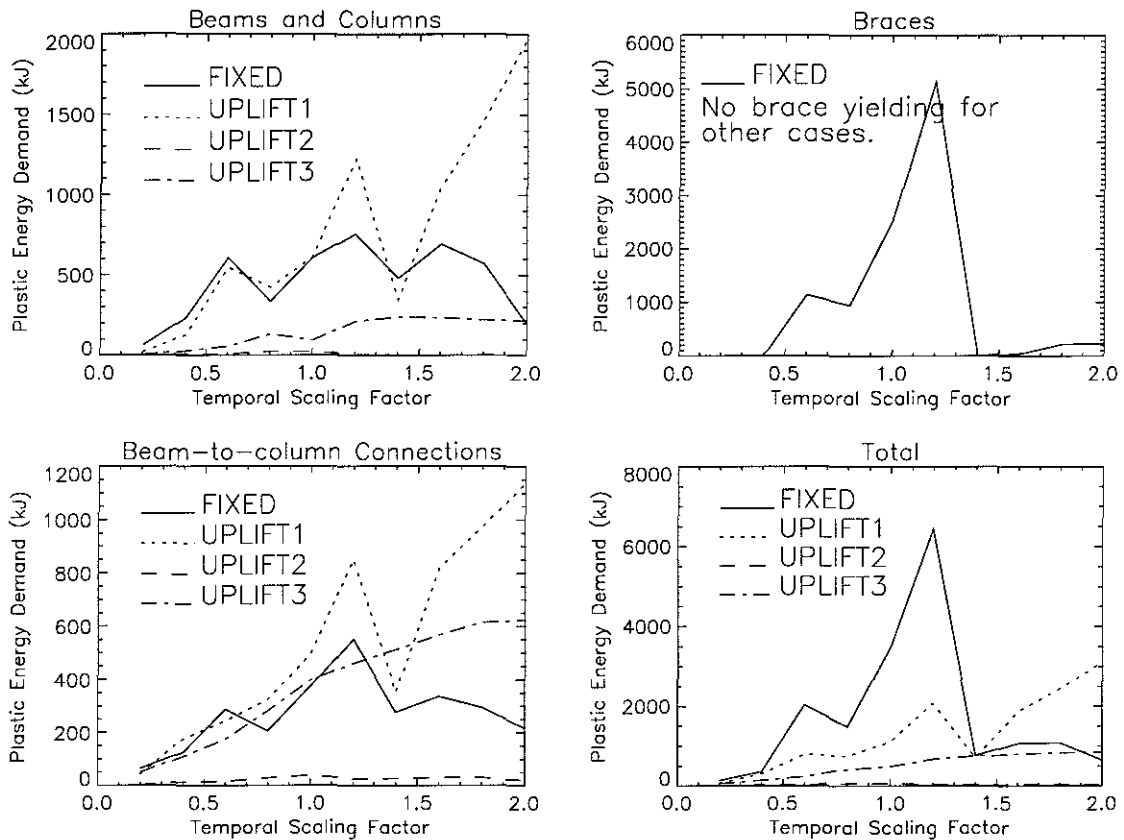


**Figure 3.26**: Comparison of plastic energy demand on structural components of frames with different X-braced-bay column base conditions under ground motion B-1 with equal-intensity scaling.

the largest tensile column axial forces, while frame UPLIFT2 has the smallest compressive column axial forces. The peak compressive column axial forces for UPLIFT1 and UPLIFT3 lie in between. Tensile column axial forces for all three frames with an uplifting bay are much lower than that for frame FIXED. Large column axial force increases the risk of failure in the columns themselves as well as their connections.

It is of interest to note that the peak column axial forces for frame UPLIFT2 are very insensitive to the scaling, which means that they are not very sensitive to the frequency contents of the ground motion. The advantage of this characteristic is that it reduces the uncertainty of the earthquake forces associated with the frequency contents of the ground motion and makes a more accurate estimation of the column force possible.
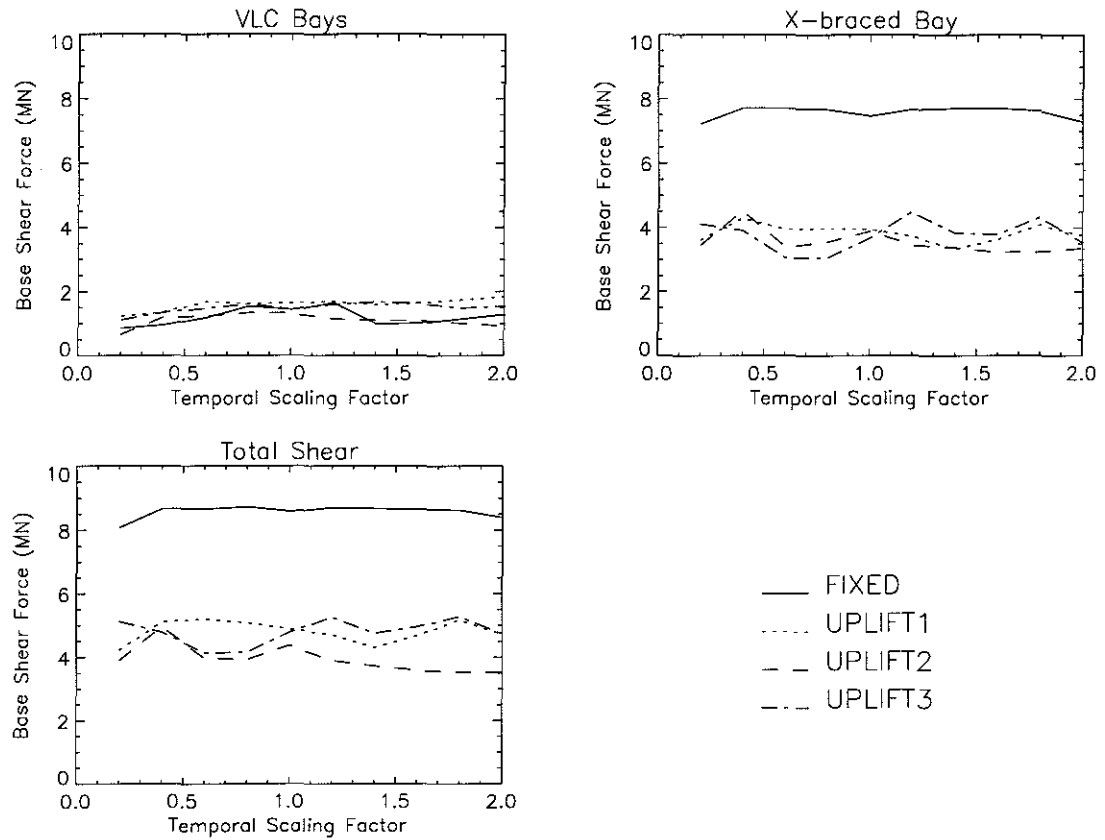
**Figure 3.27**: Comparison of peak base shear in frames with different X-braced-bay column base conditions under ground motion B-1 with equal-intensity scaling.

## 3.4.3 Earthquake Ground Motion Records

Recent seismic events in the United States and Japan have generated some of strongest ground motions in terms of peak velocity and acceleration that have ever been recorded. These records provide particularly valuable data to the study of the response of structures to strong earthquakes. In this section frames FIXED, UPLIFT2 and UPLIFT3 (the later two with an uplift restraint of 1500 kN for each column of the X-braced bay) are subjected to three earthquake ground motion records with peak acceleration ranging from 0.36 g to 0.84 g. These records include one from the 1995 Kobe earthquake (JMA), one from the 1994 Northridge earthquake (Sylmar), and the other from the 1985 Central Chile Earthquake (Vina del Mar). Details on these records can be found in Appendix B on page 151.
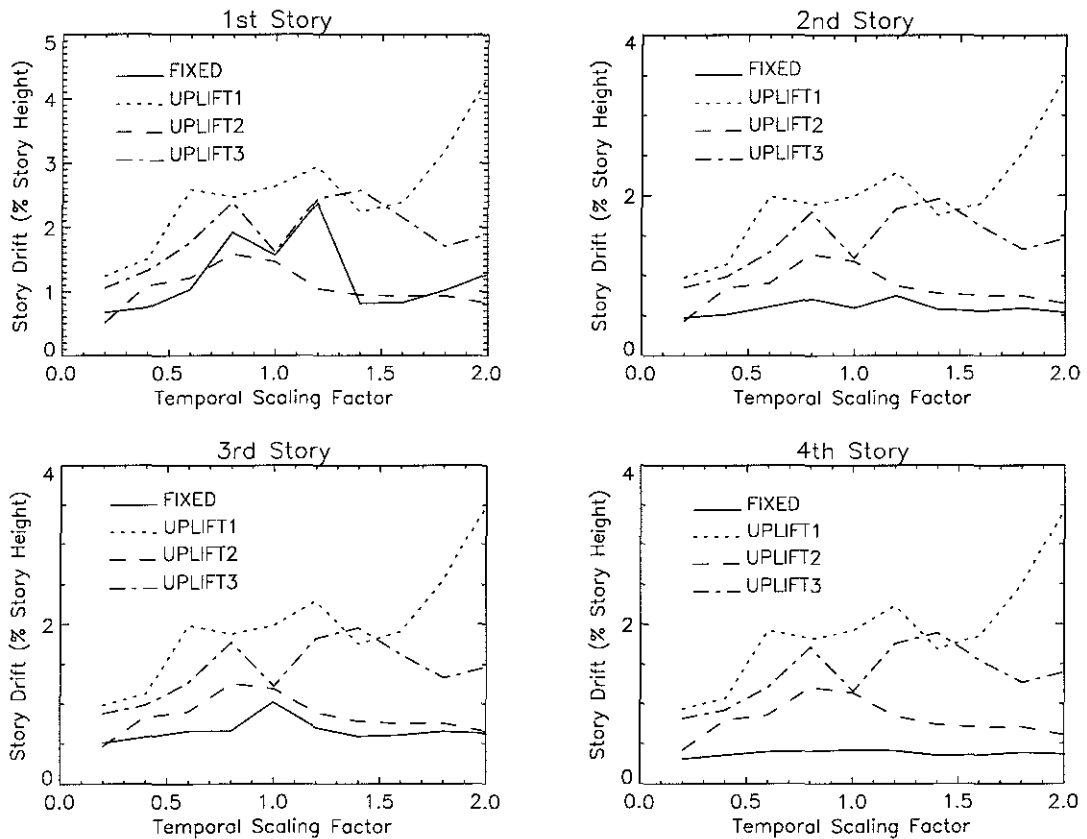
**Figure 3.28**: Comparison of peak story drift of VLC bays in frames with different X-braced-bay column base conditions under ground motion B-1 with equal-intensity scaling.

The response quantities of the three frames are listed in Tables 3.2 to 3.4.

Table 3.2 summarizes the responses of the frames under the Kobe ground motion record. The first 4 rows show the story drifts in the VLC bays. The story drifts in FIXED are much smaller than those in the other two frames, except for the first story where the braces in FIXED buckled. The large story drifts in UPLIFT2 and UPLIFT3 are the price paid in exchange for smaller X-braced-bay member forces, as shown in rows 13 to 16. Because of the smaller member forces, the deformational story drifts (rows 5 to 8) in the X-braced bay of UPLIFT2 and UPLIFT3 are small.

The plastic energy demands on different structural components are listed in rows 9 to 12. For UPLIFT2 and UPLIFT3 the energy dissipated by the uplift restraint, which dominates the energy dissipation as do the braces in FIXED, is not included in the table. Comparing the

| No. | Response Quantities | | | Frames | | |
|-----|-----|-----|-----|-----|-----|-----|
| | | | | FIXED | UPLIFT2 | UPLIFT3 |
| 1 | Story Drifts (% Story Height) | VLC Bay | 1st Story | 2.72 | 2.83 | 2.97 |
| 2 | | | 2nd Story | 0.86 | 2.40 | 2.25 |
| 3 | | | 3rd Story | 0.63 | 2.40 | 2.24 |
| 4 | | | 4th Story | 0.40 | 2.36 | 2.19 |
| 5 | | X-Braced Bay[1] | 1st Story | 2.38 | 0.18 | 0.29 |
| 6 | | | 2nd Story | 0.80 | 0.13 | 0.28 |
| 7 | | | 3rd Story | 0.57 | 0.16 | 0.35 |
| 8 | | | 4th Story | 0.34 | 0.11 | 0.17 |
| 9 | Plastic Energy (kJ) | Beams and Columns | | 349 | 156 | 420 |
| 10 | | Braces | | 1403 | 0 | 0 |
| 11 | | Beam-to-Column Joints | | 169 | 94 | 418 |
| 12 | | Total | | 1921 | 250 | 838 |
| 13 | Axial Forces (kN) | Column Compressive[2] | | 6517 | 2682 | 7176 |
| 14 | | Column Tensile[2] | | 4658 | 1182 | 602 |
| 15 | | Brace Compressive[2] | | 4636 | 2249 | 3885 |
| 16 | | Brace Tensile[2] | | 5018 | 2171 | 3634 |
| 17 | Base Shear (kN) | | | 8866 | 4449 | 7454 |
| 18 | Left Column Uplift (m)[3] | | | 0.00 | 0.60 | 0.21 |
| 19 | Right Column Uplift (m)[3] | | | 0.00 | 0.46 | 0.14 |

**Table 3.2**: Peak responses of frames with different column-base anchoring conditions under the Kobe ground motion record. Notes: (1) For frames UPLIFT2 and UPLIFT3 these are the deformational story drifts of the uplift bay; (2) These are the peak axial forces in the first story columns of the X-braced bay; (3) Column uplifts for UPLIFT2 are cumulative values, while those for UPLIFT3 are peak values.

| No. | Response Quantities | | | Frames | | |
|---|---|---|---|---|---|---|
| | | | | FIXED | UPLIFT2 | UPLIFT3 |
| 1 | Story Drifts (% Story Height) | VLC Bay | 1st Story | 1.84 | 1.74 | 1.52 |
| 2 | | | 2nd Story | 0.70 | 1.37 | 1.16 |
| 3 | | | 3rd Story | 1.08 | 1.37 | 1.15 |
| 4 | | | 4th Story | 0.41 | 1.31 | 1.09 |
| 5 | | X-Braced Bay[1] | 1st Story | 1.51 | 0.14 | 0.13 |
| 6 | | | 2nd Story | 0.64 | 0.14 | 0.14 |
| 7 | | | 3rd Story | 1.02 | 0.15 | 0.16 |
| 8 | | | 4th Story | 0.35 | 0.09 | 0.08 |
| 9 | Plastic Energy (kJ) | Beams and Columns | | 195 | 30 | 19 |
| 10 | | Braces | | 459 | 0 | 0 |
| 11 | | Beam-to-Column Joints | | 79 | 25 | 60 |
| 12 | | Total | | 733 | 55 | 79 |
| 13 | Axial Forces (kN) | Column Compressive[2] | | 6857 | 2541 | 3057 |
| 14 | | Column Tensile[2] | | 5206 | 1210 | 354 |
| 15 | | Brace Compressive[2] | | 4626 | 2110 | 2090 |
| 16 | | Brace Tensile[2] | | 4945 | 1966 | 1982 |
| 17 | Base Shear (kN) | | | 8618 | 4237 | 4064 |
| 18 | Left Column Uplift (m)[3] | | | 0.00 | 0.14 | 0.05 |
| 19 | Right Column Uplift (m)[3] | | | 0.00 | 0.18 | 0.11 |

**Table 3.3**: Peak responses of frames with different column base anchoring conditions to the Sylmar ground motion record. Notes: (1) For frames UPLIFT2 and UPLIFT3 these are the deformational story drifts of the uplift bay; (2) These are the peak axial forces in the first story columns of the X-braced bay; (3) Column uplifts for UPLIFT2 are cumulative values, while those for UPLIFT3 are peak values.

| No. | Response Quantities | | | Frames | | |
|---|---|---|---|---|---|---|
| | | | | FIXED | UPLIFT2 | UPLIFT3 |
| 1 | Story Drifts (% Story Height) | VLC Bay | 1st Story | 0.37 | 0.45 | 0.97 |
| 2 | | | 2nd Story | 0.27 | 0.34 | 0.74 |
| 3 | | | 3rd Story | 0.30 | 0.36 | 0.75 |
| 4 | | | 4th Story | 0.18 | 0.31 | 0.68 |
| 5 | | X-Braced Bay[1] | 1st Story | 0.21 | 0.12 | 0.16 |
| 6 | | | 2nd Story | 0.23 | 0.12 | 0.16 |
| 7 | | | 3rd Story | 0.27 | 0.14 | 0.19 |
| 8 | | | 4th Story | 0.15 | 0.08 | 0.10 |
| 9 | Plastic Energy (kJ) | Beams and Columns | | 0 | 0 | 1 |
| 10 | | Braces | | 0 | 0 | 0 |
| 11 | | Beam-to-Column Joints | | 18 | 0 | 40 |
| 12 | | Total | | 18 | 0 | 41 |
| 13 | Axial Forces (kN) | Column Compressive[2] | | 3564 | 2309 | 3418 |
| 14 | | Column Tensile[2] | | 2289 | 891 | 352 |
| 15 | | Brace Compressive[2] | | 2612 | 1569 | 2152 |
| 16 | | Brace Tensile[2] | | 2708 | 1522 | 2002 |
| 17 | Base Shear (kN) | | | 4907 | 2971 | 4249 |
| 18 | Left Column Uplift (m)[3] | | | 0.00 | 0.11 | 0.06 |
| 19 | Right Column Uplift (m)[3] | | | 0.00 | 0.14 | 0.06 |

**Table 3.4**: Responses of frames with different column base anchoring conditions to the Vina del Mar ground motion record. Notes: (1) For frames UPLIFT2 and UPLIFT3 these are the deformational story drifts of the uplift bay; (2) These are the peak axial forces in the first story columns of the X-braced bay; (3) Column uplifts for UPLIFT2 are cumulative values, while those for UPLIFT3 are peak values.

87
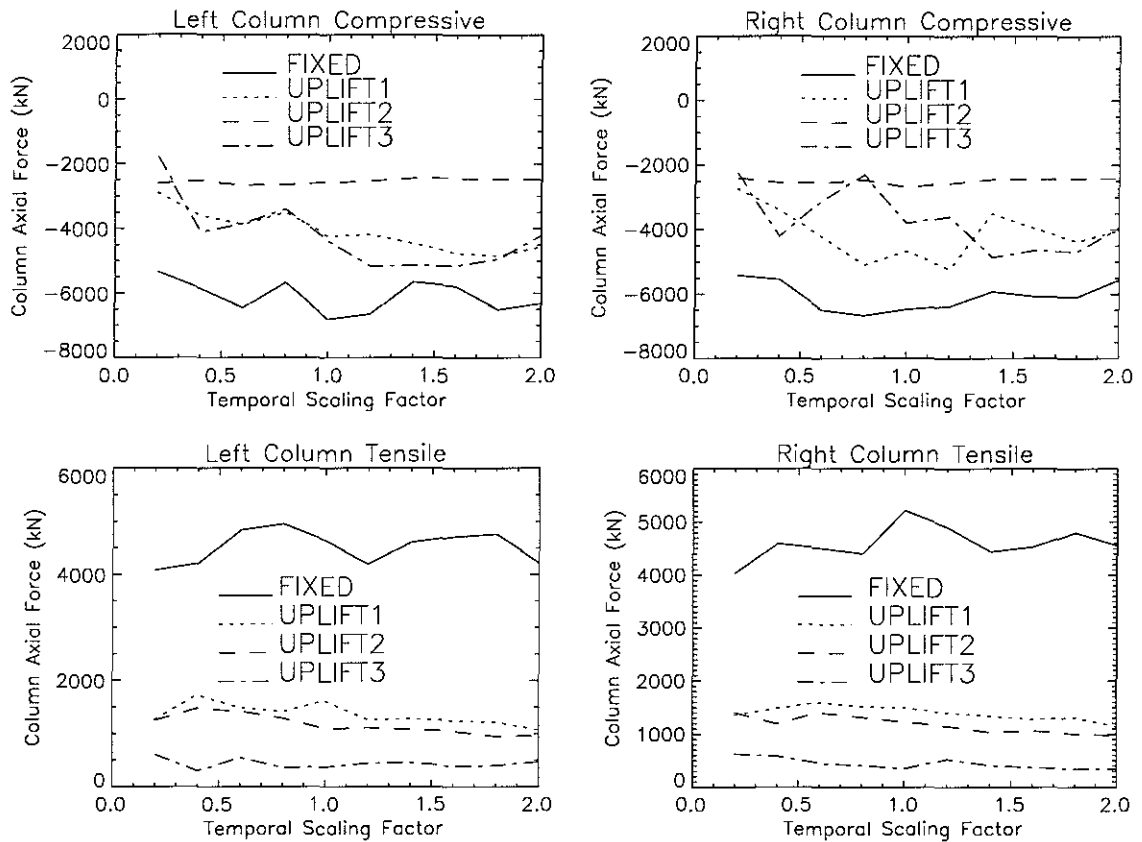


**Figure 3.29**: Comparison of peak axial forces in the first-story columns for frames with different X-braced bay column base conditions under ground motion B-1 with equal-intensity scaling.

plastic energy demands on beams and columns and on beam-to-column connections shows that frame UPLIFT2 has the smallest energy demands. As expected, there is a high plastic energy demand on the components of frame FIXED as a result of the brace buckling. But the energy demands on the beams and columns and on the beam-to-column connections of frame UPLIFT3 are also very high. A closer look at the plastic energy demand on the individual members in frame UPLIFT3 reveals that plastic deformation occured mainly in beams and beam-to-column connections adjacent to the uplifting bay. This is probably the result of the extra force and moment resulting from the shear dampers.

The uplift restraint in frame UPLIFT2 is able to reduce the total base shear (row 17) and the member forces in X-braced-bay columns and braces (rows 13 to 16). As a result, the braces in frame UPLIFT2 (also true for UPLIFT3) did not yield under the ground motion.

However, the columns experience substantial uplift (row 18 and 19) and this may not be acceptable in practice. Frame FIXED has high axial forces in the X-braced-bay columns and braces. This is consistent with the column and baseplate failures observed in the Northridge and Kobe earthquakes.
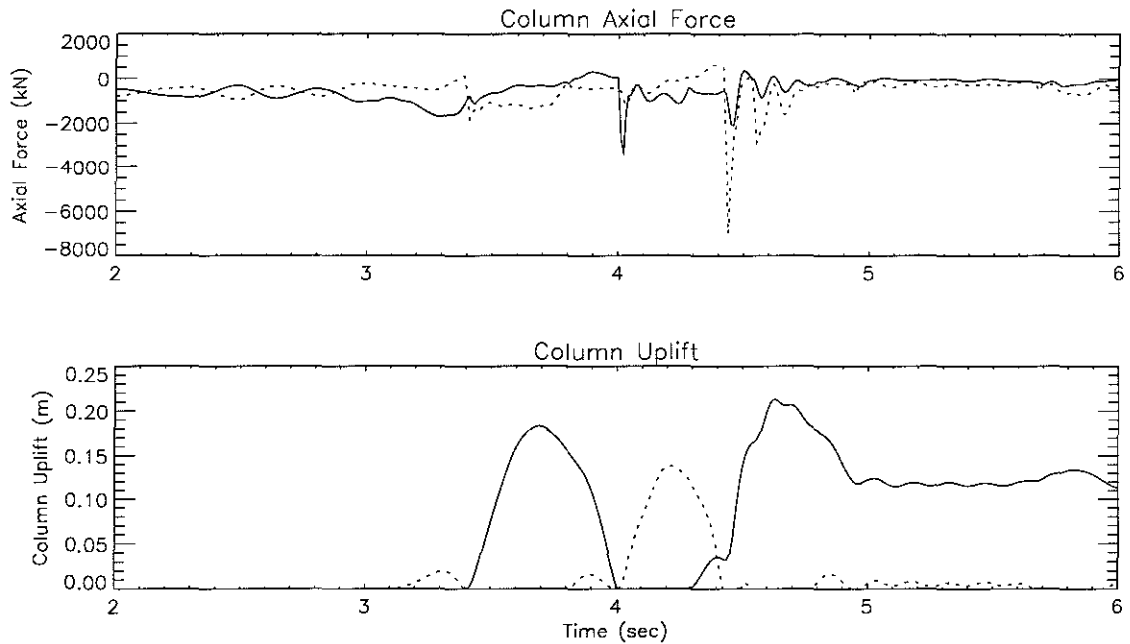


**Figure 3.30**: Axial force and uplift time histories for the first-story uplifting columns in frame UPLIFT3. Solid line—left column; dotted line—right column. Impact occurs when the uplifted column comes down. The impact causes a sudden increase in the axial force of the column.

Frame UPLIFT3 also has high compressive axial forces in the X-braced-bay columns, apparently resulting from the impact that occurs when an uplifted column comes back down. Figure 3.30 shows part of the time history for the axial force in the first-story X-braced-bay columns along with the uplift displacement time histories. It is seen that the moments when the columns impact with its supporting surface are accompanied by spikes in the column axial force time history, e.g., at $t = 4.0$ and 4.4 seconds. No impacts occur in frame UPLIFT2, as evidenced by plots in Figure 3.31.

The responses of the frames under the Sylmar ground motion (Table 3.3) are generally not as severe as, but in most aspects similar to, those under the Kobe ground motion. One
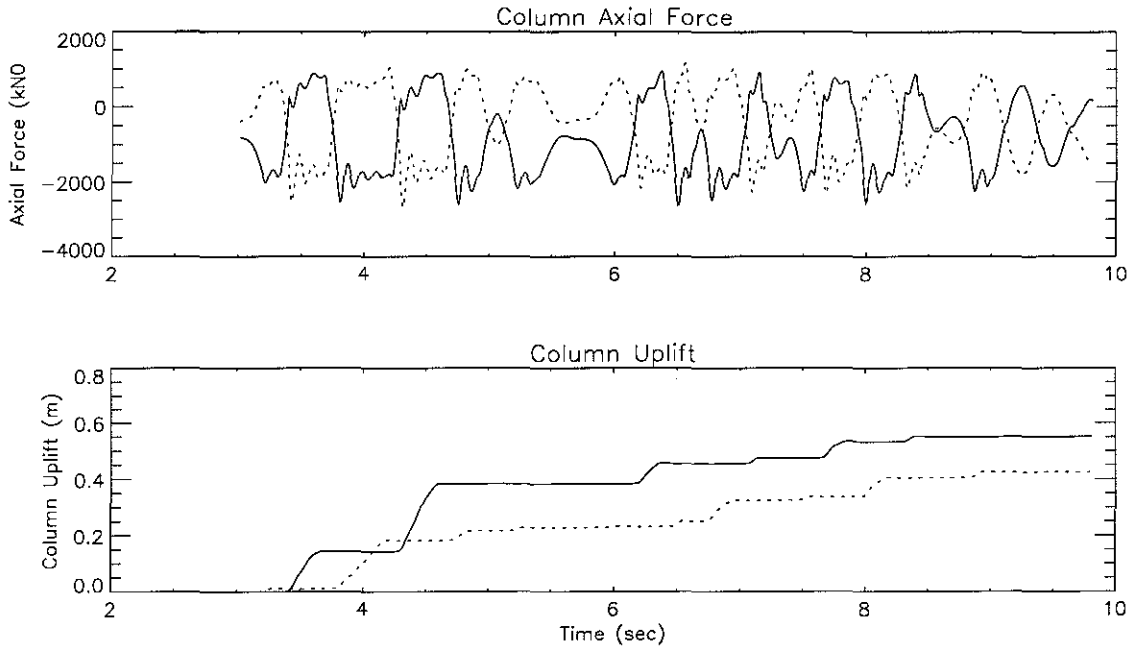
**Figure 3.31**: Axial force and uplift time histories for the first-story uplifting columns in frame UPLIFT2. Solid lines—left column; dotted lines—right column. There is no impact.

difference is that the braces in FIXED buckled on the third floor as well as on the first floor for the Sylmar ground motion. Responses under Vina del Mar ground motion, as shown in Table 3.4, are the least severe among the three ground motion histories. None of the braces buckled and the plastic energy demands on all structural components are minimal.

The push-over result in Figure 3.4 on page 63 shows that the virgin strength of FIXED is much higher than that required by the Uniform Building Code. Nevertheless, the frame suffers very severe deformation when subjected to the Sylmar and Kobe ground motions. This raises question about the propriety of using the initial buckling strength of the braces as a reference strength in seismic design. A more reasonable approach may be to base the design strength on the post buckling capacity of the braces.

## 3.4.4 Summary

Comparing the responses of the four frames with different column base anchoring conditions in the X-braced bay shows that tendon uplift restraint with up-only support can signi-

ficantly reduce the member force, base shear and the energy demands on beams, columns and braces, but it can also introduce large story drift and column uplift. Pounding resulting from column uplift for a stationary support can cause a significant increase in the column axial force. Completely anchored X-braced-bay columns result in large axial forces in columns and braces, and can cause brace buckling and large story drift in braced frames much stronger than code requirement.

## 3.5  Conclusions

The earthquake response characteristics of steel frames with different X-braced-bay column anchoring conditions have been the subject of this chapter. The results show that it is difficult to design a well behaved X-braced frame whose lateral resistance is provided by small number of heavy X-braced bays. Completely anchored X-braced bays can induce large member force in the X-braced bays, making the columns, braces and their connections vulnerable to cracking as was observed in recent earthquakes. It is possible for a braced frame with fixed column bases to suffer severe deformation under ground motions similar to those recorded in the Northridge and Kobe earthquakes even though the virgin strength of the frame is much higher than the code requirement. Flexible X-braced-bay column anchoring can significantly reduce the braced-bay member forces, but at the same time can also introduce large story drift and column uplift. The pounding of an uplifting column on its support also increases its axial force.

# Chapter 4

# Frames With Different Bracing Systems

## 4.1  General

It was shown in Chapter 2 that slender braces are more susceptible to deterioration than stocky ones. But on the other hand, experience from past earthquakes and results from Chapter 3 show that using strong braces can result in large braced-bay member force and increase the risk of failures in the braced-bay members and their connections. Since buckling is the cause for brace deterioration, in an attempt to solve this dilemma, a non-buckling bracing system is proposed in this chapter. Once buckling ceases to be a problem, a bracing system consisting of small but widely distributed bracing members can be used in place of one consisting of small number of large braces. This chapter focuses on the comparison study of the effectiveness of different bracing systems, including the above non-buckling bracing system and several conventional bracing systems with different configurations and brace end conditions.

## 4.2  The Structures

### 4.2.1  General Configuration

The studies were conducted in the context of several six-story, 2-bay by 2-bay steel frame structures, each of which has a different bracing system. All these structures have been derived from a six-story test structure designed for the U.S.-Japan Cooperative Earthquake Research Program Utilizing Large Scale Test Facilities [6] by varying the bracing system.

The original test structure represents a portion of a typical office building. It consists of three frames in the longitudinal (testing) direction, three frames in the transverse direction, and a composite floor system, as shown in Figure 4.1. In the longitudinal direction, the two exterior frames, designated as Frame A and Frame C, are of ductile moment-resisting type. The central longitudinal frame, designated as Frame B, is braced in the 1-2 bay with a concentric chevron bracing system. The two exterior frames in the transverse direction are diagonally X-braced to increase the torsional stiffness of the structure. The composite floor system is comprised of steel decking with headed studs as shear connectors and steel-wire-mesh-reinforced cast-in-place lightweight concrete. In accordance with the purpose of the original testing, only the response in the longitudinal direction is considered.

The structures considered in this chapter have the same column spacing and story height as the original test structure shown in Figure 4.1, but have different bracing systems. For structures with conventional braces, two bracing configurations are considered: chevron bracing and X-bracing, as shown in Figure 4.1(b) and Figure 4.2(a), respectively. For each configuration, both pinned-pinned and clamped-clamped brace end conditions are considered. In the pinned-pinned end condition, a bracing member can rotate freely at both ends; in the clamped end condition, the ends of a brace are assumed to rotate with the joints to which they are attached.

The previous chapter and past earthquake damage [12] show that slender braces are more susceptible to deterioration under cyclic displacement. To improve the resistance to deterioration, stockier braces (meaning fewer braced bays) can be used. But there is evidence that this can also be problematic. Firstly, there were instances [1, 12] during the Northridge and Kobe earthquakes in which braced-bay columns and baseplates suffered severe damage. Since braced bays often have very high lateral stiffness compared with unbraced bays, a small number of heavily-braced bays in a large structure can produce excessive forces in the braced bay members. A small number of braced bays also reduces the redundancy of the structure. Secondly, as seen from the previous study, stocky braces also have higher fiber strain than slender braces once buckling occurs under the same axial displacement. The

93
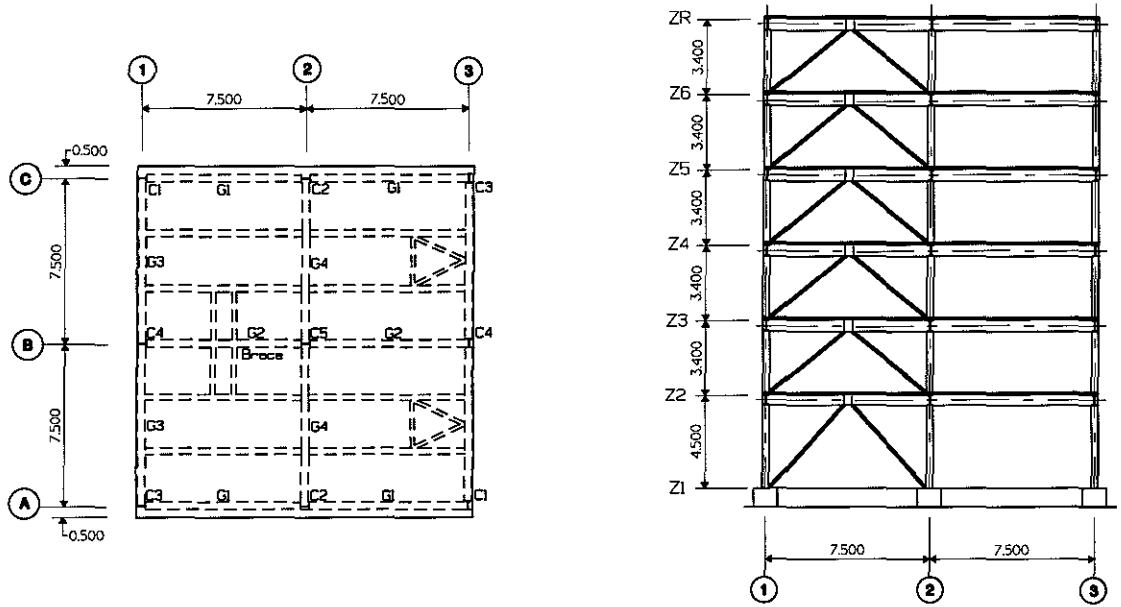


(a) Typical Floor Plan

(b) Elevation Frame B
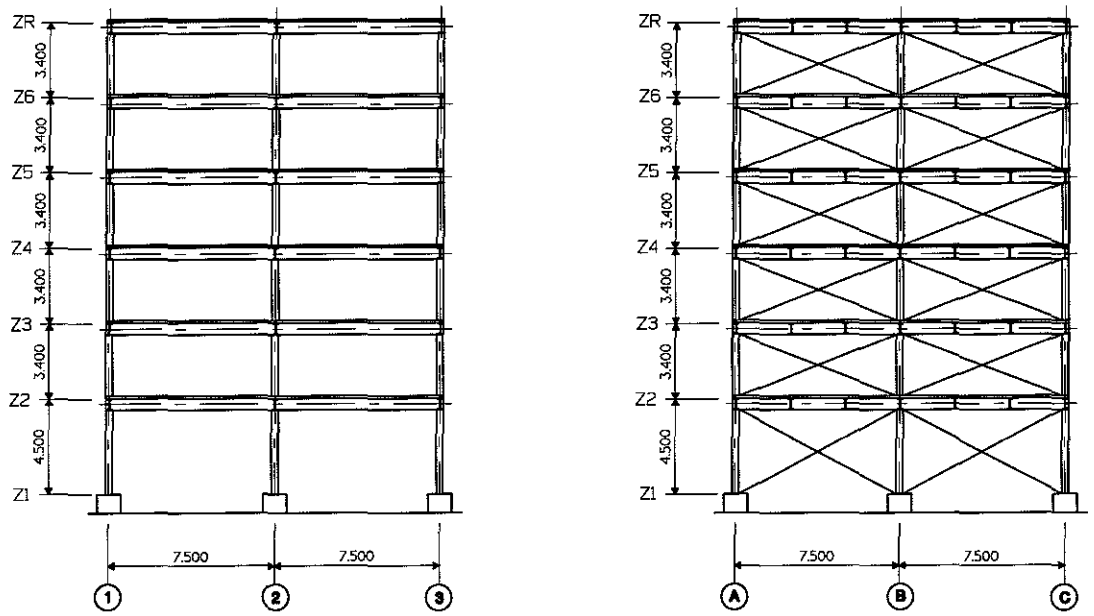
(c) Elevation Frame A, C

(d) Elevation Frame 1, 3

**Figure 4.1**: Typical plan and elevations of the test structure [6].

higher fiber strain can cause local buckling which in turn can lead to rupture. Because of this, stocky braces may be more brittle than slender ones. Another disadvantage with large structural members is the greater difficulty with welding. So using stocky braces may not be the best solution.

To explore alternative bracing systems, a hypothetical non-buckling bracing system is considered in the study. The non-buckling system is composed of slip braces, and it differs from a conventional bracing system in that when a non-buckling brace is subjected to compressive force, it shortens automatically before its buckling load is reached, thus eliminating the residual tensile elongation and making it possible to take full advantage of the high tension capacity of the brace. Since the deterioration associated with buckling is not a problem for a slip brace, a large number of small slip braces can be distributed in many bays in a large structure, thus avoiding the problem of having only a few braced bays with heavy braces.

For the structure with non-buckling braces, smaller braces are used in both bays of Frame B, as shown in Figure 4.2(b). The total brace cross-sectional area in each story still equals to that of the conventional braces in Figure 4.2(a). In total five structures are considered, four with conventional braces and one with non-buckling braces. For structures with X-bracing, as shown in Figure 4.2, there are no cross connections between the cross braces in the first and sixth stories. Table 4.1 summarizes the five structures considered in this chapter.

## 4.2.2 Slip Braces

A slip brace is schematically shown in Figure 4.3. In the figure, the control unit controls the slipping and locking of the two yielding units. When the brace is under compression, the control unit allows the connection of the two yielding units to slip; when the brace is under tension, it locks them together. Although it is possible for such an assemblage to resist compressive force that is below the buckling load, this study assumes that no compressive resistance is present.

(a) With conventional braces      (b) With non-buckling braces
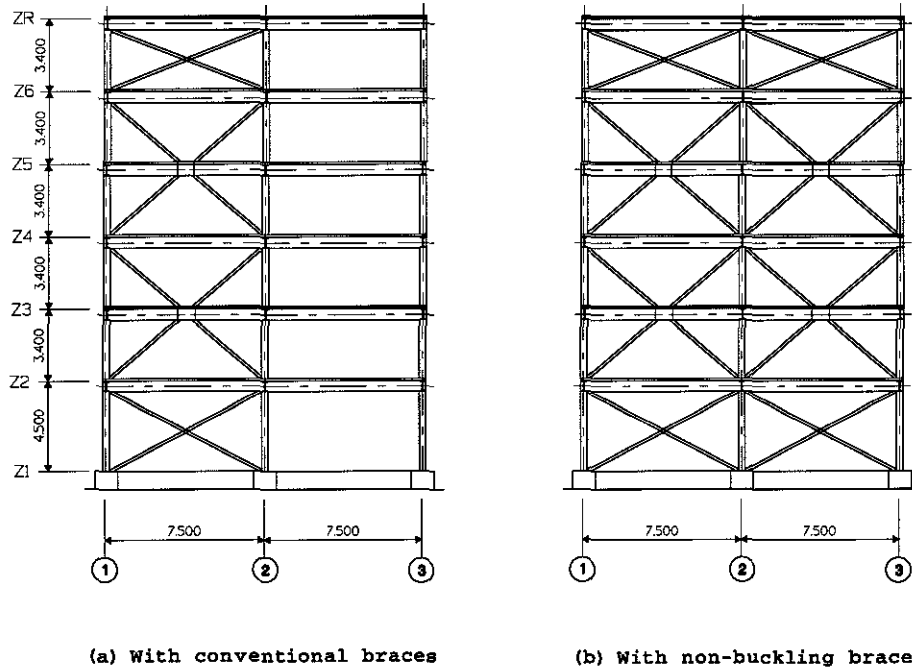
**Figure 4.2**: Two X-bracing systems in Frame B. The two have the same total brace cross-sectional area in each story.

| Structure | Bracing System |
|-----------|----------------|
| F6PV | Pin-ended Chevron braces. |
| F6CV | Clamp-ended Chevron braces. |
| F6PX | Pin-ended X-braces. |
| F6CX | Clamp-ended X-braces. |
| F6SL | Non-buckling slip braces. |

**Table 4.1**: Bracing systems of the five structures used in this study.
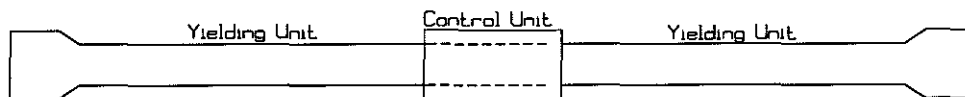


**Figure 4.3**: Schematic drawing of a slip brace.
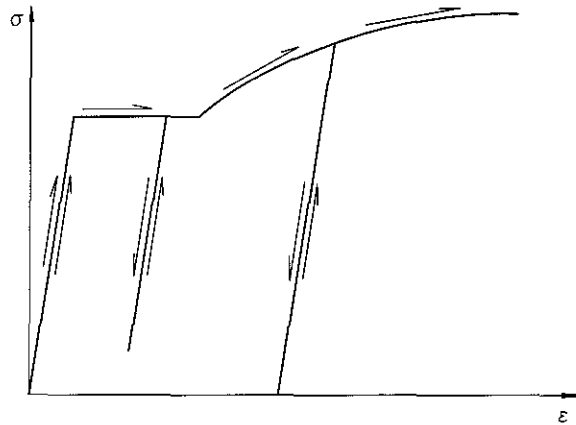
**Figure 4.4**: Typical stress-strain path in the yielding units of a slip brace.

A typical stress-strain curve for the yielding unit is shown in Fig 4.4, and examples of the hysteretic loops can be found in Figure 4.30 on page 127. Thus, energy dissipation comes entirely from plastic elongation. Since the control unit eliminates the residual elongation, the total elongation of the brace is limited by the allowable strain limit of the yielding units, not by the allowable story drift of a frame structure as in the case of conventional braces. The purpose of this chapter is to study the potential of the concept of non-buckling braces, not the implementation of such braces.

## 4.2.3  Gravity and Lateral Force Design

The original test structure was designed in accordance with the requirements of both the 1979 Uniform Building Code (UBC) and the 1981 Japanese Aseismic Design Code, with a dead load of 3.60 kN/m$^2$ (75 psf) for the roof and 4.31 kN/m$^2$ (90 psf) for the floors, and a live load of 2.88 kN/m$^2$ (60 psf) for the design of the slabs and floor beams and of 1.77 kN/m$^2$ (37 psf) for the design of the frames. The design was found to satisfy the 1985 UBC requirements for structures in Zone 4 if the effective length factor of the braces is taken as 0.7 [6]. Hassan [14] redesigned the structure according to the 1988 Uniform Building Code as a braced moment resisting structure with $R_w = 10$. This results in smaller beam and column sizes and equal or larger brace sizes except for the first story.

| Floor | G1 | G2 |
|---|---|---|
| Roof | 16W31 | 16W31 |
| 6 | 16W31 | 16W31 |
| 5 | 16W31 | 18W35 |
| 4 | 18W35 | 18W35 |
| 3 | 18W35 | 18W40 |
| 2 | 18W40 | 18W40 |

| Story | Brace |
|---|---|
| 6 | $\square 5 \times 5 \times 3/16$ |
| 5 | $\square 5 \times 5 \times 3/16$ |
| 4 | $\square 6 \times 6 \times 3/16$ |
| 3 | $\square 6 \times 6 \times 1/4$ |
| 2 | $\square 7 \times 7 \times 1/4$ |
| 1 | $\square 7 \times 7 \times 1/4$ |

(a) Girders                     (b) Conventional Braces

| Story | C1 | C2 | C3 | C4 | C5 |
|---|---|---|---|---|---|
| 6-5 | 10W33 | 10W33 | 10W49 | 10W33 | 12W40 |
| 4-3 | 10W39 | 12W53 | 10W65 | 10W60 | 12W72 |
| 2 | 12W50 | 12W65 | 12W79 | 12W79 | 12W106 |
| 1 | 12W65 | 12W87 | 12W87 | 12W106 | 12W136 |

(c) Columns

Table 4.2: Member sizes for the six-story frame structures (longitudinal frames).

The plan here was to study the redesigned structure. However, preliminary numerical analysis showed that excessive axial plastic deformation could easily occur in the columns of the braced bay. For this reason, the structures used in this study retain the beam and column sizes in the original test structure but adopt the brace sizes in the redesigned structure. The sizes of the relevant members are summarized in Table 4.2. Only the members relevant to the response in the longitudinal direction are included in the table.

Girders, columns and beams are made of wide flange ASTM-A36 steel; and braces are made of ASTM A500 Grade B square steel tubes. The yield strength and ultimate strength of the ASTM-A36 steel are taken to be 249 MPa and 450 MPa respectively, and the yield

strength and ultimate strength of the ASTM A500 Grade B steel are taken to be 317 MPa and 510 MPa respectively. In Frames A, B and C, all girder to column joints use moment connections.

## 4.3 Mathematical Model

Nonlinear dynamical analysis of three dimensional structures is often computationally expensive. To improve computational efficiency, three dimensional structures are simplified into a two dimensional representation and loads applied in plane. Shown in Figure 4.5 is a two dimensional mathematical model representing the three dimensional frame structure shown in figure 4.1 on page 93. In the figure, Frame AC represents Frames A and C combined, and Frame B is the same as in Figure 4.1. The mathematical model for the structures with X-bracing system is similar.

The representation of the three dimensional structures by a two dimensional mathematical model is based on the following assumptions: (1) Frames A and C have the same deformation; (2) Frames A, B, and C have the same horizontal displacement at the central girder-to-column joints of each floor. Since the structures under study have an almost symmetrical configuration and high torsional stiffness, the rotational response of the structure under translational earthquake motions should be minimal, and frames A and C should have about the same deformation. The second assumption is justified by the high in-plane stiffness of the floor system.

In Figure 4.5 each pair of nodes on Line 2 on the same floor level in Frame AC and Frame B are connected by an imaginary horizontal rigid bar so that the two nodes have the same horizontal displacement. This is actually done in the computer code by assigning the same degree of freedom (DOF) number to the horizontal displacement component of each pair of the corresponding nodes in the two frames. This avoids the increase in the condition number of the stiffness matrix that could otherwise be introduced by actually connecting the pairs of nodes with stiff auxiliary elements. Each member in Frame AC of the mathematical
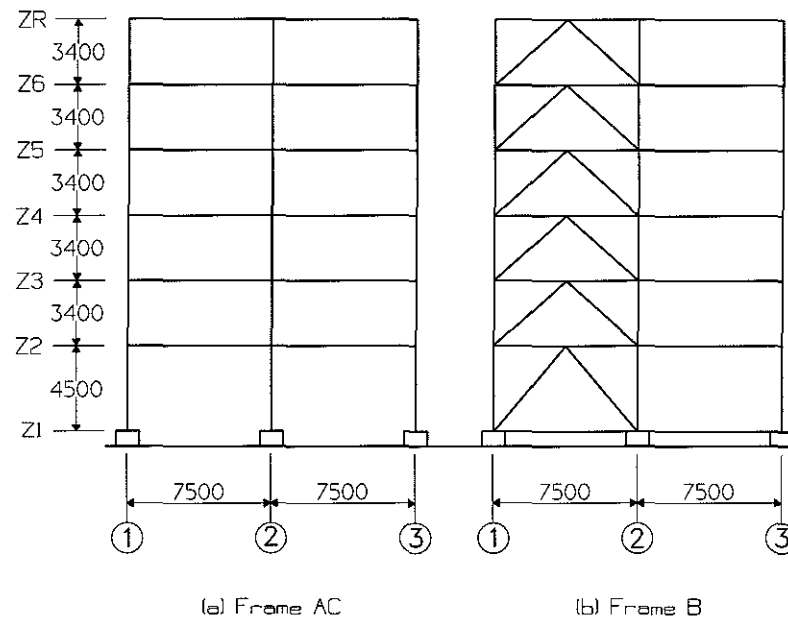
**Figure 4.5**: Mathematical model of the six-story building. Frame AC represents the combined Frames A and C in Figure 4.1. On Line 2, Frames A and B have the same horizontal floor displacement.

model is a side-by-side combination of the corresponding members in Frames A and C of the three dimensional structure. That is, a member in Frame AC has widths equal to the sum of the widths of the corresponding members in Frame A and Frame C of the three dimensional structures. The height of the members remains unchanged.

In the analysis of the structures, all the dead loads are included in the calculation of the vertical static load as well as the reactive mass which produces inertia force in dynamic response. The 1.77 kN/m$^2$ live load is also included in the calculation of the static vertical loads but, in accordance with UBC, is excluded from the calculation of the reactive mass. The 2.88 kN/m$^2$ live load used in the design of the slabs and beams is not included in the analysis of the frames. As thus, the resulting reactive mass is $88.0 \times 10^3$ kg (863 kN in weight) for the roof and $105.5 \times 10^3$ kg (1035 kN in weight) for each floor, and the resulting static vertical loads are 1287 kN for the roof and 1458 kN for each floor, as summarized in Table 4.3. The $P - \Delta$ effect of the static loads is taken into consideration.

To give an idea of the overall strength of the structures, push-over response of two of them, F6PV and F6PX, were obtained by subjecting the structures to lateral static loads with

| Story | Static Load | Reactive Mass |
|-------|-------------|---------------|
| Roof  | 1287 kN     | $88.0 \times 10^3$ kg |
| 6     | 1458 kN     | $105.5 \times 10^3$ kg |
| 5     | 1458 kN     | $105.5 \times 10^3$ kg |
| 4     | 1458 kN     | $105.5 \times 10^3$ kg |
| 3     | 1458 kN     | $105.5 \times 10^3$ kg |
| 2     | 1458 kN     | $105.5 \times 10^3$ kg |

**Table 4.3**: Static loads and reactive mass that are included in the analysis.

a distribution over the height calculated according to the Uniform Building Code. Figure 4.6 plots the base shear coefficient versus the roof lateral displacement for the two structures. The base shear coefficient is defined as the ratio between the base shear and the total reactive weight of a structure and is corresponding to the value

$$C_s = \frac{ZIC}{R_w} \tag{4.1}$$

in the Uniform Building Code. F6PX is seen to have an ultimate base shear coefficient 40% higher than F6PV. The lower lateral resistance for F6PV is attributed to the bending of the girders in the braced bay that accompanies the buckling of the braces. When comparing with the code requirement, it should be kept in mind that 100% yield strength is used here for all components.

All girder-to-column joints in the frames have a moment resistant connection. The force deformation characteristic of a joint is dependent on the panel zone, the modeling of which is summarized in Appendix A. More detailed information can be found in [10]. The effect of the finite dimension of the joints is not considered. Instead, the center-to-center dimensions are used. This results in a weaker structure and should be keep in mind when interpreting the results. Another simplification that reduces the strength and stiffness of the structure is

the exclusion of the effect of the composite floor system on the girder stiffness and strength.

The energy dissipation mechanisms considered in the analysis include hysteretic energy dissipation and viscous damping energy dissipation. The former is included in the element models and therefore there is no need for explicit consideration in the equation of motion. The viscous damping is represented by the Rayleigh damping matrix

$$[C] = \alpha_0[M] + \alpha_1[K] \tag{4.2}$$

where $[M]$ and $[K]$ are the mass matrix and the initial stiffness matrix, respectively, of the structure. A damping coefficient of 2%, calculated at $T = 0.2$ seconds and $T = 1.0$ seconds, is assumed. The use of linear viscous damping as given in the above form in nonlinear dynamic analysis is problematic. It can result in excessive energy dissipation by certain structural components. This is related to the fact that the damping matrix $[C]$ contains the constant initial stiffness matrix and the energy dissipation by this part of the damping matrix is related to the relative motion of the structure. When the stiffness of a structural component is reduced because of yielding or buckling, large relative motion can result, causing excessive energy dissipation by viscous damping. To avoid this potential problem, the stiffness of structural components that are most likely to experience such stiffness reduction are excluded from the calculation of the damping matrix $[C]$. These include the braces and panel zones.

As was shown in the Chapter 2, the mass of a brace can have significant effect on the response of the brace under high frequency vibration. But this is not expected to occur for the structures considered in this chapter since the fundamental periods of these structures are relatively long (0.8 seconds under small amplitude vibrations and longer under large amplitude vibrations). To confirm this, structure F6CV was subjected to the Kobe and Sylmar ground motions (see Appendix B) with and without the mass of the braces being included. Table 4.4 lists the peak story drift values of the structure obtained under the two conditions, and the differences are indeed very small. Based on this result, the mass of the braces is ignored for the structures considered in this study.

| Story | Kobe Ground Motion | | Sylmar Ground Motion | |
|:---:|:---:|:---:|:---:|:---:|
| | With Mass | Without Mass | With Mass | Without Mass |
| 1 | 0.129 m | 0.129 m | 0.087 m | 0.093 m |
| 2 | 0.318 m | 0.323 m | 0.211 m | 0.215 m |
| 3 | 0.535 m | 0.532 m | 0.180 m | 0.186 m |
| 4 | 0.093 m | 0.097 m | 0.026 m | 0.026 m |
| 5 | 0.060 m | 0.062 m | 0.049 m | 0.048 m |
| 6 | 0.029 m | 0.030 m | 0.027 m | 0.027 m |

**Table 4.4**: Effect of brace mass on peak story drifts for the Kobe and Sylmar ground motions. The results were obtained with and without the mass of the braces.
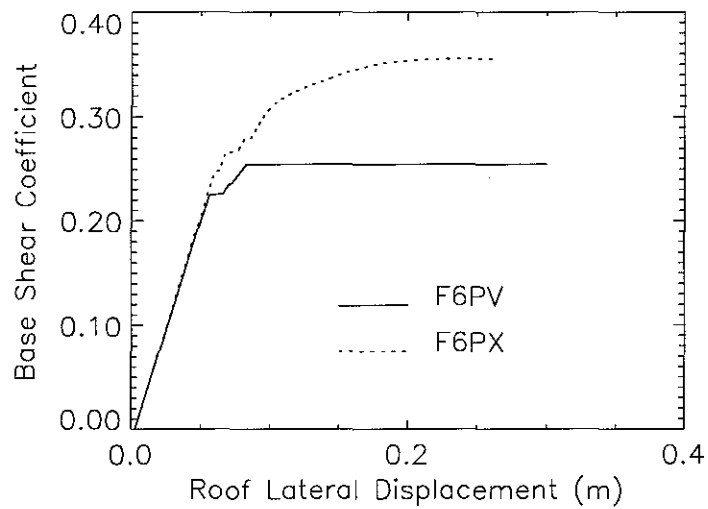


**Figure 4.6**: Push-over responses for F6PV and F6PX.

# 4.4 Response Comparison

In this section the responses of the five structures listed in Table 4.1 under the Kobe and Sylmar ground motions are compared to study their earthquake performance and the effect of different bracing systems. Besides the original records, ground motions derived from the two records through scaling, as described in Appendix B on page 151, are also used. Since the responses are affected by the frequency characteristics of the structures, one structure may have smaller response than another under certain ground motions and have larger response under other ground motions. It is therefore necessary to consider the comparison under ground motions with a wide range of frequency contents. Temporal scaling is used to generate such ground motions. Another use of the scaled ground motions is to study the response of the structures under ground motions of different intensities. It will be apparent from the following sections that the employed ground motions cause very severe nonlinear response in the frames analyzed, beyond what would be needed to cause local buckling and rupture in highly deformed regions. Even though such behavior is not modeled, the results are useful for evaluating the relative merits of the bracing systems.

The comparison of the earthquake performance of structures can be based on a number of response quantities: displacement, deformation, force and energy dissipation. Under linear response the stress or force level is considered a good indication of the response amplitude. However few structures are designed to remain elastic even under moderate earthquakes. For structures that undergo significant plastic deformation, these quantities are poor indicators because once yielding occurs they are insensitive to the response level. Under such conditions, deformation, displacement and energy dissipation are more appropriate measures of the response.

Peak deformation such as story drift indicates the extent of repair that is required to restore a partially damaged structure and is also related to non-structural damage. The energy dissipated is an indication of the accumulated damage sustained by the structure or its components and is related to the low cycle fatigue failure of structural components [33,34]. Based on the above arguments, the comparisons in this study emphasize mainly the response

quantities of deformation, displacement and energy dissipation.

### 4.4.1 Conventional Chevron Braces Versus Conventional X-Braces

It is commonly recognized that the buckling of a brace in a chevron bracing system can result in an unbalanced vertical force at the brace-to-girder junction because of the difference in the tension and compression capacities of the braces. The unbalanced vertical force can be estimated from

$$P_v = (P_y - P_c)\sin\theta \tag{4.3}$$

where $P_y$ is the tension yield capacity, $P_c$ is the compression capacity, and $\theta$ is the slope angle of the braces.

The potential effect of the unbalanced vertical force on the deformation of the braced-bay girders can be gauged by comparing the capacity of the girders with the moment resulting from the unbalanced vertical force. Taking the first floor braced-bay girder as an example and assuming fixed end conditions, the maximum unbalanced vertical force that can be supported by the girder is

$$P_{max} = \frac{8M_p}{L} = \frac{8 \times 407\text{kN} \cdot \text{m}}{7.5\text{m}} = 434\text{kN} \tag{4.4}$$

where $M_p$ is the plastic moment capacity and L the length of the girder. The tension yield force of the $\square\,7 \times 7 \times 1/4$ brace is 1383 kN and its post buckling compression capacity is about 20% of the tension yield capacity, or 277 kN, as estimated from Figure 4.10(a). The resultant unbalanced vertical force $P_v$ is 850 kN, which is much higher than $P_{max}$. From this result, there is little doubt that the girders will form plastic hinges under even moderate ground shaking.

The immediate consequence of the formation of plastic hinges in the girders is the severe bending deformation sustained by the girders, as shown in a snapshot in Figure 4.7 of the deformed braced-bay in F6CV under the Kobe ground motion. The lateral floor displacement time histories and the vertical mid-span displacement time histories of the girders of
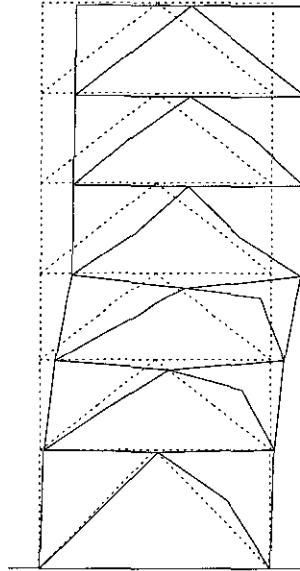
**Figure 4.7**: Snapshot of the deformed braced bay in frame F6CV at $t = 8.5$ seconds during the Kobe ground motion. It was drawn to scale in each of the horizontal and vertical directions.

the structure are shown in Figures 4.8 and 4.9. From 0 to 3 seconds into the time histories, there is little vertical displacement at the brace-to-girder junctions. Shortly after 3 seconds, initial buckling occurs in the left brace of the first story, as can be seen in Figure 4.11, and the mid-span vertical displacement in the second floor girder shows a sudden increase. Significant vertical mid-span displacements occur in other girders at about 3.5 seconds when initial buckling occurs in the braces attached to those stories. It is seen that most of the girders suffer significant permanent downward deflection. This bending can cause local buckling of the girder flange as was found in the Kobe earthquake as well as experimental results, and special attention in the detailing of the brace-to-girder connection area has been suggested [12].

Another consequence of the flexibility of the girders is that the effectiveness of the bracing system is also compromised. The brace under tension is not able to reach its tension
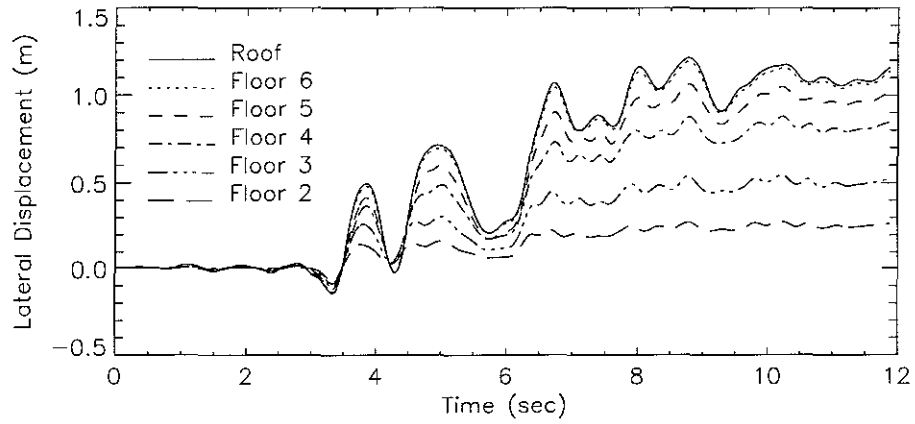
**Figure 4.8**: Lateral floor displacement time histories (relative to the ground floor) of F6CV under the Kobe ground motion.
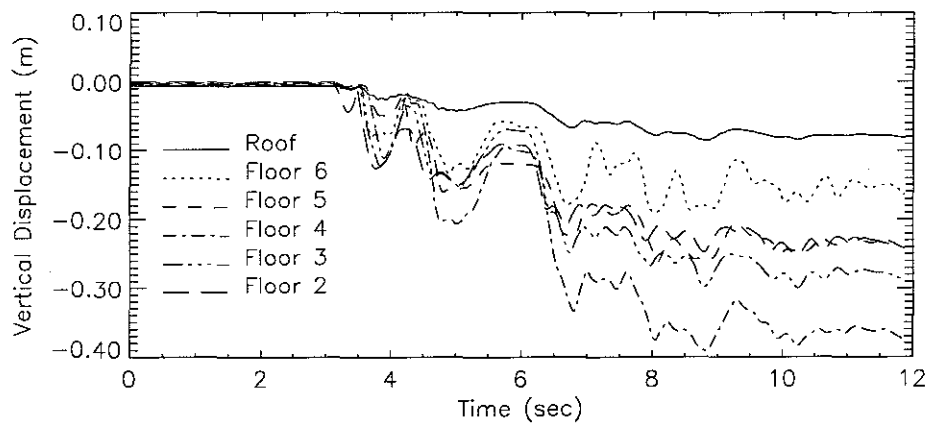


**Figure 4.9**: Vertical mid-span displacement time histories of the girders in the braced bay of F6CV under the Kobe ground motion.
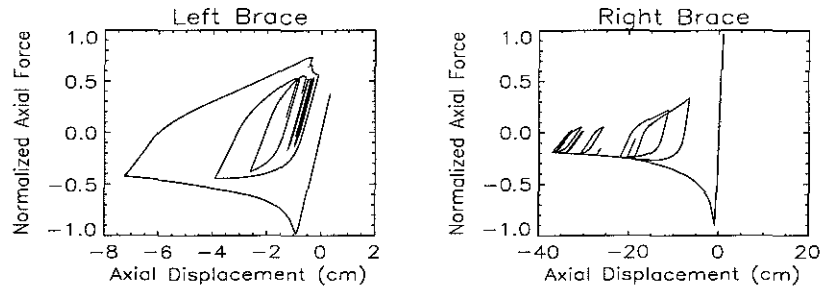
(a) 1st story
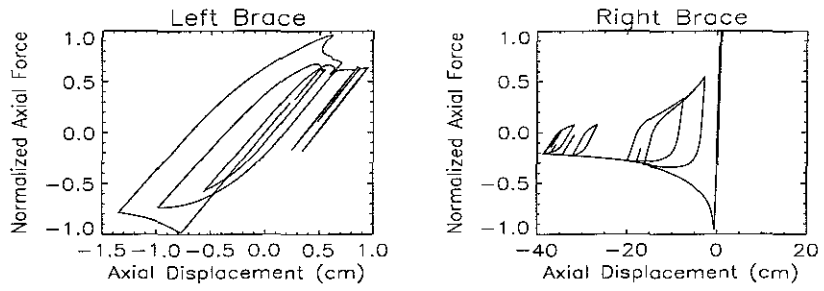
(b) 2nd story
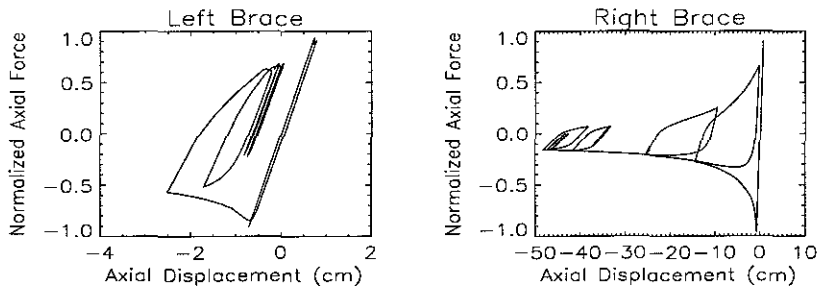
(c) 3rd story

(d) 4th story

**Figure 4.10**: Hysteresis loops for braces in F6CV under the Kobe ground motion.
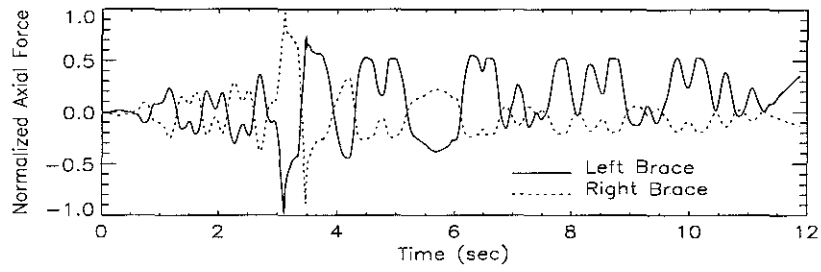
(a) 2nd floor
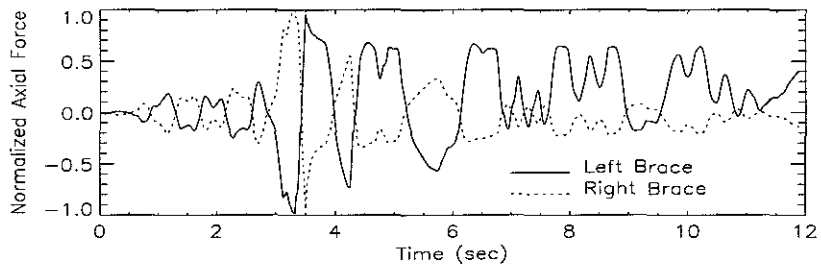


(b) 3rd floor
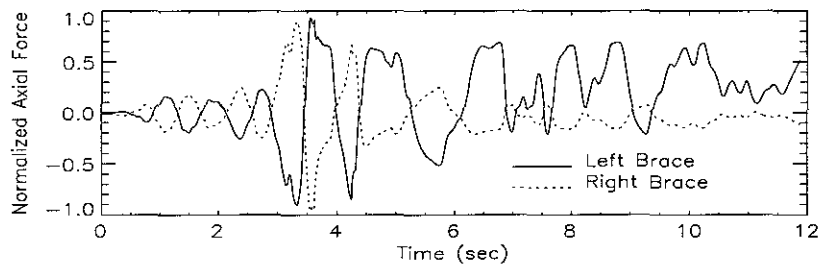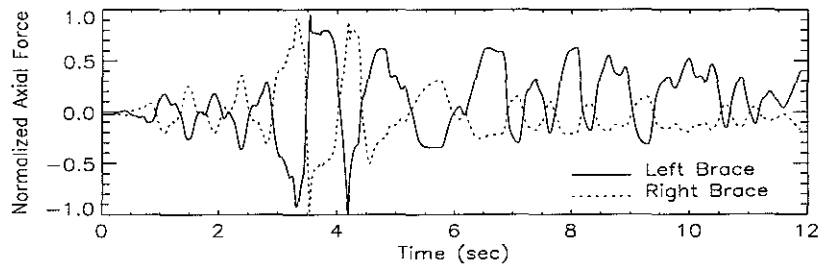


(c) 4th floor



(d) 5th floor

**Figure 4.11**: Axial force time histories for braces in F6CV under the Kobe ground motions.

capacity because of the girder's inability to support the unbalanced vertical force once the brace under compression buckles. Because of this, the deformation of the chevron braces is severely biased: extremely large compression but very little extension, as can be seen in the hysteresis loops in Figure 4.10. The axial force in the plots is normalized by the tension capacity of the brace for easy comparison. None of the braces undergo inelastic elongation of any significant magnitude, and the right braces provide very little resistance after the second major cycle in the time histories as shown in Figure4.11. The hysteresis loops for the braces are severely underdeveloped and little energy is dissipated by the them (note that the hysteresis plots use different scales for the axial displacement axis.) High localized strains in the buckled braces would certainly cause local buckling and rupture observed in test results [4,5,8].

It is interesting to note that, when one brace buckles and the compressive axial force drops suddenly, the tensile axial force in the other brace in the same story also experiences a sudden drop, as shown in Figure 4.11(a) for example. The reason for this is that when one brace buckles, the girder experiences a sudden downward deflection because of the unbalanced vertical force at the brace-to-girder junction, thus releasing some of the tensile force carried by the other brace.

The above results are for F6CV which has a clamp-ended chevron bracing system. The performance of F6PV, which has pin-ended chevron braces, is worse. The compressive deformation of the braces is more severe, and the forces developed and energy dissipated in the braces are lower as can be seen in Figure 4.12. In fact the axial force resisted by the right braces in some of the stories is practically zero after initial buckling at about 3.5 seconds into the time history, as depicted in Figure 4.13.

The girders in the braced bay can have significant mid-span vertical displacement even under moderate ground motion intensity. Figure 4.14 shows the time histories of mid-span vertical displacement of the 4th-floor braced-bay girder in F6PV under the Kobe ground motion scaled to 40% to 100% of its original amplitude. The peak vertical mid-span girder displacement under 60% of the Kobe ground motion is more than 15 centimeters, enough
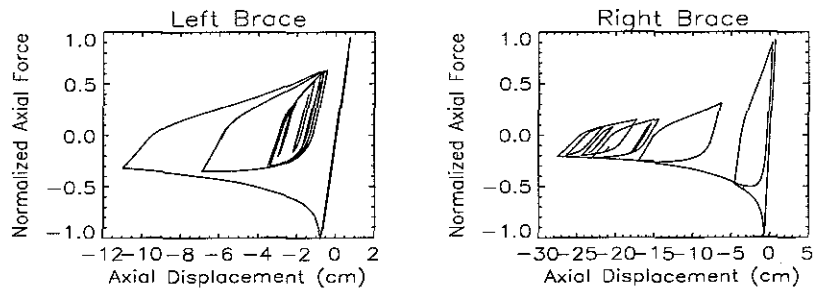
(a) 1st story
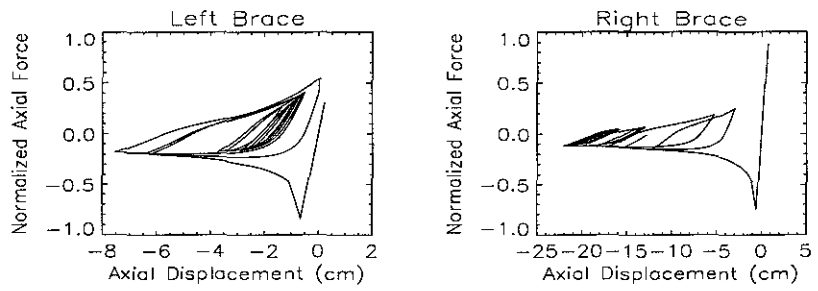


(b) 2nd story
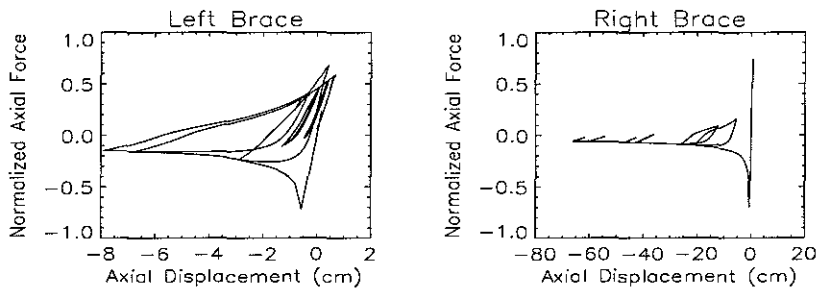


(c) 3rd story
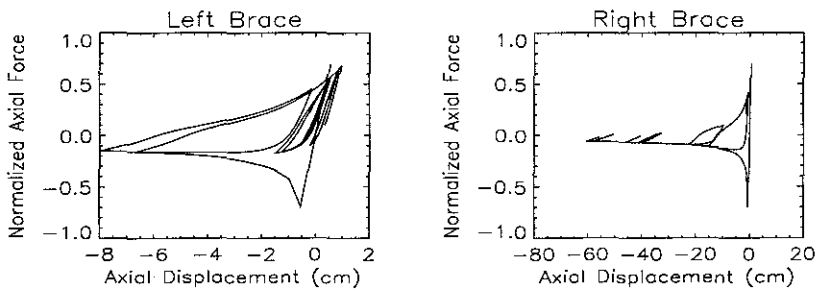


(d) 4th story

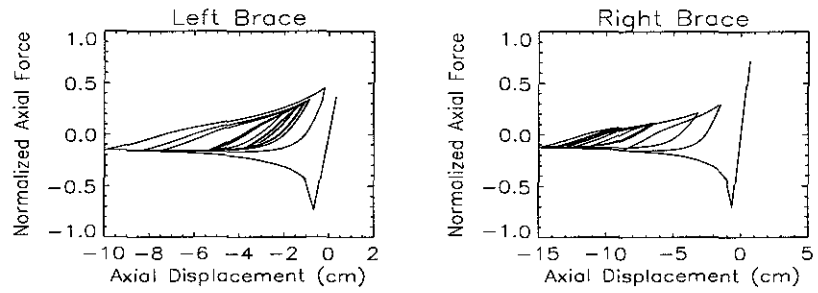**Figure 4.12**: Hysteresis loops for braces in F6PV under the Kobe record.

(a) 2nd floor
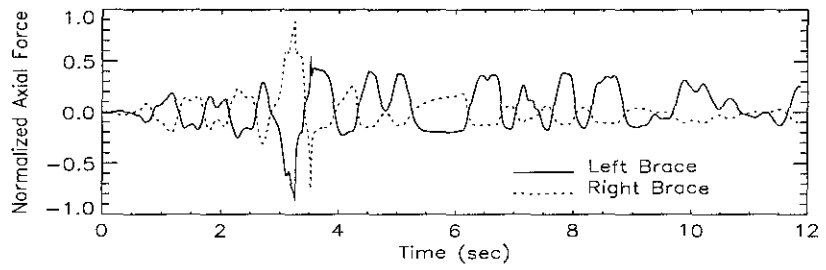


(b) 3rd floor
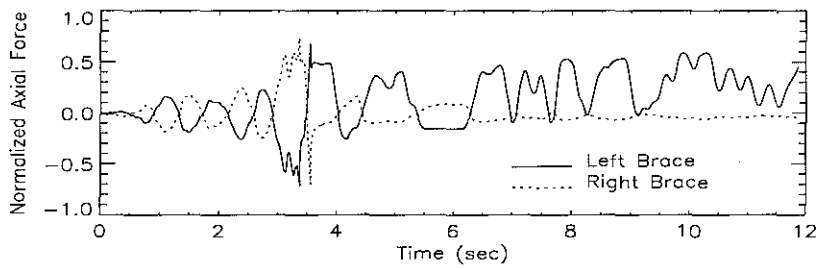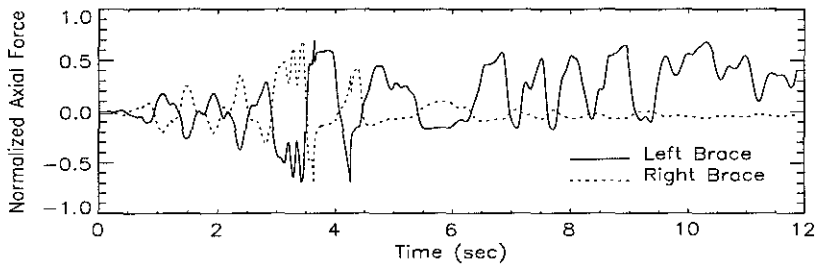


(c) 4th floor



(d) 5th floor

**Figure 4.13**: Axial force time histories for braces in F6PV under the Kobe ground motion.

to cause damage that requires major repair.
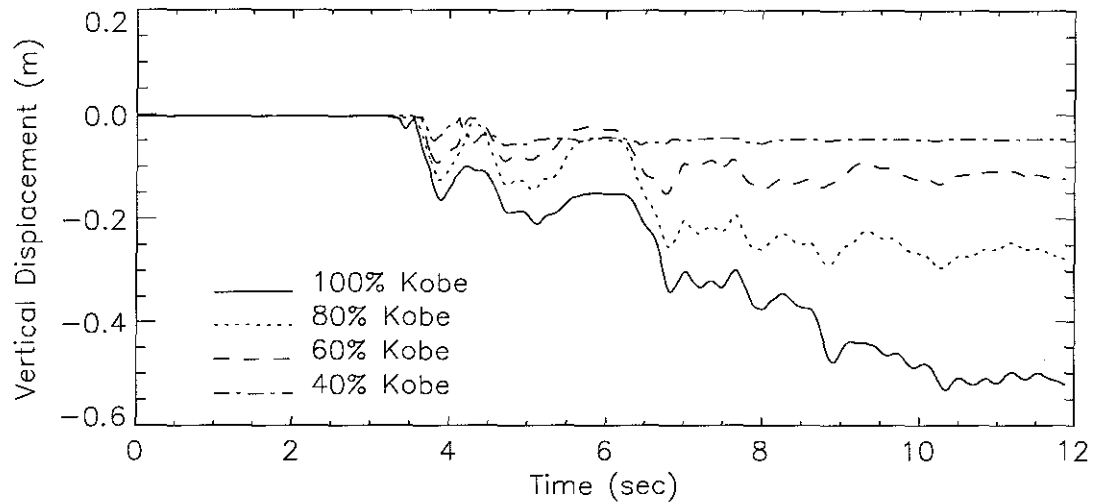


**Figure 4.14**: Time histories of mid-span vertical displacement of the 4th-floor girder in the braced bay of F6PV under the Kobe ground motion scaled to different amplitudes.

In summary, girders in chevron-braced frames may suffer severe bending and the braces have only limited effectiveness. The plastic bending of the girders is able to dissipate some energy, but the bending may cause buckling or rupture of the girder flanges. It is also not desirable to allow large deformation in the girders from the perspective of post-quake repair. The unbalanced vertical force caused by the braces is large and it may not be economically feasible to design the girders strong enough to support the unbalanced vertical force caused by the brace buckling.

To reduce the unbalanced vertical force on the girders, an X-bracing system can be used in place of a chevron bracing system. Each X spans either one or two stories as shown in Figure 4.2 on page 95. The unbalanced force at the mid-span girder connection (floors 3 and 5) resulting from brace buckling is expected to be much smaller. This is demonstrated in Figure 4.15 which should be compared with Figure 4.9. The braces are also able to develop their tension capacity, as shown in Figures 4.16 and 4.17. The deformation of the braces is more balanced; the hysteresis loops are fuller; and some compressive resistance is retained. Also, the portion of the base shear resisted by the first-story braces is larger in the

X-braced F6CX than in the chevron-braced F6CV, as shown in Figure 4.18. As also seen in Figure 4.18, the effectiveness of the clamp-ended braces (F6CV and F6CX) is superior to that of the pin-ended braces (F6PV and F6PX). All these results are for the Kobe ground motions. The behavior of the bracing systems is similar under the Sylmar ground motions, except that the response is generally less severe, as shown in Figure 4.19.
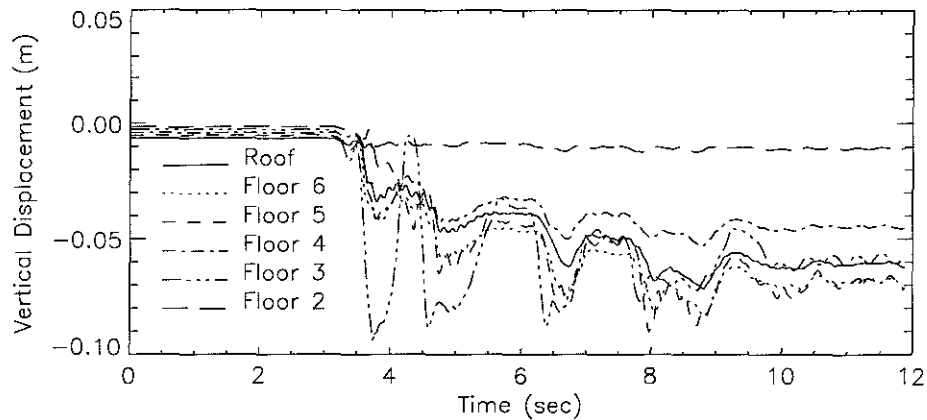


**Figure 4.15**: Vertical mid-span displacement time histories of the girders at floors 3 and 5 in the braced bay of F6CX under the Kobe ground motion.

The difference between the chevron bracing system and X-bracing systems is also reflected in the overall response of the structures. The energy dissipated by different parts of a structure is one indication of the effectiveness of a bracing system. The energy dissipation can be divided into two parts: that dissipated by the bracing system and that dissipated by other non-brace structural components. A more effective bracing system will dissipate a larger portion of the energy. The X-bracing system shows a clear advantage over the chevron bracing system in reducing the energy demand on non-brace structural components, as can be seen by comparing the energy dissipation between F6PV and F6PX, and between F6CV and F6CX, respectively, shown in Figures 4.20 and 4.21. Under the Kobe ground motion, the X-bracing systems in F6PX and F6CX dissipate almost twice as much energy as the chevron bracing systems in F6PV and F6CV, respectively, while the energy demand on the the non-brace structural components is reduced. The comparison under the Sylmar
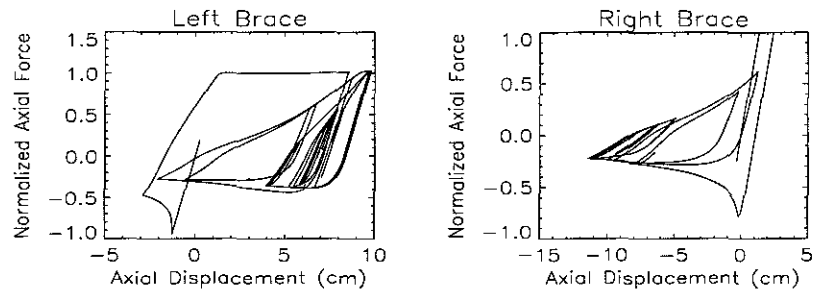
(a) 1st floor
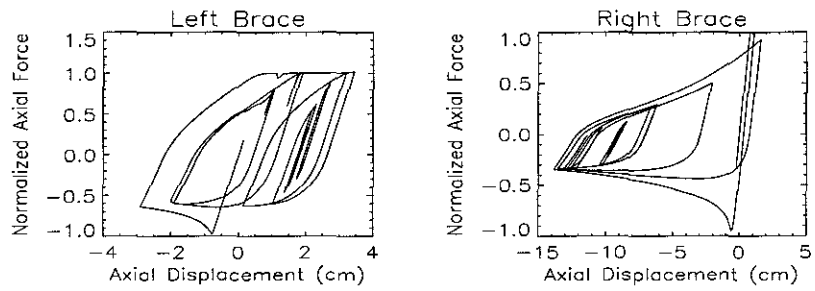


(b) 2nd floor
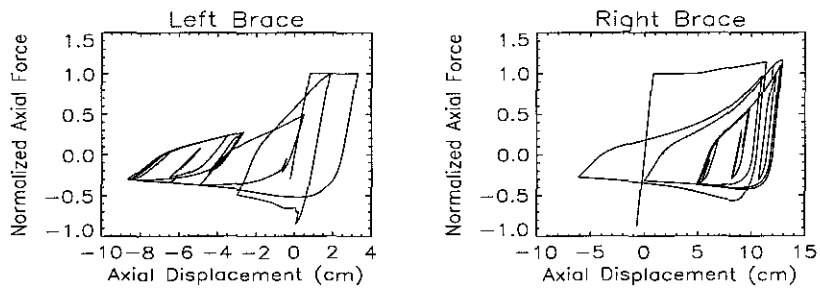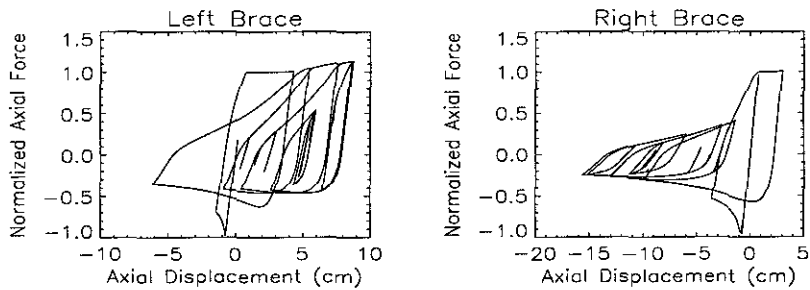
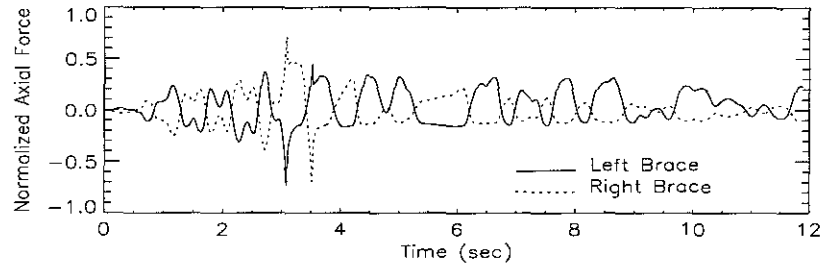

(c) 3rd floor



(d) 4th floor

**Figure 4.16**: Hysteresis loops for braces in F6CX under the Kobe ground motion.
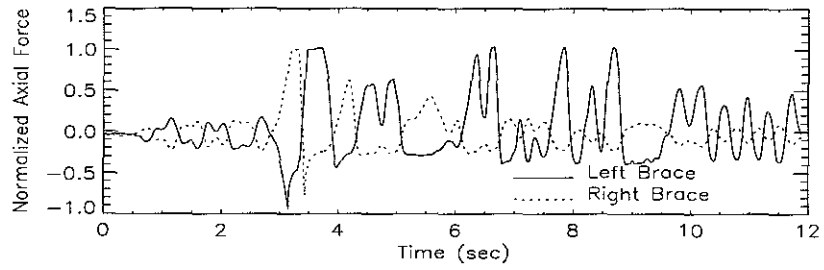
(a) 1st floor
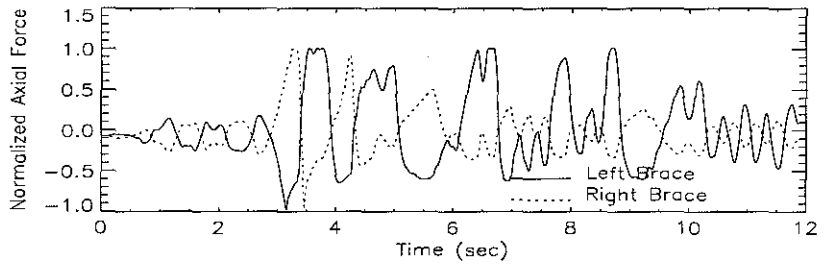


(b) 2nd floor
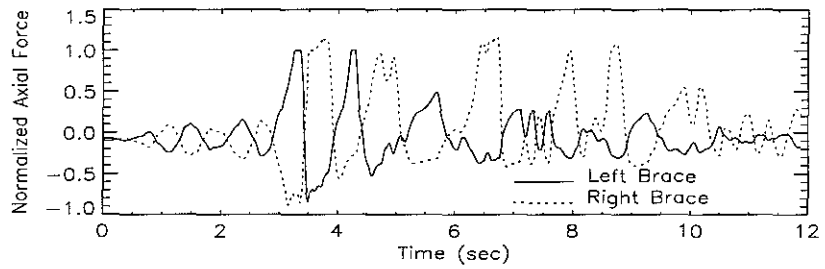


(c) 3rd floor
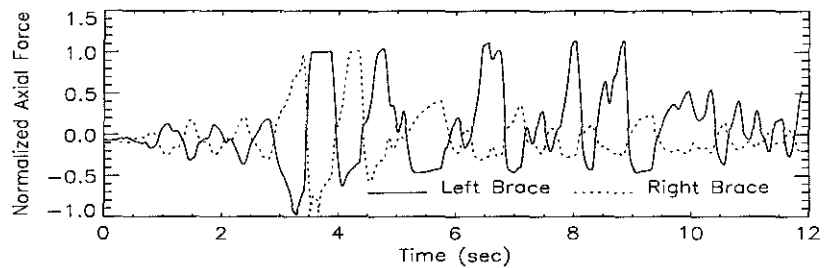


(d) 4th floor

**Figure 4.17**: Axial force time histories for braces in F6CX under the Kobe ground motion.

ground motion is similar.

Under the Kobe ground motion, the peak floor lateral displacement and peak story drift in the structures with an X-bracing system are also significantly lower than those in the structures with a chevron bracing system, as can be seen from Figures 4.22, 4.23 and 4.25. In terms of maximum peak story drift, similar can be said on the comparison between the structures with chevron bracing system and those with X-bracing system under the Sylmar ground motion. But the average peak story drift of F6CX is somehow slightly larger than that of F6CV, as shown in Figures 4.26 and 4.24.

One possible reason for this is that, because the peak response occurs in the first major cycle in the time history under the Sylmar ground motion, the bracing system has not experience much deterioration, and therefore the different susceptibility to deterioration of different bracing systems can not be differentiated.

## 4.4.2   Effect of End Conditions

In Chapter 2 it was shown that the end condition of a brace has significant effect on its load and energy dissipation capacities. How this affects the overall response of a braced frame structure under earthquake ground motions is the focus of this sub-section.

Figures 4.18 and 4.19 show the time histories of the total base shear and the portions of base shear resisted by columns and by braces in F6PV, F6CV, F6PX and F6CX under the Kobe and Sylmar ground motions. Initially the braces in all structures resisted almost the entire base shear, indicating that the lateral stiffness of the structures is provided mainly by the bracing systems. The portion of base shear resisted by the braces is reduced significantly after the initial buckling of the braces. However the degree of reduction is different for structures with different bracing systems, with reduction more severe in bracing systems with pinned ends than in those with clamped ends.

In terms of peak lateral roof displacement, the structures with clamp-ended braces performed clearly better than those with pin-ended braces, as shown in Figure 4.22. But the comparison of the peak lateral displacement at individual stories is not as clear cut. A more
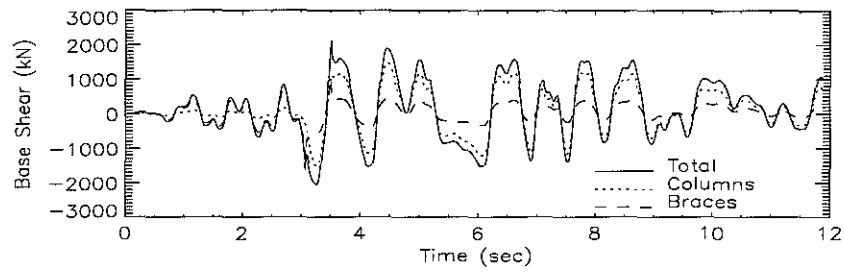
(a) F6PV
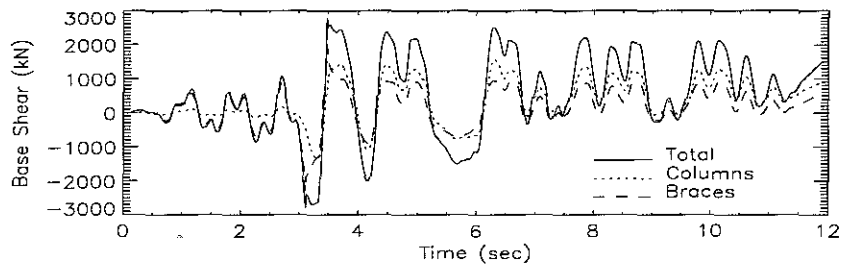


(b) F6CV
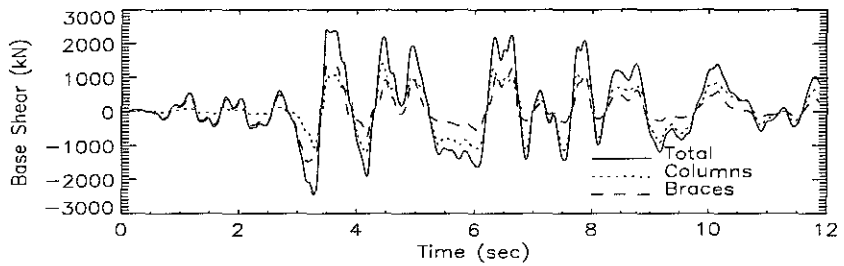


(c) F6PX
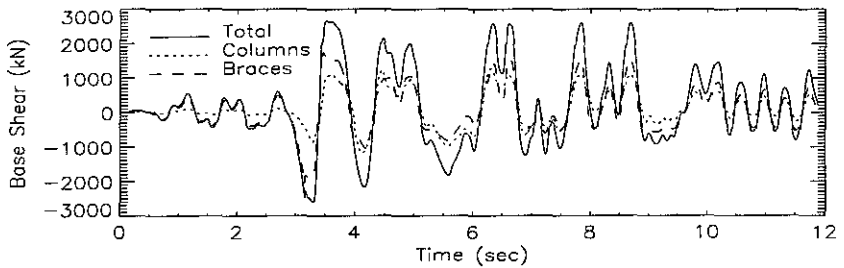


(d) F6CX

**Figure 4.18**: Base shear time histories under the Kobe ground motion.
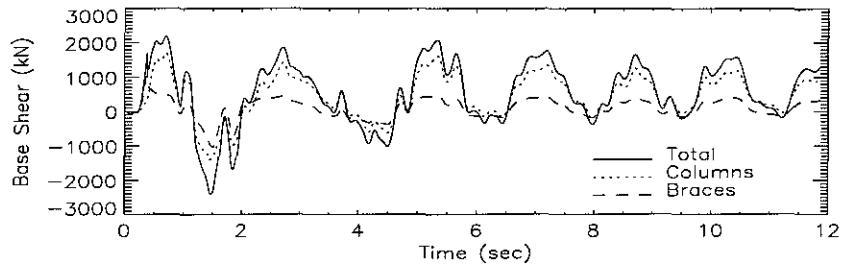
(a) F6PV
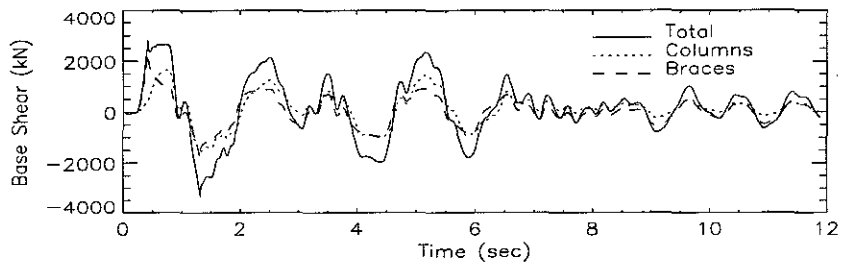


(b) F6CV
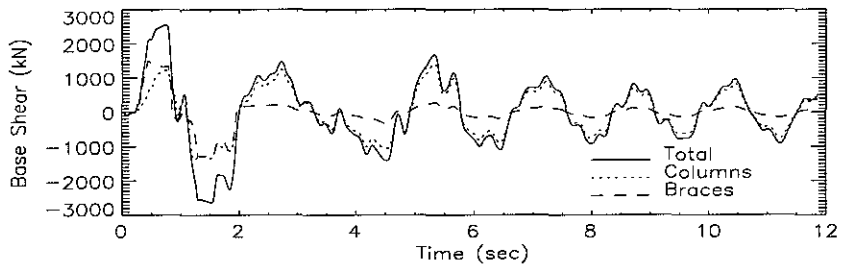


(c) F6PX
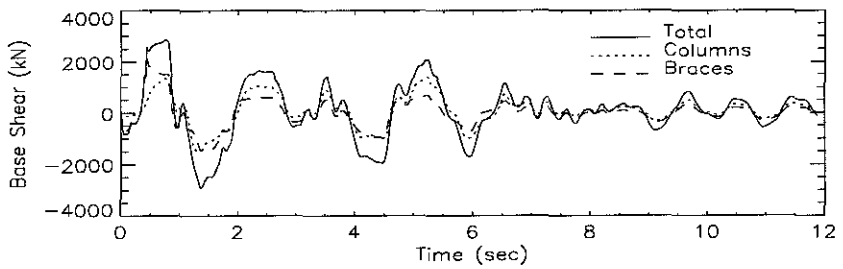


(d) F6CX

**Figure 4.19**: Base shear time histories under the Sylmar ground motion.
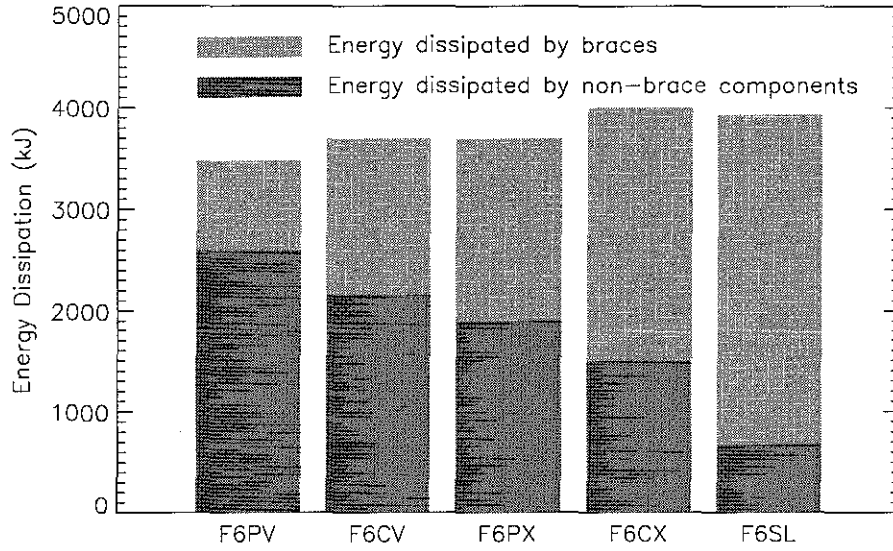
**Figure 4.20**: Plastic energy dissipation on different structural components under Kobe ground motion.
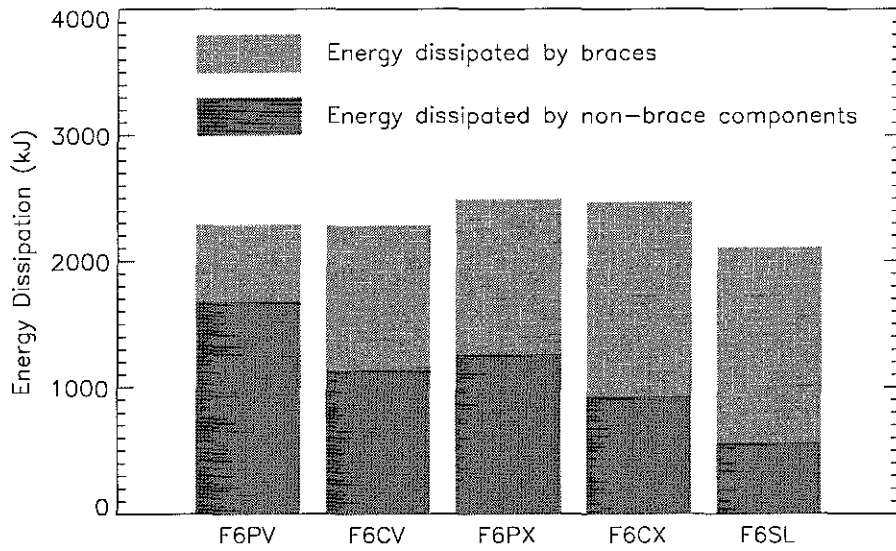


**Figure 4.21**: Plastic energy dissipation on different structural components under Sylmar ground motion.

(a) Under Kobe record

(b) Under Sylmar record
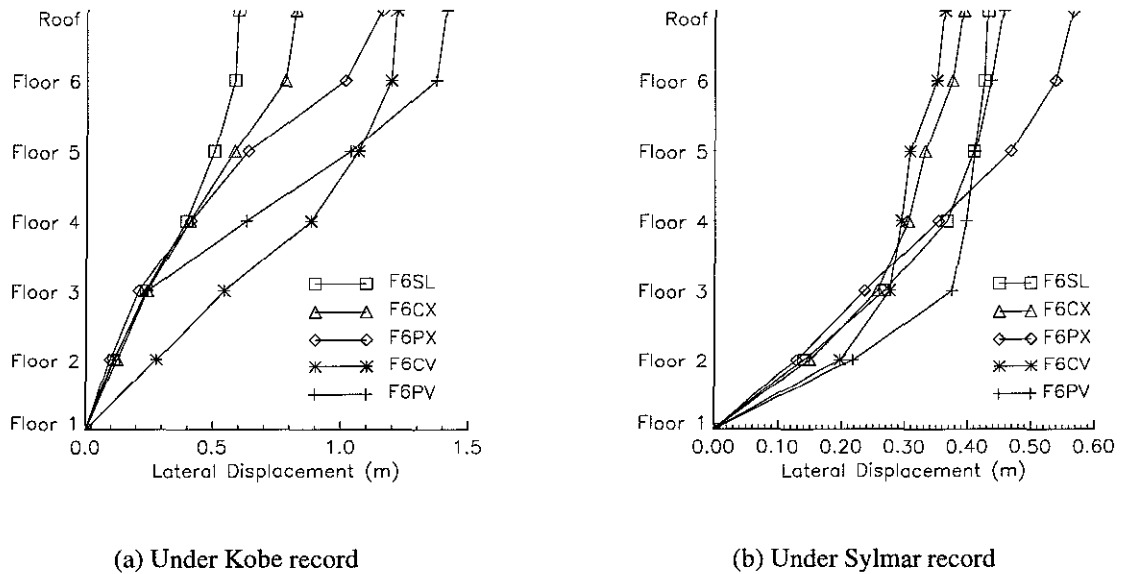
**Figure 4.22**: Peak lateral displacement of F6PV, F6CV, F6PX, F6CX and F6SL under the Kobe and Sylmar ground motions.

meaningful comparison is with the peak story drift in terms of percentage story height. As shown in Figures 4.23 and 4.24, under both the Kobe and Sylmar ground motions, structures with clamp-ended bracing systems always have smaller maximum peak story drift than their counterparts with pin-ended bracing systems.

Since the maximum peak story drift depends on the vertical distribution of the strength of a structure and may be affected by a single weak story, another useful measurement is the average peak story drift, as shown in Figures 4.25 and 4.26. It is seen that for the structures under consideration, the trend of comparison is similar to that for maximum peak story drift, but the degree of difference is different.

Bracing systems with clamp-ended bracing members generally dissipate more energy than those with pin-ended bracing members, and the plastic energy demand on the non-brace structural components is lower for structures with clamp-ended braces than for those with pin-ended ones, as shown in Figures 4.20 and 4.21.

Since the bracing system provides most of the elastic lateral stiffness of a frame struc-
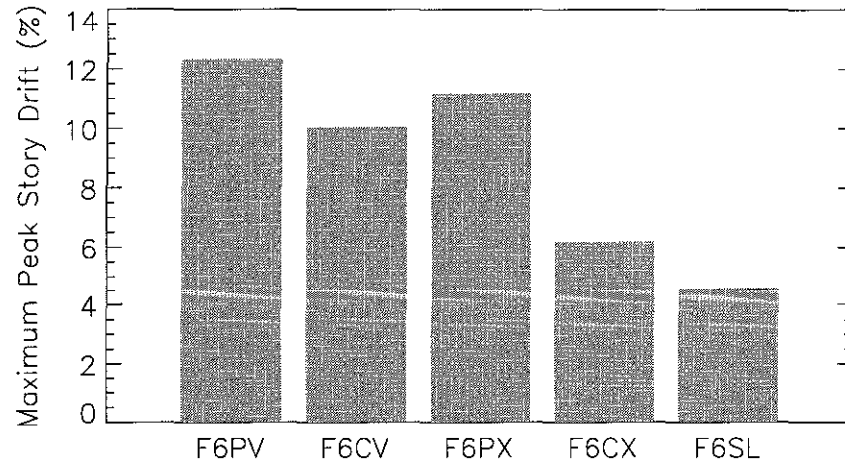
**Figure 4.23**: Maximum story drifts for F6PV, F6CV, F6PX, F6CX and F6SL under the Kobe ground motion.
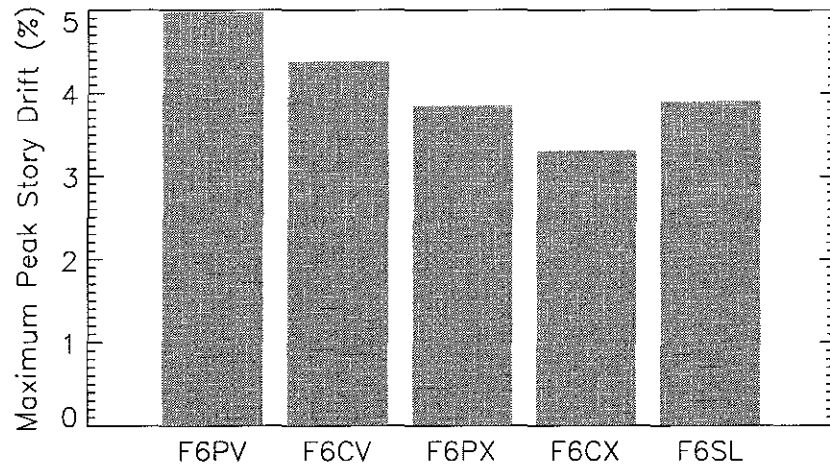


**Figure 4.24**: Maximum story drift for F6PV, F6CV, F6PX, F6CX and F6SL under the Sylmar ground motion.
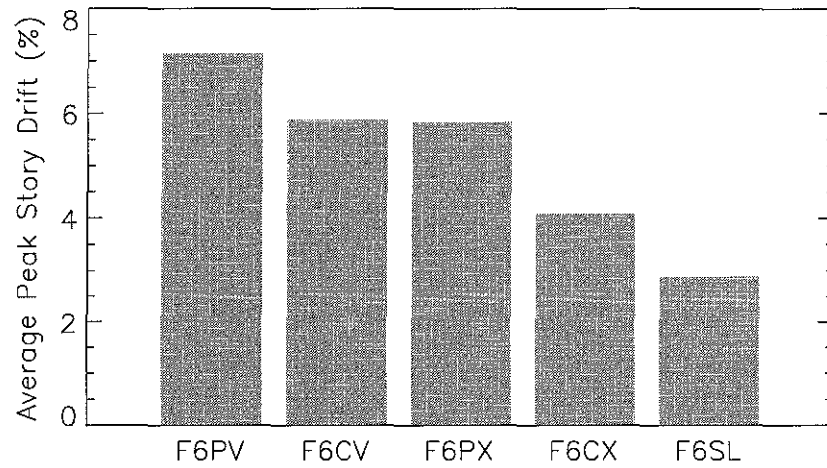
**Figure 4.25**: Average peak story drift for F6PV, F6CV, F6PX, F6CX and F6SL under the Kobe ground motion.
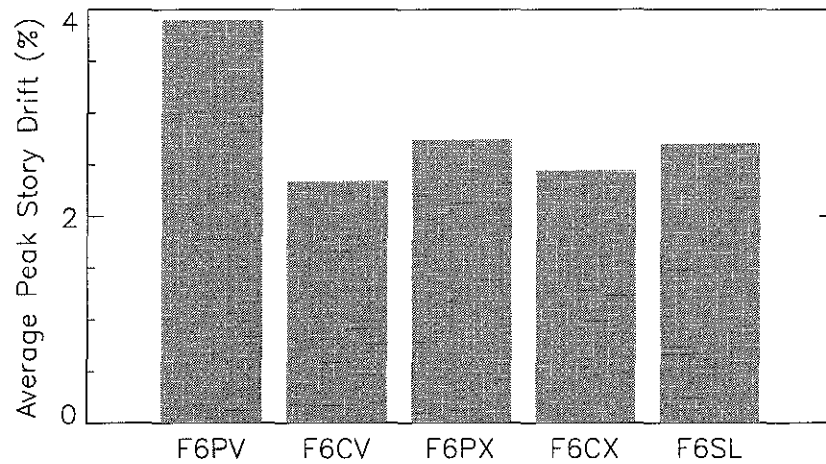


**Figure 4.26**: Average peak story drift for F6PV, F6CV, F6PX, F6CX and F6SL under the Sylmar ground motion.

ture, one expected consequence of the deterioration of the bracing system is the reduction in the stiffness of the structure. This reduction will be reflected in the frequency contents of the response of the structures. To study this change, Fourier spectra are computed for the roof lateral velocity time histories for the time period after the first-story braces have buckled under the Sylmar ground motion record. These spectra are compared with those computed from small amplitude response obtained by scaling the same ground motion history to 1% of its original amplitude. The time period used here is between 1.25 and 12.0 seconds. The Fourier spectra are normalized so that the maximum value is 1 to facilitate easier comparison, as shown in Figure 4.27.

Under the scaled Sylmar record the response of the structure is basically linear with a predominant frequency of about 1.25 Hz (T=0.8 seconds), and the spectra of the four structures with conventional bracing systems show little difference. Under the unscaled ground motion history, the predominant frequencies of all four structures shift lower to about 0.6 Hz (T=1.7 seconds). However, the shift of the frequency content is different between the structures with clamp-ended braces and those with pin-ended braces. Specifically, the spectra of the structures with clamp-ended braces contain more high frequencies than those of their counterparts with pin-ended braces, as can be seen by comparing Figures 4.27(a) with 4.27(b), and Figures 4.27(c) with 4.27(d). But the effect of the bracing configuration (X-bracing versus chevron bracing) is small under this particular ground motion.

The Kobe and Sylmar ground motions seem to excite different modes of vibrations in the structures, as can be seen in Figure 4.22. The Kobe ground motion tends to cause largest story drift in the upper middle stories of the structures, while the Sylmar ground motion tends to cause the largest story drift in the lower stories. This is what should be expected because the large difference in the frequency contents of these two ground motion histories as shown in Figures B.1 and B.2 in Appendix B.
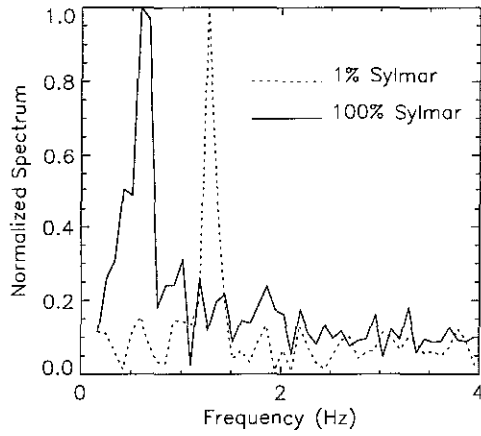
(a) F6PV
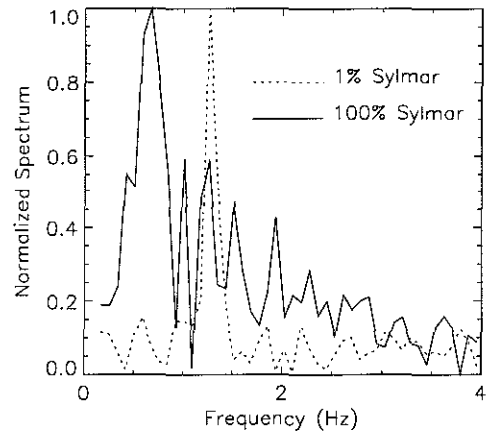
(b) F6CV
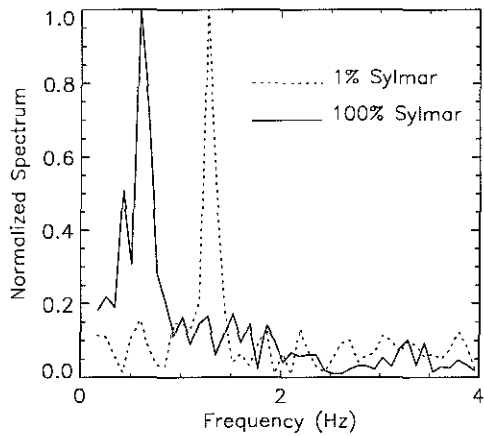
(c) F6PX
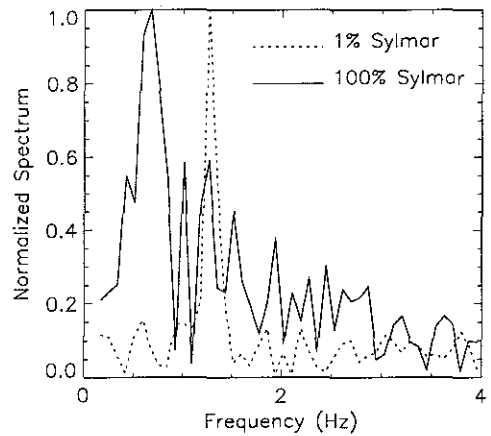
(d) F6CX

**Figure 4.27**: Roof lateral velocity spectra of structures under ground motions of different intensities.

125
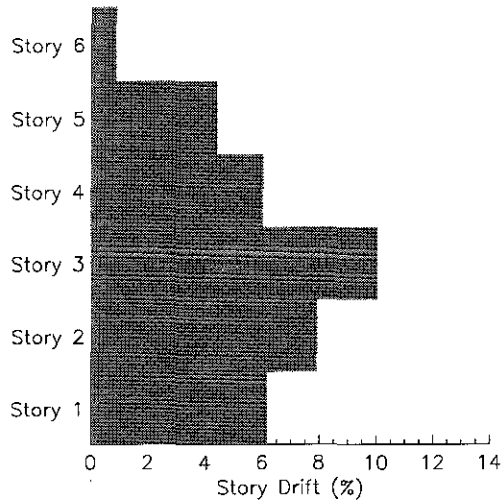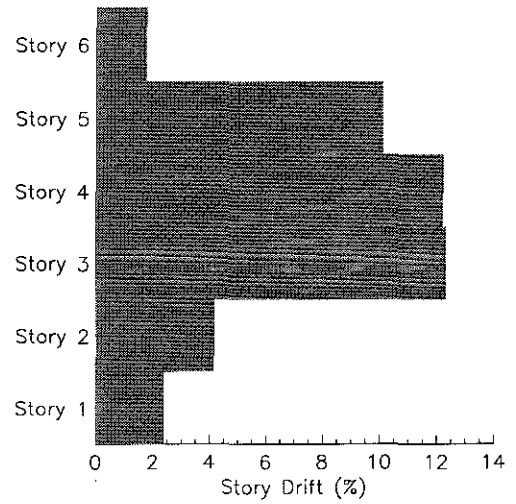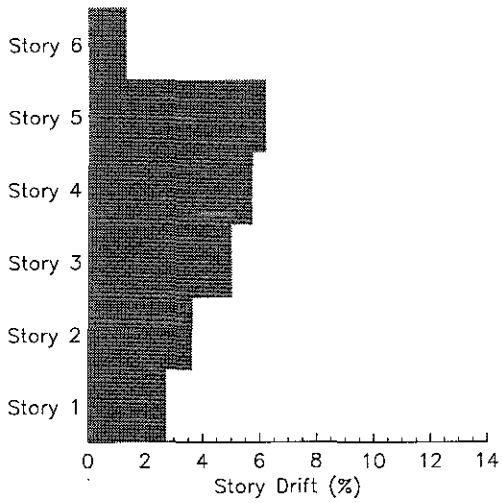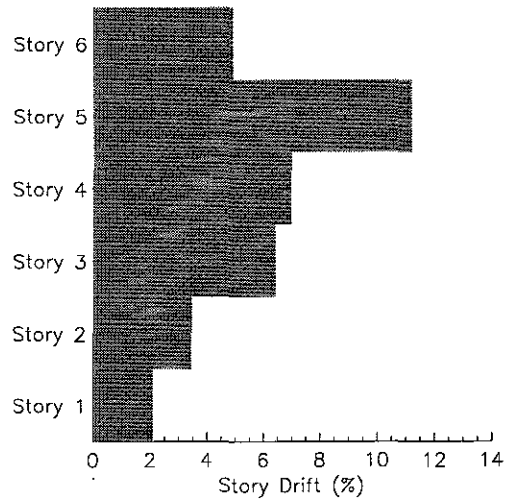


(a) F6CV



(b) F6PV



(c) F6CX



(d) F6PX

**Figure 4.28**: Peak story drifts of F6CV, F6PV, F6CX and F6PX under the Kobe record.
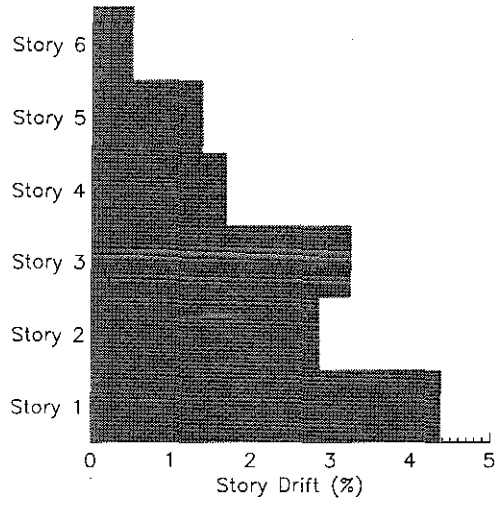
(a) F6CV
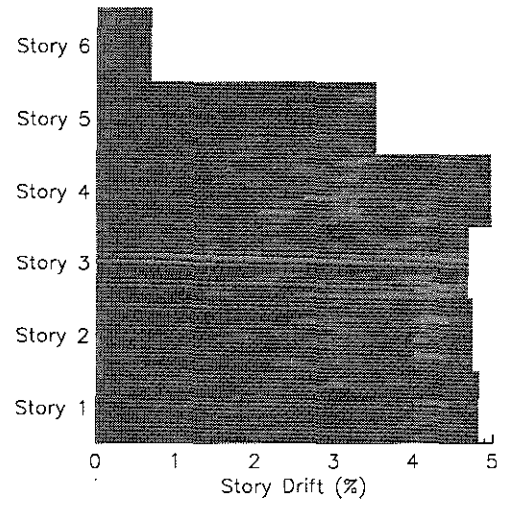
(b) F6PV
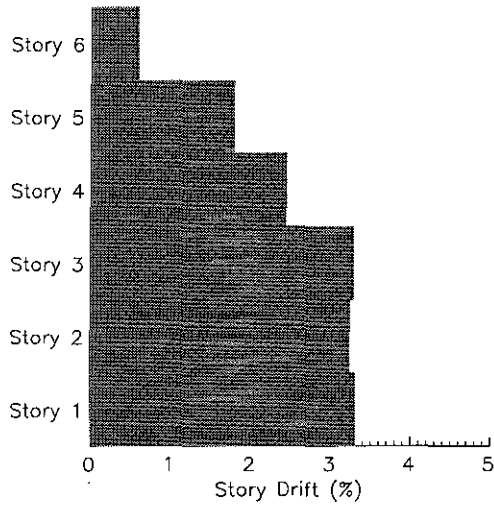
(c) F6CX
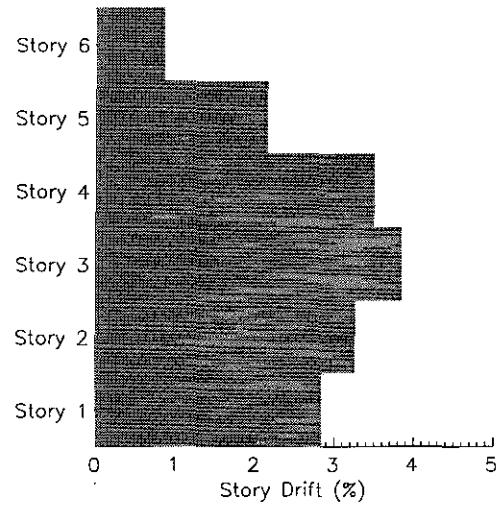
(d) F6PX

**Figure 4.29**: Peak story drifts of F6CV, F6PV, F6CX and F6PX under the Sylma record.

## 4.4.3 Structure With Non-Buckling Braces

As is expected, the non-buckling braces have very stable hysteresis loops, as shown in Figures 4.30 and 4.31. Under both the Kobe and Sylmar ground motions the braces carry a large portion of the base shear for the entire loading history, as evidenced in Figures 4.32 and 4.33. The bending of the girders in the braced bay is also much smaller.
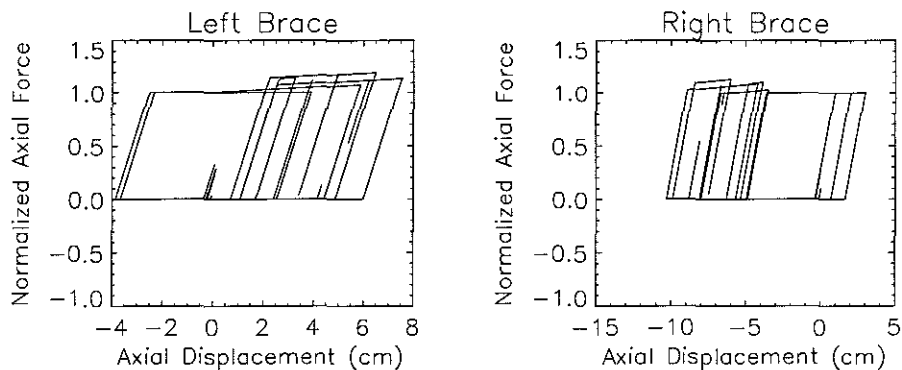


Figure 4.30: Normalized hysteresis loops of the first-story braces of F6SL under the Kobe ground motion.
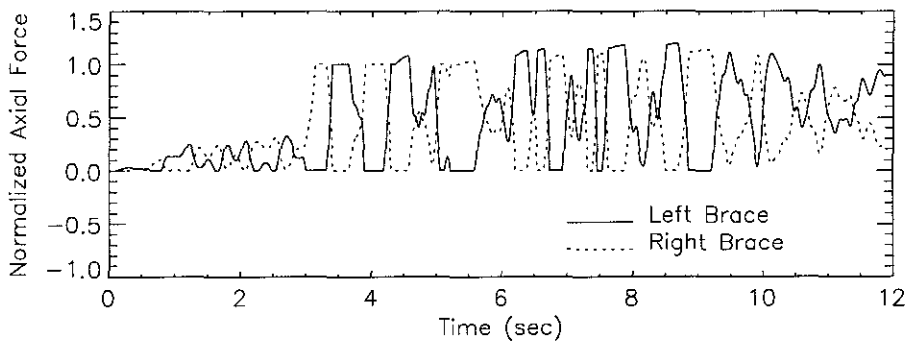


Figure 4.31: Normalized axial force time histories for first-story braces of F6SL under the Kobe ground motion.

As for the overall responses, the plastic energy demand on the non-brace structural components of F6SL is the smallest among the five structures under both the Kobe and Sylmar ground motions, and the non-buckling bracing system dissipates the largest amount of energy, as shown in Figures 4.20 and 4.21. Under the Kobe ground motion, F6SL
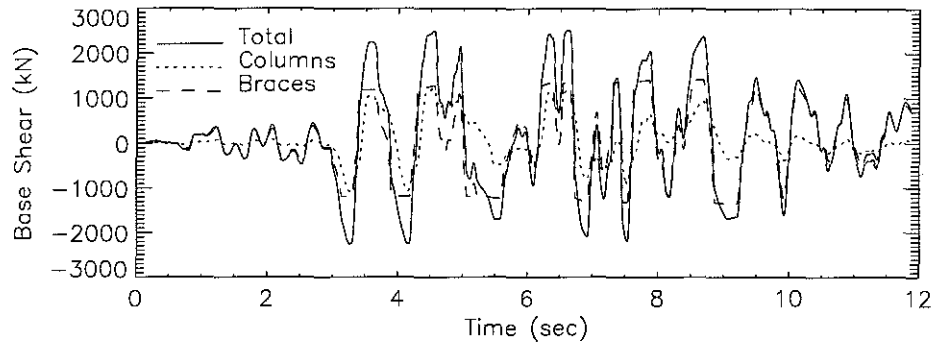
**Figure 4.32**: Base shear time history of F6SL under the Kobe ground motions.
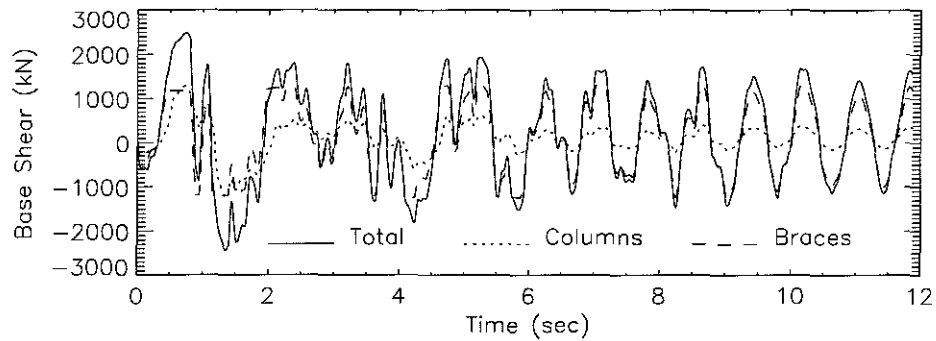


**Figure 4.33**: Base shear time history of F6SL under the Sylmar ground motion.

also has the smallest peak floor lateral displacement and peak story drift, as shown in Figures 4.22, 4.23 and 4.25.

In terms of peak responses, F6SL shows more advantage over structures with a conventional bracing system under the Kobe ground motion than under the Sylmar ground motion (Figures 4.22, 4.24 and 4.24). One reason for this is that, under the Sylmar ground motion, the peak response occurs early in the first cycle before the bracing systems experience any significant deterioration, and after that the intensity of the response drops off quickly, and therefore the difference between the deterioration resistance of the non-buckling bracing system and the conventional bracing systems can not be differentiated. In contrast, under the Kobe ground motion, the response of the structures maintains a high intensity level of
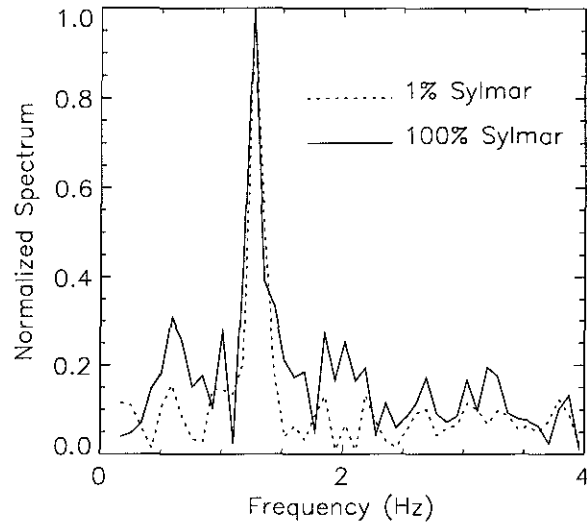
(a) Under Sylmar record
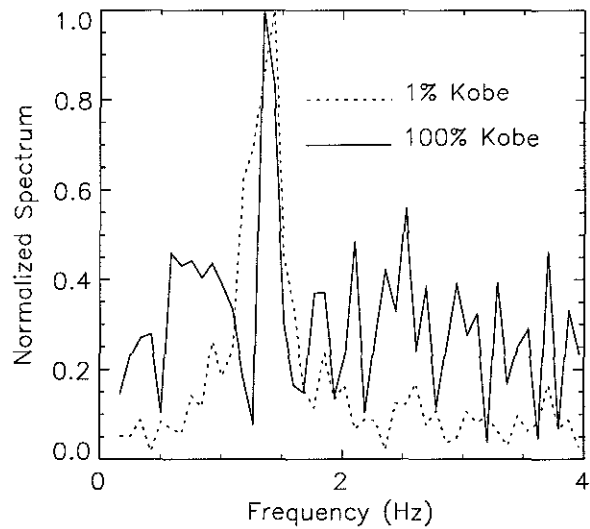


(b) Under Kobe record

**Figure 4.34**: Roof lateral velocity spectrum of F6SL under ground motions of different intensities. The predominant frequency of the response shifts lower when the structure is subjected to large amplitude ground motions.

vibrations for a relatively long period, thus allowing the superior deterioration-resistance of the non-buckling bracing system to stand out. The result is more differentiated peak response quantities for structures with different bracing systems. Another reason is that a slip brace can resist only tensile force, and therefore the virgin strength of F6SL is lower than the other structures with conventional bracing systems. The energy dissipation is dependent on the entire response history, and therefore the non-buckling bracing system shows advantage over other bracing systems under both ground motions.

The shift of the predominant frequency in the response spectrum of F6SL is extremely small, as can be seen in Figure 4.34 on the page before. Although this structure also experiences significant plastic yielding under the unscaled Sylmar record, the frequency shift is minimal, a result of the more stable hysteretic characteristics. Judging from this fact, it can be concluded that the frequency shift in the responses of the other four structures is mainly the consequence of the deterioration of the bracing systems.

### 4.4.4 Effect of Input Frequency Content

As mentioned above, because of the difference in the natural frequencies of structures with different bracing systems, the frequency content of the ground motion inputs may affect the comparison. To reduce this effect, this section uses several ground motions with different frequency content in the comparison. Two of the five structures, F6CX and F6SL, are selected for this purpose. The ground motions are derived from the Kobe acceleration record through temporal and amplitude scaling as described in Appendix B to achieve desired frequency content and intensity.

The issue concerning the choosing of suitable ground motions input arises from the fact that different bracing systems give the structure different natural frequencies and thus different frequency response characteristics. This makes it difficult to determine whether the difference in responses of two structures with different bracing systems is the result of different natural frequencies or of differences in other qualities like deterioration resistance and energy dissipation capacity. This distinction is important because the reduction of re-

sponses caused by the change of natural frequencies is beneficial only in the case where the frequency content of possible ground motion is known, while the reduction caused by increased deterioration resistance and energy dissipation is beneficial in all cases and is therefore more desirable. In an attempt to differentiate these two effects, a series of scaled ground motions have been used in the study. Details of the scaling are discussed in Appendix B on page 151. The range of the temporal scaling factor $\lambda$ considered is between 0.6 and 2.0, with an increment of 0.2 and an $\eta = 0.8$ in Equation B.5 on page 157.
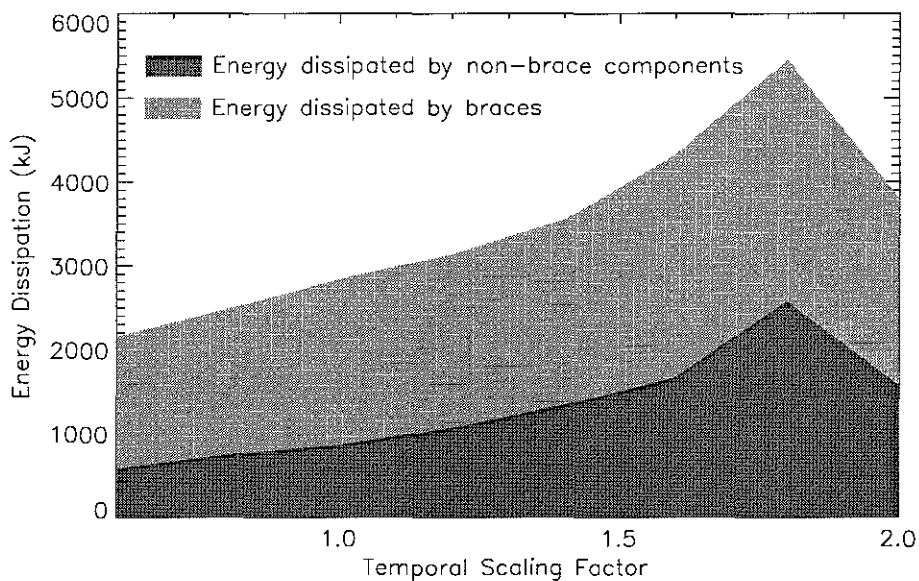


**Figure 4.35**: Energy dissipation by braces and non-brace structural components of F6CX under the scaled Kobe ground motions.

The frequency content of ground motion inputs has significant effect on the response of the two structures. However over the range of temporal scaling factor considered, F6SL consistently shows better performance over F6CX. Figures 4.35 and 4.36 plot the energy dissipation by the bracing system and non-brace structural components for F6CX and F6SL under the scaled Kobe ground motions. It is seen that the energy demand on the non-brace structural components in F6SL is considerably lower than that on the same components in F6CX for the entire range of temporal scaling. The peak roof displacement (Figure 4.37), the maximum peak story drift (Figure 4.38) and the average peak story drift (Figure 4.39)
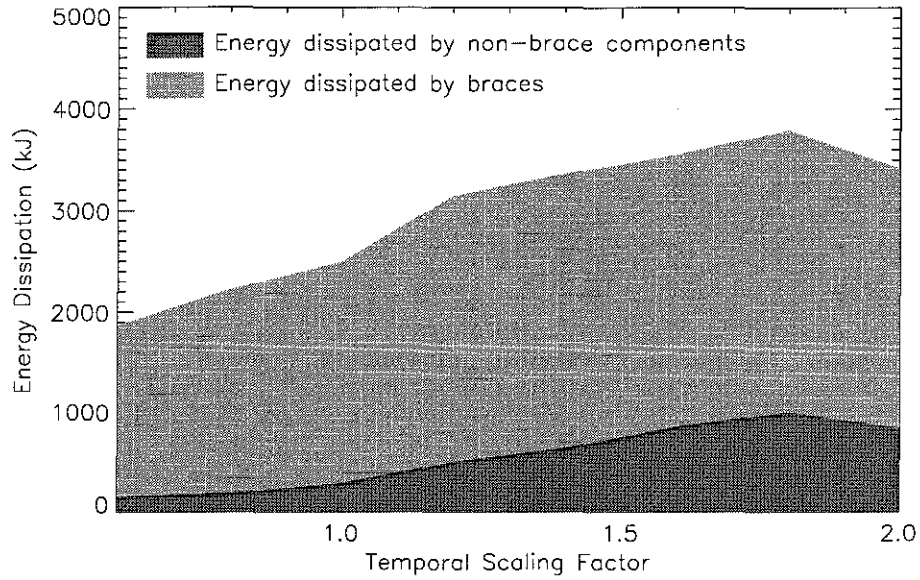
**Figure 4.36**: Energy dissipation by braces and non-brace structural components of F6SL under the scaled Kobe ground motions.
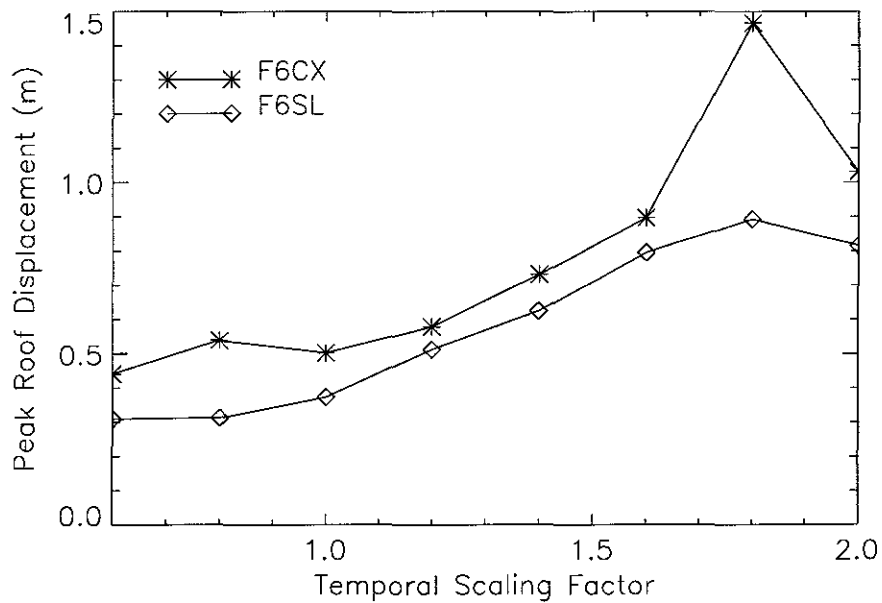


**Figure 4.37**: Peak lateral roof displacement for F6CX and F6SL under the scaled Kobe ground motions.
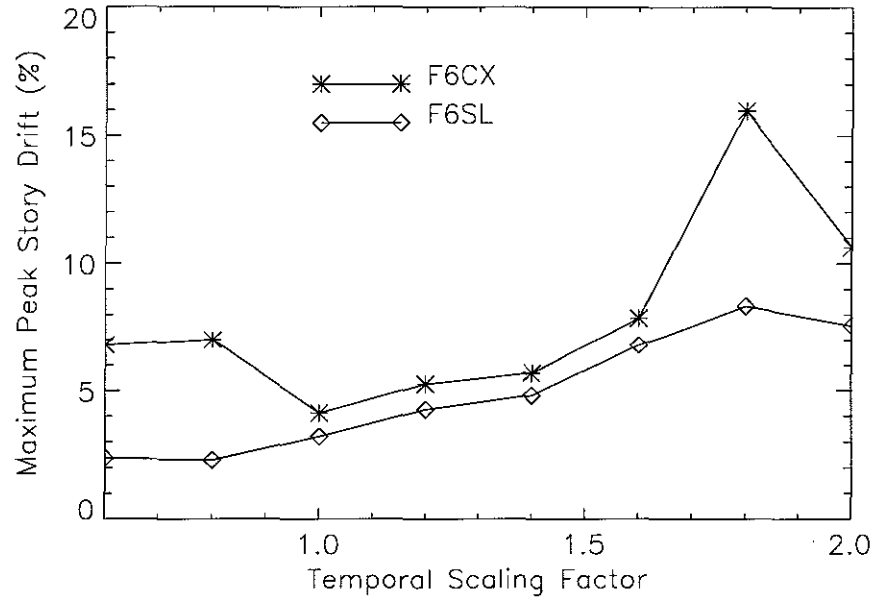
**Figure 4.38**: Maximum peak story drift of F6CX and F6SL under the scaled Kobe ground motions.
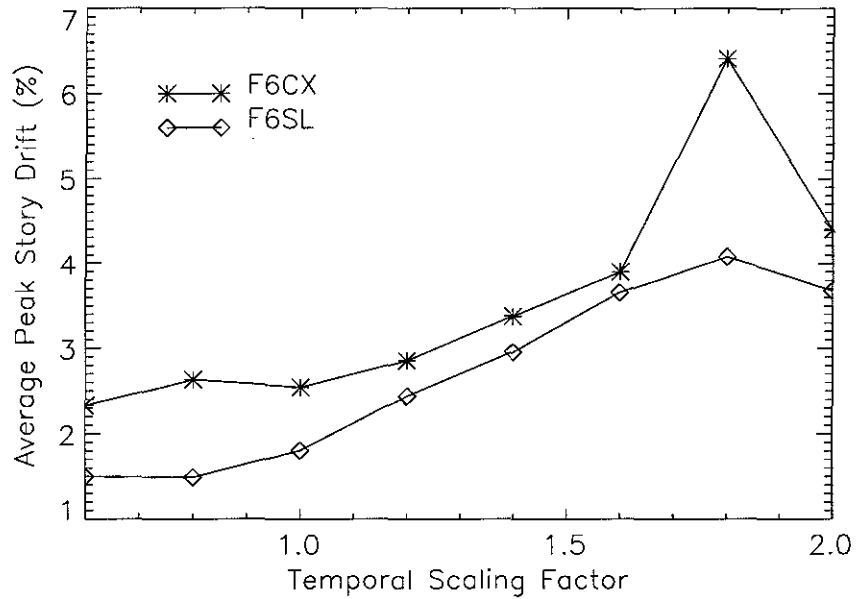


**Figure 4.39**: Average peak story drift of F6CX and F6SL under the scaled Kobe ground motions.

of F6SL are also consistently smaller than those of F6CV for the range of temporal scaling factor.

Question concerning of the propriety of using the virgin strength of the braces in the design is also echoed by the results in this chapter. Although the push-over result in Figure 4.6 on page 102 show that the structures have adequate strength, but the response levels under the Sylmar and Kobe ground motions are unacceptably high.

## 4.5 Conclusions

The effects of different bracing systems on the response of braced structures have been studied. The following conclusions are made:

1. Under small amplitude vibrations, the bracing system provides the main portion of the lateral stiffness of the structures and resists most of the lateral shear force. But after the buckling of the braces, redistribution of base shear occurs and the columns carry significantly more of the shear force.

2. The unbalanced vertical force resulting from brace buckling in a chevron bracing system can cause severe bending of the beam to which the braces are connected. This also reduces the effectiveness of the bracing system significantly and causes severe compression of the braces. X-bracing can alleviate this problem and result in better bracing performance. The response of structures with X-bracing is less severe than that of structures with chevron bracing.

3. A bracing system with clamp-ended braces has better force resistance and energy dissipation capacities, leading to smaller response, than one with a pin-ended bracing system.

4. The non-buckling bracing system provides good lateral shear resistance through-out the entire time history because of its stable hysteretic characteristic. The response of the structure with a non-buckling bracing system is considerably smaller than other

structures with a conventional bracing system under ground motions with several significant cycles. The non-buckling bracing system is especially effective in reducing the plastic energy demand on the non-brace structural components. This is true for ground motions with a wide range of frequency content. However, for ground motion input whose main energy is concentrated in one cycle, as in the case of the Sylmar record, the non-buckling bracing system shows less advantage over the conventional bracing systems.

5. The combination of X-bracing and clamped-clamped end condition give the best bracing performance for the conventional bracing systems considered in this study.

# Chapter 5

# Summary and Conclusions

This thesis examines the earthquake behaviors of steel bracing members and braced steel frames. A summary of the subjects under consideration and the main conclusions is presented in the following.

## 5.1 Braces Under Cyclic End Displacement

### 5.1.1 Inertia Effect

Braces under axial compression belong to a class of "acceleration magnifying" structural elements in which small motion at the loading point can result in large internal acceleration and hence large inertia. This phenomenon has direct effect on the validity of the numerical and pseudo-dynamic modeling of braced structures under dynamic loading. In numerical analysis, a technique called static condensation is commonly used to remove the internal degrees of freedom of a brace from the global equations. In pseudo-dynamic modeling, the internal dynamics of the braces is routinely ignored because of the limited number of data channels and actuators. How these simplifications affect the accuracy of modeling is the focus of Chapter 2, which studies the effect of internal inertia on the response of individual braces under cyclic end displacement typical of earthquake response of steel frames. The study uses a fiber type finite element beam-column model.

The effect of internal inertia is found to depend on several factors, of which the most important are the period of the end displacement input and the slenderness ratio of the braces. For slender braces, the most pronounced effect of the period is on the axial force response.

Inputs of short period produce higher axial force response. For braces with a slenderness ratio greater than 100, an input with period shorter than 0.8 seconds can result in significant increase in the peak axial force compared with the value predicted by quasi-static analysis. Very short input periods (about 0.2 seconds) also cause significant increase in the compressive strain for braces with slenderness ratio over 100.

For stocky braces, the effect of inertia is more visible on the deformation patterns than on the magnitude of axial force and strain. End displacement inputs with short period can cause unsymmetrical deformation in the braces similar to the unsymmetrical buckling of shallow arches under distributed lateral force. This unintuitive deformation mode is fundamentally different from what can be predicted by quasi-static analysis.

From the results it is concluded that, for braces similar to those considered in this thesis, if the period of the input is longer than 0.8 seconds, the effect of internal inertia can be ignored and the static condensation technique can be applied to the internal degrees of freedom. For input with period less than 0.5 seconds, the peak axial force can be significantly higher than the value predicted by quasi-static method. It is suggested that a full-blown dynamic analysis be carried out whenever possible. If this is not practical, localized measure should be considered to account for the effect of increased brace force on the adjacent structural components. The increase in the axial force takes the form of disturbance with frequencies much higher than the normal range found in building structures. Its effect on the overall response of a structure under earthquake ground motions is not clear, and the need for further research exists. Besides its implication in the numerical and pseudo-dynamic modeling of structures under earthquake ground motions, this part of the study can also have significance in the response of structures under blast and impact loads.

## 5.1.2   Brace Deformation

Local buckling and cracking, together with connection damage, are the primary modes of brace failure. Large compressive axial deformation is the cause of local buckling, which in turn leads to strain concentration and cracking. Chapter 2 also studies the deformation of

braces of different sizes and end conditions under monotonic and cyclic end displacement.

The distribution of axial strain over the length of a brace under axial end displacement is highly uneven, and strain concentration occurs. The maximum strain can be several times the equivalent uniform strain. The size of a brace affects its strain distribution and magnitude. Slender braces often have more severe strain concentration, but stocky braces have higher strain magnitude under the same end displacement. The strain resulting from cyclic end displacement is higher than that from monotonic end displacement of identical magnitude.

## 5.2   Braced Steel Frames With Column Uplift

Recent earthquake events have demonstrated the large magnitude of axial force in braced bay columns and the difficulty in properly anchoring the column bases. Chapter 3 of this thesis examines the effect of column uplift and explores the feasibility of flexible column base anchoring. A 6-bay and 4-story frame structure with one strong braced bay is designed for this purpose.

The study finds that free column uplift can seriously reduce the lateral force resistance of the frame and result in large story drift. The pounding of an uplifted column with its base also significantly increases the compressive axial force in the column. Flexible non-pounding column base anchoring can reduce the force in the braced bay columns and braces, but can result in story drift too large to be acceptable. The results show that using strong braces in a small number of bays poses serious difficulty in the design of columns and column base anchoring.

## 5.3   Non-Buckling Bracing System

Chapter 2 shows that slender braces are susceptible to deterioration, while, on the other hand, Chapter 3 and experience from past earthquakes show that using strong braces can

result in large braced bay member force and increase the likelihood of failures in the braced bay members and their connections. Since buckling is the cause for brace deterioration, a non-buckling bracing system is proposed in Chapter 4 in an attempt to solve this dilemma. The proposed bracing system eliminates the possibility of buckling, and thus can be used with small braces distributed in more bays without increasing the susceptibility of deterioration.

The effectiveness of this bracing system is assessed by comparing the responses of a 6-story frame building braced by different bracing systems under artificial and recorded earthquake ground motions. This study does not deal with the implementation of the bracing system. Instead, the goal of the study at this stage is to demonstrate the potential of the non-buckling bracing system, and hopefully, to stimulate further research in this area. The results show that the proposed bracing system can significantly reduce the response of the structure compared with conventional bracing systems.

The effectiveness of conventional bracing systems with different brace configurations and end conditions are also studied. The results show that, in a frame with a Chevron bracing system, the unbalanced vertical force resulting from brace buckling can cause severe bending in beams to which the bracing members are attached. In return, the severe bending of the beam also reduces the effectiveness of the bracing system. Bracing systems with clamped brace ends generally show more effectiveness.

The results from ground motions recorded during the Northridge and Kobe earthquakes raise questions regarding the adequacy of code-designed conventionally braced frames. Extremely large story drifts are observed in these frames under the two ground motion records. The exact reason for this is not clear. Low strength reserve in the frames after brace buckling occurs is one possible reason that merits further study.

# Appendix A

# Notes on Modeling and Programming

## A.1 Equation of Motion

The dynamic response of a structure is obtained by solving its equation of motion. For complex nonlinear structures this is usually possible only in discrete form through numerical iteration. This is the approach used through out the studies of this thesis. After spatial discretization, the equation of motion for a structure can be written

$$[M]\{\ddot{d}(t)\} + [C]\{\dot{d}(t)\} + \{R(t)\} = \{f(t)\} \tag{A.1}$$

where $[M]$ is the mass matrix, $[C]$ the linear viscous damping matrix, $\{R(t)\}$ the static resisting force vector corresponding to the displacement vector $\{d(t)\}$, and $\{f(t)\}$ the load vector which includes the gravity and earthquake loads. $\{f(t)\}$ can be expressed as

$$\{f(t)\} = -[M]\{I\}a(t) + \{F\} \tag{A.2}$$

where $\{a(y)\}$ is the ground acceleration, $\{I\}$ the participation vector, and $\{F\}$ the gravity load vector.

## A.2 Mass Matrix

The mass of the structures is lumped at the nodes, which usually mean the beam-to-column junctions in a frame structure. Because of the complexity of three dimensional structures,

they are simplified into planar frames in this study. In some cases all or part of the inner columns of a building are designed to only carry vertical load. Under such situation the mass that participates in horizontal acceleration is usually different from the mass that participates in the vertical acceleration in the two dimensional model.

## A.3 Stiffness Matrix

The resisting force vector $\{R(t)\}$ is generally a nonlinear function of displacement vector $\{d(t)\}$ and depends on the deformation history in the existence of inelastic deformation. Because of this, linearization and iterations during each time step are necessary to integrate the equation of motion. In the vicinity of a current approximation $\{d\}$ of the displacements vector at time $t + \Delta t$, the resisting force vector can be expressed approximately by the equation

$$\{R(t + \Delta t)\} = [K_{\mathrm{T}}]\{\Delta d\} + \{R\} \tag{A.3}$$

where $[K_{\mathrm{T}}] = \nabla_{\{d\}}\{R(t + \Delta t)\}$ is the tangent stiffness matrix, $\{\Delta d\}$ the displacement increment, and $\{R\}$ the resisting force vector corresponding to $\{d\}$.

## A.4 Damping Matrix

For linear structures, the damping matrix $[C]$ is commonly expressed as various forms of combination of the mass matrix $[M]$ and the stiffness matrix $[K]$, among which the following form is most frequently used

$$[C] = \alpha_0[M] + \alpha_1[K] \tag{A.4}$$

where $\alpha_0$ and $\alpha_1$ are chosen to give the system the desired level of damping. One obvious advantage of such an expression of $[C]$ is that it allows the system to have classical modes and thus can be un-coupled with the undamped modal matrix [29], making classical

modal analysis possible. The expression also easily relates the coefficients $\alpha_0$ and $\alpha_1$ to the modal damping ratio $\zeta$, whose measuring is widely conducted in dynamic structural testings, through the equation

$$\zeta = \frac{1}{2\omega}(\alpha_0 + \alpha_1\omega^2) \qquad (A.5)$$

where $\omega$ is the frequency of vibrations in radians/sec. Many structures do have un-coupled modes during small amplitude vibrations. If the value of $\zeta$ is given at two different frequencies $\omega_1$ and $\omega_2$, then $\alpha_0$ and $\alpha_1$ can be determined from

$$\alpha_0 = \zeta\frac{2\omega_1\omega_2}{\omega_1 + \omega_2}, \qquad \alpha_1 = \zeta\frac{2}{\omega_1 + \omega_2}. \qquad (A.6)$$

It is noted from Equation A.5 that the damping ratios for different modes can be different. Only at frequencies $\omega_1$ and $\omega_2$ does the damping ratio equal to the desired value. For frequencies in the range between $\omega_1$ and $\omega_2$ the damping ratio is lower than the desired value, resulting in under-damped modes; for frequencies outside of the above range the damping ratio is higher than the desired value, resulting in over-damped modes.

In modal analysis of linear systems, the matrix $[C]$ can simply be ignored and damping ratios are assigned to individual modes directly. But this is not possible in direct integration of nonlinear structures. One solution is to include more terms from the Caughey series in the expression of $[C]$. This will still guarantee the existence of the classical normal modes of the system. Other methods call for the use of more complicated functions of the components in $[M]$ and $[K]$ and do not guarantee the existence of the classical normal modes. The computation work is likely to increase with these methods.

There is an additional difficulty when nonlinear structures are the concern. All the above expressions of the damping matrix call for the use of the stiffness matrix in one way or another. For a nonlinear structure the stiffness matrix is no longer constant, and theoretically the stiffness of some of the structural components can go down to near zero. Under this situation the use of the initial stiffness matrix in Equation A.4 can result in artificially large viscous damping energy dissipation because the weakened components will experience more

severe deformation and the viscous damping energy dissipation is proportional to the deformation and the stiffness which does not reflect the change.

One extreme example is when modeling brittle damage of certain structural components with high stiffness. Because of its high stiffness, the damping coefficients associated with this type of components are large. This is not a serious problem before a component is damaged since the deformation in the components is small. But once the component experiences brittle damage, the stiffness provided by the components drops to zero and large relative displacement may result. But since $[C]$ is constant, it does not reflect the change in stiffness associated with the damaged components, and dissipates undue amount of energy because of the large relative displacement.

The situation with braces is similar. The linear stiffness associated with a brace is very large compared with other components. But when it buckles or yields there is a steep drop in its stiffness and thus allows large relative displacement between its two ends, resulting in abnormal energy dissipation through damping coefficient term. It should be noted that the energy thus dissipated is in addition to the energy dissipated through plastic deformation.

To correct this problem the use of a damping matrix that will take into account of the changing stiffness is desirable. One way to do this is to use the current tangent stiffness matrix. If the components that are likely experience significant plastic deformation can be identified prior the start of computation, the contribution to the damping matrix by these components can be removed from $[C]$. This treatment causes some inconsistency in the damping ratios of the system. But it is not expected to cause significant error to the solution, especially for responses under strong ground motions since the viscous damping effect plays only a small role compared with the hysteretic damping effect associated with plastic deformation.

In this study the damping of a structure is considered in two parts: viscous damping and hysteretic damping. The viscous damping can be interpreted as the damping that is measured in small amplitude vibration testing, while the hysteretic damping is determined by the hysteretic characteristics of the force term $R\{t\}$ in Equation A.1. The stiffness of all

braces and panel zones, which are particularly easy to yield, is not included in $[C]$ to avoid excessive energy dissipation by these components when they experience yielding or buckling. Since the studies are primarily interested in the nonlinear response of frame structures under strong earthquake, the hysteretic damping term dominates and the above approximation is expected to have only small effect.

## A.5   Integration of The Motion Equation

Substitution of Equation A.3 into Equation A.1 and discretization in time domain using constant average acceleration method give

$$
\begin{aligned}
\left[ M + \frac{\Delta t}{2}C + \frac{\Delta t^2}{4}K_{\mathrm{T}} \right] \{\Delta d\} &= \frac{\Delta t^2}{4}\{f(t + \Delta t)\} - \left[ M + \frac{\Delta t}{2}C \right] \{d(t)\} \\
&\quad - \frac{\Delta t^2}{4}\{R(t)\} + [M]\left\{ d(t) + \Delta t\, \dot{d}(t) + \frac{\Delta t^2}{4}\ddot{d}(t) \right\} \\
&\quad + [C]\left\{ \frac{\Delta t}{2}a(t) + \frac{\Delta t^2}{4}\dot{d}(t) \right\}
\end{aligned}
\tag{A.7}
$$

which is then solved iteratively for $\{\Delta d\}$ at each time step. There are a few details that call for special attentions in the iteration process.

One problem is associated with the irreversibility of plastic deformation: Unlike the energy stored in the form of elastic potential, the energy dissipated in plastic deformation will never be returned to the system in other form of energy. In the iterative solution process it is inevitable that some iterations will over-shoot the target deformation state. Even though the iteration mechanism will try to retreat from the over-shot state, it can never arrive at the real target since the energy dissipation that is realized in the over-shot is irreversible. This problem is also frequently described in the perspective of artificial unloading [26].

To avoid this problem, an iteration scheme [10] in which each iteration within a time step is based on the deformation state at the beginning of the time step is used. According

to this scheme, the displacement vector at time $t + \Delta t$ for iteration $k + 1$ is expressed as

$$\{d^{k+1}(t + \Delta t)\} = d(t) + \{\Delta a^k\} \qquad \text{(A.8)}$$

where $\{d(t)\}$ is the displacement vector at the beginning of the time step, and $\{\Delta a^k\}$ is the displacement increment vector from $\{d(t)\}$. The plastic energy dissipation within the time step depends only on the beginning state and the final state, thus avoiding the artificial energy dissipation during the iterations.

Numerical experiment shows that in many cases the use of tangent stiffness in the iteration can speed up convergence significantly. But there are times when the use of the elastic stiffness is prefered or necessary. One such case is in the first iteration of each step. This is necessary to trace the correct load-deformation path when the deformation direction change from loading to unloading. It may also help to switch to the elastic stiffness when the iterations are not showing convergence. Another situation in which the use of the elastic stiffness matrix may be helpful is when the left hand side matrix of the iteration equation becomes non-positive definite because of large axial force and small material stiffness.

The program uses a two-level iteration scheme in which the internal degrees of freedom of some of the members are statically condensed and only the boundary degrees of freedom enter the global displacement vector. After each global iteration, the global nodal displacements are imposed on the condensed components; the internal forces and nodal displacements of the members are then computed by iterations at the member level. The resulting imbalance nodal forces enter the next global iteration until the desired accuracy is achieved.

## A.6 Fiber Element

Beams, columns and braces are modeled by fiber elements [10]. In this model, an undeformed member is divided into a number of segments by node planes perpendicular to the longitudinal axis of the member, as is shown in Figure A.1(a). A node plane is assumed to remain a plane, but not necessarily perpendicular to the longitudinal axis, after deformation.

Each segment is further divided into a number of strips over the cross-section, as illustrated in Figure A.1(b) for an I-shaped cross-section. The strips are then replaced by abstract uniaxial fibers at the centroid of the strips. These fibers are connected to the two node planes of the segment but are otherwise independent to each other, as shown in Figure A.1(c). The deformation of the fibers in a segment is entirely determined by the translational and rotational displacements of the two node planes at the ends of the segment.

(a) Subsegments

(b) Strips

Fiber —⟋   Node plane —⟍
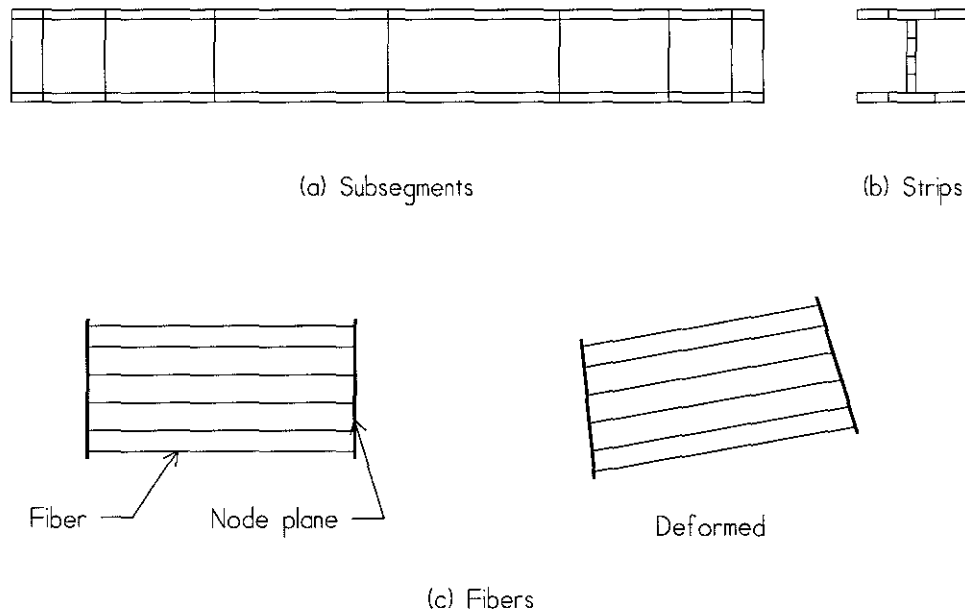
Deformed

(c) Fibers

**Figure A.1**: Fiber modeling of a W-shape structural member. (a) The member is divided into a number of subsegments. (b) The cross-section is divided into a number of strips. (c) The strips are represented by fibers.

The stress for a fiber under a given deformation history is determined by a hysteretic model detailed in [11]. The basis of the hysteretic model is the monotonic loading curve, which is defined by the elastic modulus $E$, yield stress $\sigma_y$, ultimate stress $\sigma_u$, strain $\epsilon_{sh}$ at initiation of strain hardening, strain $\epsilon_u$ at ultimate stress, rupture strain $\epsilon_r$, and initial strain hardening modulus $E_{sh}$, as shown in Figure A.2. The monotonic loading curve is assumed to apply in both tension and compression.

When no unloading is involved, the determination of stress amounts simply to following the monotonic loading curve. When the stress-strain history involves unloading, the determination of stress makes use of two backbone curves and a set of rules. The two back-

bone curves, one for tensile stress state and the other for compressive stress state, have the same shape as the monotonic curve but they shift along the strain axis. Details on the rules to trace the hysteretic stress-strain path can be found in [10].

Given the current stresses of the fibers, the resultant nodal axial force $P$ and moments $M_1$ and $M_2$ for the segment are computed as

$$P = \sum_{i=1}^{N_f} \sigma_i A_i \tag{A.9}$$

$$M_1 = -\sum_{i=1}^{N_f} \sigma_i A_i h_i + \frac{1}{2} Ql \tag{A.10}$$

$$M_2 = \sum_{i=1}^{N_f} \sigma_i A_i h_i + \frac{1}{2} Ql \tag{A.11}$$

where $N_f$ is the number of fibers, $\sigma_i$ the stress in the $i$-th fiber, $A_i$ the cross-sectional area of the strip represented by the fiber, $h_i$ the distance of the fiber from the centroid of the segment's cross section, $l$ the length of the segment, and $Q$ the shear force. The shear force is assumed to be carried by the material in the segment elastically and is calculated from

$$Q = \frac{1}{2} GA^* \gamma \tag{A.12}$$

where $\gamma$ and $A^*$ are the average shear deformation and the effective shear area of the segment, respectively. The inclusion of the term $Ql/2$ in the formulas for $M_1$ and $M_2$ is necessary because the summation term is more appropriately interpreted as the moment at the mid-point of the segment.

The computation of the segment tangent stiffness matrix, which relates nodal displacement increments to nodal force increments, follows the regular finite element procedure. Under local coordinates, the tangent stiffness

$$[K] = [K_F] + [K_{SH}] \tag{A.13}$$
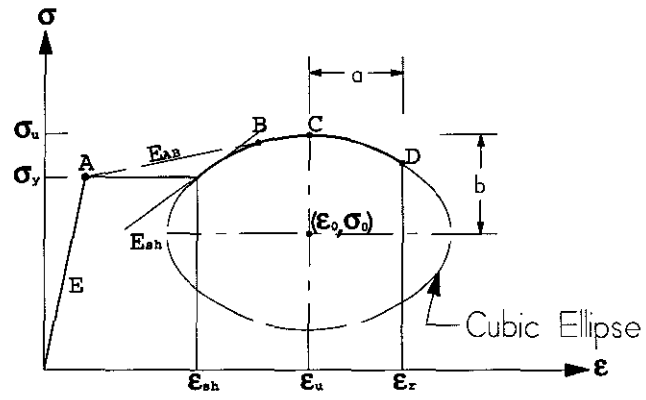
**Figure A.2**: Monotonic stress-strain loading curve for fiber model [11].
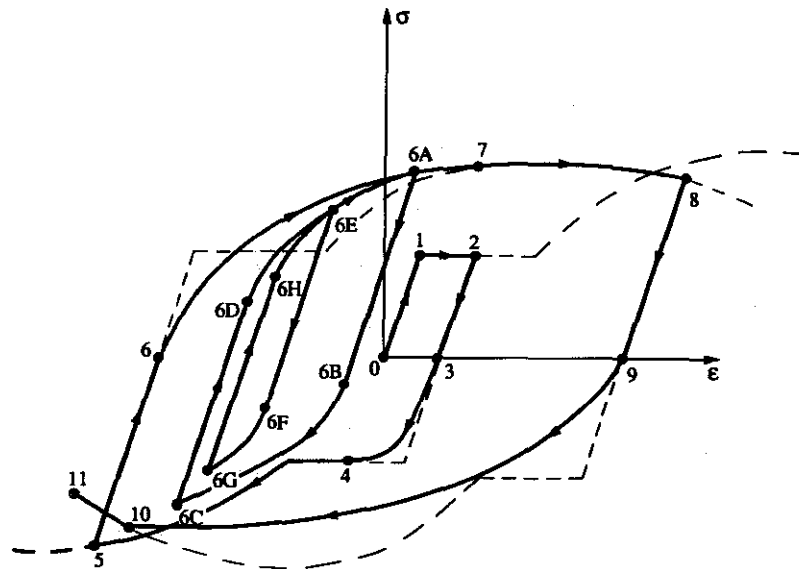


**Figure A.3**: Hysteretic stress-strain behavior for the fiber model [11].

where $[K_F]$ represents the contribution from material and geometric stiffnesses of the fibers, and $[K_{SH}]$ the shear stiffness:

$$[K_F] = \sum_{i=1}^{N_f} \begin{bmatrix} \Lambda_i & -\Lambda_i \\ -\Lambda_i & \Lambda_i \end{bmatrix}, \qquad [\Lambda_i] = \frac{A_i}{l} \begin{bmatrix} E_{Ti} & 0 & -E_{Ti}h_i \\ 0 & \sigma_i & 0 \\ -E_{Ti}h_i & 0 & E_{Ti}h_i^2 \end{bmatrix} \qquad (A.14)$$

$$[K_{SH}] = GA^* \begin{bmatrix} 0 & 0 & 0 & 0 & 0 & 0 \\ & 1/l & -1/2 & 0 & -1/l & -1/2 \\ & & l/4 & 0 & 1/2 & l/4 \\ & & & 0 & 0 & 0 \\ & \text{sym} & & & 1/l & 1/2 \\ & & & & & l/4 \end{bmatrix}. \qquad (A.15)$$

The element stiffness matrix is then transformed from local coordinate system into global coordinate system and is then assembled into the global stiffness matrix.

The computation associated with the fiber element model is quite CPU intensive when there is yielding or buckling in the elements. To improve the computational efficiency, the internal degrees of freedom are statically condensed and only the degrees of freedom of the two ends of a component enter the global equilibrium equation of the structure. This greatly reduces the total number of degrees of freedom of the structure and thus improves computational efficiency.

Numerical results [10] show that the fiber element, with its ability to include strain hardening, gradual spread of yield area, axial-flexural yield interaction, is able to model some of the difficult problems like cyclic elasto-plastic buckling of steel columns with good accuracy. For beams and columns the use of 7 to 8 subsegments gives satisfactory accuracy.

# A.7  Panel Zone Element

Common methods of beam-to-column connection in steel frame structures include welds, rivets, unfinished bolts, and high-strength bolts. This thesis is concerned with the type of welded joints that in engineering practice are sometimes classified as being rigid, or more precisely, the type of joints whose connections themselves are so rigid that their deformation can be neglected under normal loading condition. Despite of the rigidity of the connections, the beam-to-column joint assemblage can nevertheless exhibit some degree of flexibility under earthquake ground motion.

Research has shown that the deformation of the beam-column joints can have considerable effects on the response of a steel frame structure, and panel zones exhibits stable hysteretic behavior and are excellent means for energy dissipation [35].

The hysteretic behavior of a panel zone is modeled in a similar way as that of a fiber, except that a different monotonic loading curve (between moment $M^{\mathrm{pz}}$ and shear strain $\gamma_{\mathrm{pz}}$) is used [10]. The monotonic moment–shear strain loading curve for the panel zone begins with a linear segment to 0.8 of the yield moment $M_{\mathrm{y}}^{\mathrm{pz}}$:

$$M_{\mathrm{y}}^{\mathrm{pz}} = \tau_{\mathrm{y}} d_{\mathrm{c}} d_{\mathrm{b}} t \qquad (A.16)$$

where $\tau_{\mathrm{y}} = \sigma_{\mathrm{y}}/\sqrt{3}$ is the shear yield stress, $d_{\mathrm{c}}$, $d_{\mathrm{b}}$ and $t$ are the width, height and thickness of the panel zone. Following the linear segment is a quadratic ellipse that is tangent to the preceding linear segment and reaches a zero slope at $\gamma_{\mathrm{u}} = 100\gamma_{\mathrm{y}}$, $M_{\mathrm{u}}^{\mathrm{pz}} = 2.35 M_{\mathrm{y}}^{\mathrm{pz}}$, where $\gamma_{\mathrm{y}}$ is the shear yield strain. The above monotonic loading curve is chosen to match a set of experimental data.

151

# Appendix B

# Earthquake Ground Motions

Several ground motion time histories are used in this thesis. They include the Sylmar Olive View Hospital record from the 1994 Northridge earthquake, the Kobe JMA record from the 1995 Hyogo-Ken Nanbu, Japan earthquake, the Vina del Mar record from the 1985 Central Chile earthquake and the B-1 artificial ground motion time history from [32]. The acceleration time histories and response spectra of these ground motions are plotted in Figures B.1 to B.4.

The Sylmar and Kobe JMA ground motions shown in Figures B.1 and B.2 are each the combination of the two orthogonal horizontal components

$$a(t) = a_{N-S}(t) \cos \theta + a_{E-W}(t) \sin \theta \tag{B.1}$$

where $a_{N-S}(t)$ is the N-S component, $a_{E-W}(t)$ is the E-W component, and $\theta$ is chosen such that the integral

$$E(\theta) = \int_0^T a^2(t)dt \tag{B.2}$$

is maximized, where $T$ is the duration of the ground motion record.

This set of ground motions represent a wide range of intensities, frequency contents and durations. The Kobe JMA record has a very high intensity both in terms peak acceleration and peak response spectrum. The Sylmar record also has a very high peak acceleration, but the peak response spectrum is smaller and the duration of significant ground motions is shorter. In fact significant ground motions in the Sylmar record occur only in two cycles. The duration of significant ground motions of a record affects the degree of deterioration of
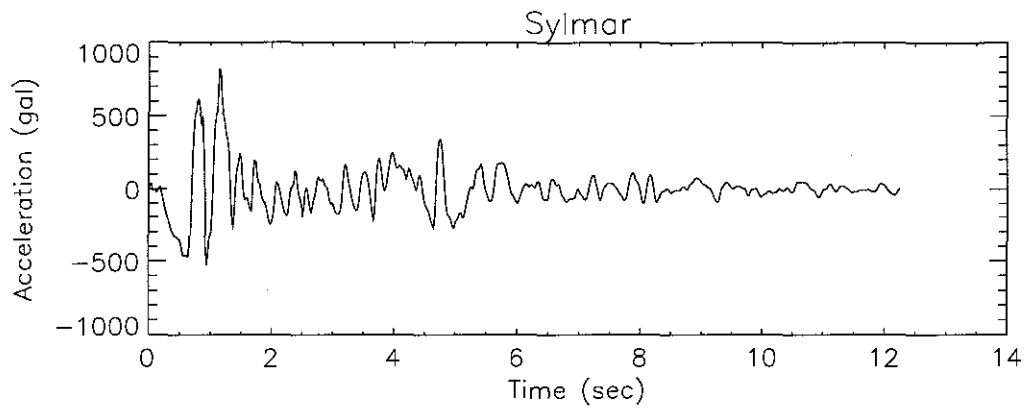
(a) Acceleration
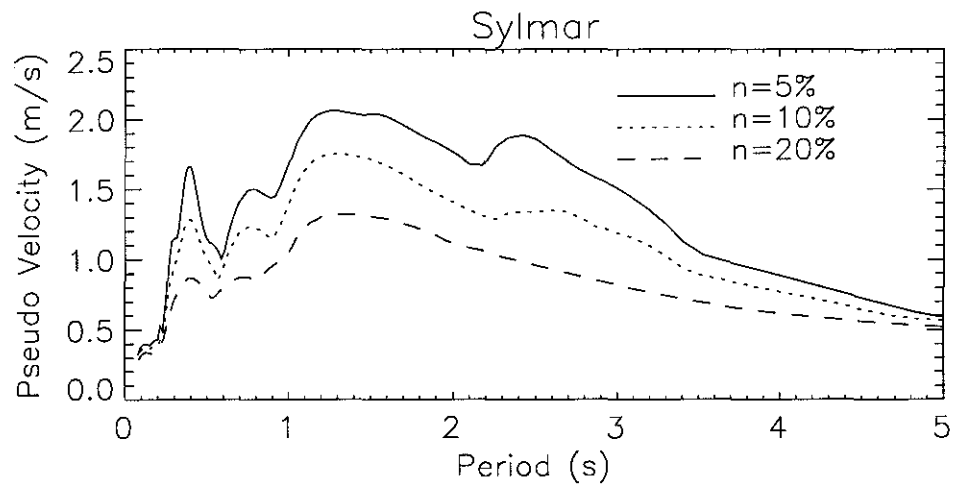


(b) Response spectrum

**Figure B.1**: The Sylmar ground acceleration from the 1994 Northridge earthquake. The record is a combination of the two horizontal acceleration components.
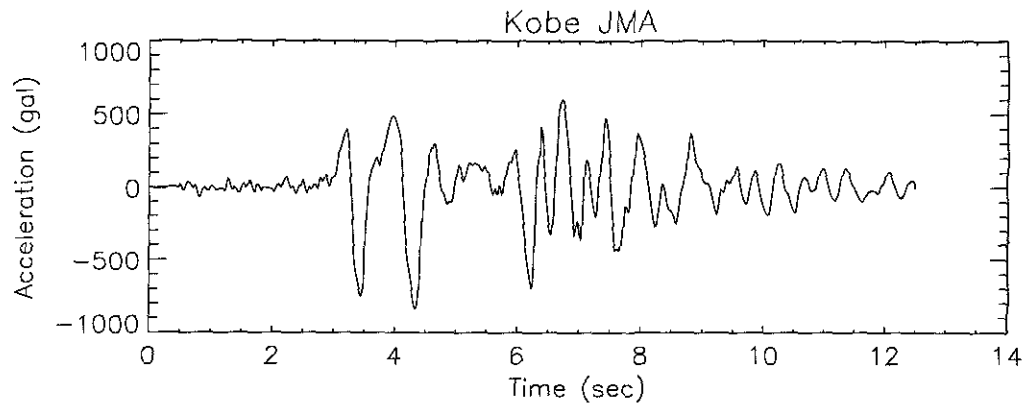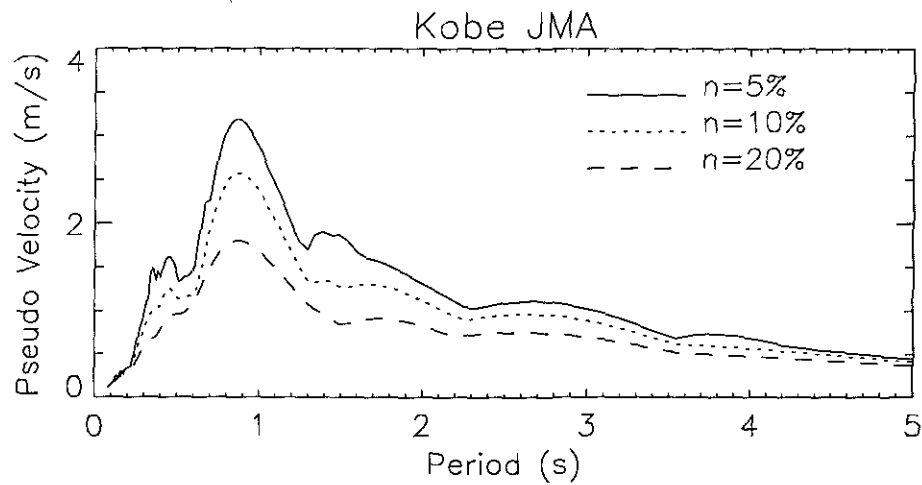
(a) Acceleration



(b) *Response spectrum*

**Figure B.2:** The Kobe JMA ground acceleration from the 1995 Hyogo-Ken Nanbu (Kobe), Japan, earthquake. The record is a combination of the two horizontal acceleration components.
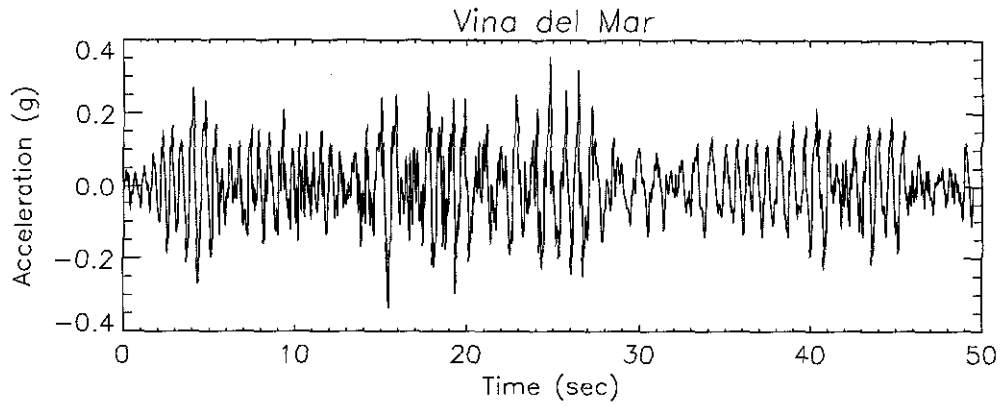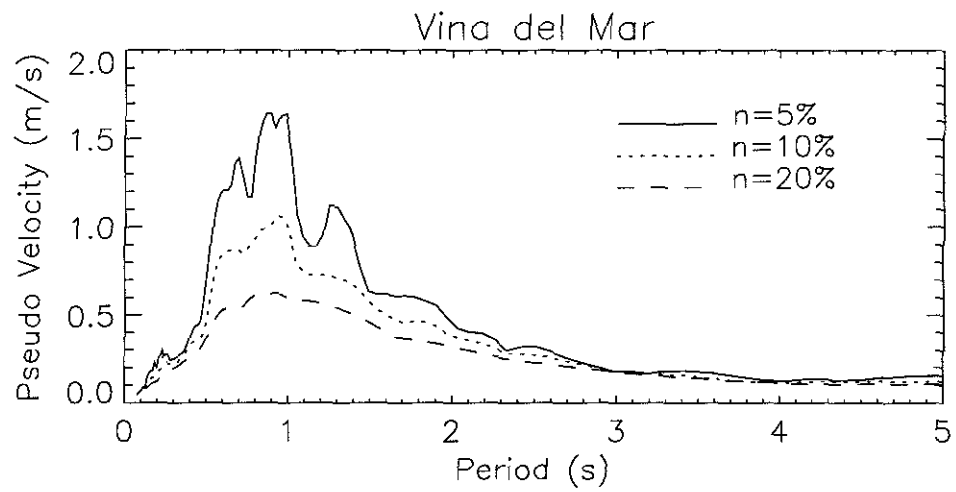
(a) Acceleration



(b) Response spectrum

**Figure B.3**: The Vina del Mar ground acceleration from the 1985 Central Chile earthquake.

(a) Acceleration



(b) Response spectrum

**Figure B.4**: The B-1 artificial ground acceleration from [32].

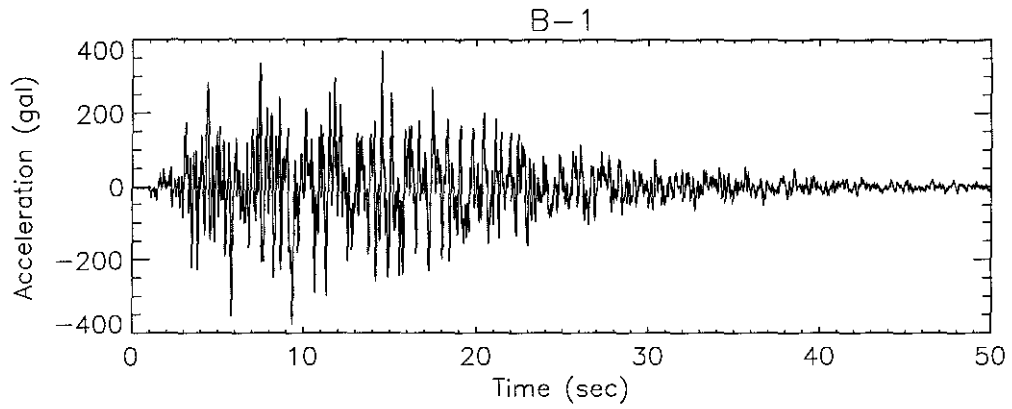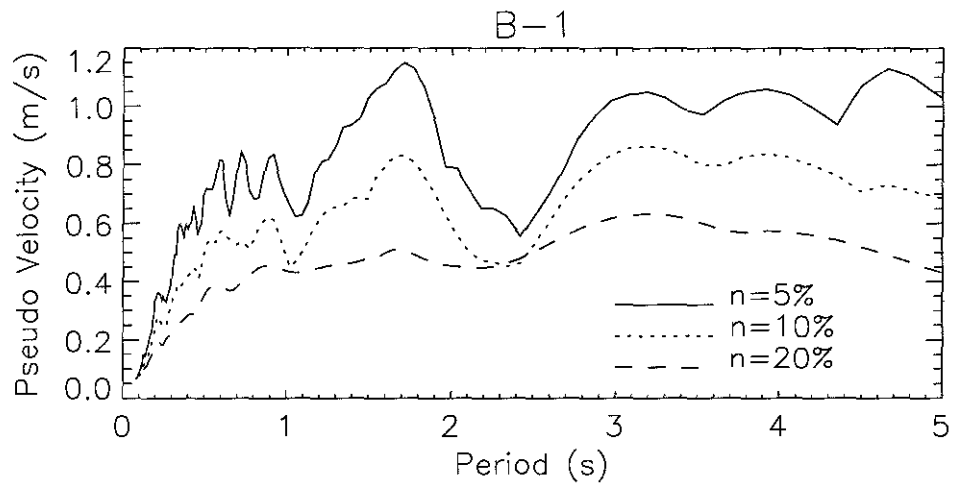the braces in a structure. The Vina del Mar and the B-1 artificial ground motions have relatively long durations of significant ground motions but much smaller intensities in terms of peak acceleration and response spectrum, which are more in line with pre-Northridge estimation of earthquake intensities. The frequency contents of the Kobe JMA record and the Vina del Mar record are largely concentrated around one second period, which is close to the small amplitude natural period of the structures analyzed, but the other two have significant long period content.

The comparison of the earthquake performance of two different structures is invariably affected by the frequency contents of the ground motions used since different structures are likely to have different frequency characteristics. To reduce this effect, it is desirable to conduct the comparison under ground motions with a wide range of frequency contents. The solution of this thesis is to use scaled ground motions as well as the original ground motions presented above. A ground motion time history can be scaled both in time and in amplitude:

$$a(t, \lambda, \mu) = \mu a_0(t/\lambda), \qquad o \leq t \leq \lambda T \tag{B.3}$$

where $\lambda$ is the temporal scaling factor, $\mu$ is the amplitude scaling factor, and $a_0(t)$, $0 \leq t \leq T$, is the un-scaled ground motion. The effects of the scaling factors can be seen more clearly from the Fourier transform of $a(t, \lambda, \mu)$:

$$
\begin{aligned}
A(\omega, \lambda, \mu) &= \int_0^{\lambda T} a(t, \lambda, \mu) \, e^{-j\omega t} dt \\
&= \int_0^{\lambda T} \mu a_0(t/\lambda) \, e^{-j\omega t} dt \\
&= \mu \lambda \int_0^T a_0(\tau) \, e^{-j\lambda\omega\tau} d\tau \\
&= \mu\lambda A_0(\lambda\omega) \tag{B.4}
\end{aligned}
$$

where $A_0(\omega)$ is the Fourier transform of $a_0(t)$. From Equation B.4 it is seen that $\lambda$ affects the Fourier transform of $a(t, \lambda, \mu)$ in amplitude as well as in frequency contents, while $\mu$ affects only the amplitude. A $\lambda > 1$ increases the amplitude of the Fourier transform by a

factor of $\lambda$ and shifts the frequency content towards the lower end by the same factor. So both the frequency content and the Fourier transform amplitude of $a(t, \lambda, \mu)$ can be adjusted by choosing appropriate $\lambda$ and $\mu$.

For better comparability, it is desirable to use ground motions that have about the same "intensity." However, the intensity of a ground motion is not a well defined concept and different, sometimes contradicting, definitions have been used. These methods can be divided into three categories [32]:

1. Characterization by peak parameters of time histories;

2. Spectral methods;

3. Energy methods.

Peak parameters of time histories are single-parameter measures based on the maximum ground acceleration, velocity or displacement. Because of the inherent limitation of a one-parameter measure of a complex wave form, methods in this category are not used in this study.

The response spectral methods most commonly used in earthquake engineering are based on the response spectra which have an explicit engineering meaning. The disadvantage is that it is not easy to find a simple relation between the response spectrum of the unscaled ground motion $a_0(t)$ and that of the scaled ground motion $a(t, \lambda, \mu)$ similar to Equation B.4. But since the Fourier spectrum and the response spectrum under low damping are very similar, the Fourier spectrum is adopted as the measures for the intensity of a ground motion in this study. Based on this definition of intensity, it is seen from Equation B.4 that to maintain $\max |A(\omega, \lambda, \mu)| = \eta \max |A_0(\lambda\omega)|$ requires

$$\mu = \eta/\lambda \qquad (B.5)$$

where $\eta$ is the intensity scaling factor.

The "energy" of a ground motion $a_0(t)$, $0 \le t \le T$, in a generalized sense, is defined in the fashion of [32] as

$$W_0(\infty) = \int_0^\infty a_0^2(t)\, dt = \int_0^T a_0^2(t)\, dt. \tag{B.6}$$

According to this definition, the energy of $a_\lambda(t)$, $0 \le t \le \lambda T$, is

$$W(\lambda, \mu, \infty) = \int_0^{\lambda T} \mu^2 a_0^2(t/\lambda)\, dt = \lambda \mu^2 \int_0^T g_0^2(\tau)\, d\tau. \tag{B.7}$$

By requiring $W(\lambda, \mu, \infty) = \eta W_0(\infty)$, it follows that

$$\mu = \sqrt{\eta/\lambda}. \tag{B.8}$$

It is easy to show that such a choice of $\mu$ also leads to

$$\int_0^\infty |A_\lambda(\omega)|^2\, d\omega = \eta \int_0^\infty |A_0(\omega)|^2\, d\omega. \tag{B.9}$$

That is, the areas under the Fourier spectra of $a(t, \lambda, \mu)$ is equal to that of $\eta a_0(t)$. Numerical experimentation seems to indicate that the intensity of structural response under ground motions generated according to this criterion is less equal than the spectrum criterion. This thesis uses the spectrum criterion.

# Bibliography

[1] V. V. Bertero, J. C. Anderson, and H. Krawinkler, "Performance of Steel Building Structures During the Northridge Earthquake," Report No. UBC/EERC-94/09, Earthquake Engineering Research Center, University of California, Berkeley, August 1994.

[2] W. T. Holmes and P. Somers, eds., *Earthquake Spectra*, ch. 2. Earthquake Engineering Research Institute, Jan. 1996. Northridge Earthquake Reconnaissance Report, Vol. 2, Supplement C to Volume 11.

[3] R. G. Black, W. A. B. Wenger, and E. P. Popov, "Inelastic Buckling of Steel Struts Under Cyclic Load Reversals," Report No. UBC/EERC-80/40, Earthquake Engineering Research Center, University of California, Berkeley, October 1980.

[4] S.-J. Lee and L.-W. Lu, "Quasi-Static Tests of Scaled Model Building," *Journal of Structural Engineering, ASCE*, vol. 115, no. 8, pp. 1895–1916, 1989.

[5] C. W. Roeder, "Seismic Behavior of Concentrically Braced Frame," *Journal of Structural Engineering, ASCE*, vol. 115, no. 8, pp. 1837–1856, 1989.

[6] C.-M. Uang and V. V. Bertero, "Earthquake Simulation Tests and Associated Studies of a 0.3-Scale Model of a Six-Story Concentrically Braced Steel Structure," Report No. UBC/EERC-86/10, Earthquake Engineering Research Center, University of California, Berkeley, December 1986.

[7] M. Wakabayashi, T. Nakamura, and N. Yoshida, "Experimental Studies on the Elastic-Plastic Behavior of Braced Frames Under Repeated Horizontal Loading, Part 1," in *Bulletin of the Disaster Prevention Research Institute*, vol. 27, Part 3, No. 251, pp. 121–154, Kyoto University, 1977.

[8] H. Yamanouchi, M. Midorikawa, I. Nishiyama, and M. Watabe, "Seismic Behavior of Full-Scale Concentrically Braced Steel Building Structure," *Journal of Structural Engineering, ASCE*, vol. 115, no. 8, pp. 1917–1929, 1989.

[9] Y. Yamazaki, M. Nakashima, and T. Kaminosono, "Reliability of Pseudodynamic Test in Earthquake Response Simulation," *Journal of Structural Engineering, ASCE*, vol. 115, no. 8, pp. 2098–2112, 1989.

[10] J. F. Hall and V. R. M. Challa, "Beam-Column Modeling," *Journal of Engineering Mechanics, ASCE*, vol. 121, no. 12, pp. 1284–1291, 1995.

[11] V. R. M. Challa and J. F. Hall, "Earthquake Collapse Analysis of Steel Frames," *Earthquake Engineering and Structural Dynamics*, vol. 23, pp. 1199–1218, 1994.

[12] V. V. Bertero, et al., "Seismological and Engineering Aspects of the 1995 Hyogoken-Nanbu (Kobe) Earthquake," Report No. UBC/EERC-95/10, Earthquake Engineering Research Center, University of California, Berkeley, November 1995.

[13] "The January 17, 1995 Kobe Earthquake: An EQE Summary Report." EQE International, April 1995.

[14] O. F. Hassan, *Modeling of Bracing Members and Seismic Behavior of Concentrically Braced Steel Structures*. Ph.D. thesis, University of Michigan, 1991.

[15] V. A. Zayas, P. B. Shing, S. A. Mahin, and E. P. Popov, "Inelastic Structural Modeling of Braced Offshore Platforms for Seismic Loading," Report No. UCB/EERC-81/04, Earthquake Engineering Research Center, University of California, Berkeley, January 1981.

[16] Y. Ghanaat, "Study of X-Braced Steel Frame Structures Under Earthquake Simulation," Report No. UBC/EERC-80/08, Earthquake Engineering Research Center, University of California, Berkeley, April 1980.

[17] M. Midorikawa, I. Nishiyama, and H. Yamanouchi, "Analytical Evaluation of K-Braced Structure Seismic Test," *Journal of Structural Engineering, ASCE*, vol. 115, no. 8, pp. 1930–1948, 1989.

[18] L. S. Wijanto, P. J. Moss, and A. J. Carr, "The Seismic Behavior of Cross-Braced Steel Frames," *Earthquake Engineering and Structural Dynamics*, vol. 21, pp. 319–340, 1992.

[19] T. Fukuta, I. Nishiyama, H. Yamanouchi, and B. Kato, "Seismic Performance of Steel Frames With Inverted V Braces," *Journal of Structural Engineering, ASCE*, vol. 115, no. 8, pp. 2016–2028, 1989.

[20] F. Perotti and G. P. Scarlassara, "Concentrically Braced Steel Frames Under Seismic Actions: Non-Linear Behavior and Design Coefficients," *Earthquake Engineering and Structural Dynamics*, vol. 20, pp. 409–427, 1991.

[21] T. Nonaka, "An Elastic-Plastic Analysis of a Bar Under Repeated Axial Loading," *International Journal of Solids and Structures*, vol. 9, no. 5, pp. 569–580, 1973. erratum in No. 10, p. 569.

[22] M. Shibata, T. Nakamura, N. Yoshida, S. Morino, T. Nonaka, and M. Wakabayashi, "Elastic-Plastic Behavior of Steel Braces under Repeated Axial Loading," in *Proceedings of the 5th World Conference on Earthquake Engineering*, (Rome), pp. 845–848, 1973.

[23] K. Ikeda and S. A. Mahin, "Cyclic Response of Steel Braces," *Journal of Structural Engineering, ASCE*, vol. 112, no. 2, pp. 342–361, 1986.

[24] T. Fujiwara, "Seismic Behavior of Inelastic Members of Braced Frame Structure," in *Proceedings of the 7th World Conference on Earthquake Engineering*, (Istanbul), pp. 241–248, 1980.

[25] J. F. Hall, "Optimum Use of Panel Zones in Seismic Design of Tall Steel Frames," Report for the CUREe-Kajima Research Project, California Institute of Technology, Pasadena, January 1993.

[26] V. R. M. Challa, "Nonlinear Seismic Behavior of Steel Planar Moment-Resisting Frames," Report No. 92-01, *Earthquake Engineering Research Laboratory, California* Institute of Technology, Pasadena, June 1992.

[27] F. Aslani and S. C. Goel, "Stitch Spacing and End Fixity in Seismic-Resistant Boxed Angle Braces.," *Journal of Structural Engineering, ASCE*, vol. 118, no. 10, pp. 2872–2889, 1992.

[28] M. Wakabayashi, T. Nakamura, and N. Yoshida, "Experimental Studies on the Elastic-Plastic Behavior of Braced Frames Under Repeated Horizontal Loading, Part 2," in *Bulletin of the Disaster Prevention Research Institute*, vol. 29, Part 3, No. 264, pp. 99–127, Kyoto University, 1980.

[29] T. K. Caughey, "Classical Normal Modes in Damped Linear Dynamic Systems," *Journal of Applied Mechanics*, vol. 27, pp. 269–271, 1960.

[30] J. M. Ricles and E. P. Popov, "Inelastic Link Element for EBF Seismic Analysis," *Journal of Structural Engineering, ASCE*, vol. 120, no. 2, pp. 441–463, 1994.

[31] P. D. Moncarz and H. Krawinkler, "Theory and Application of Experimental Model Analysis in Earthquake Engineering," Report No. 50, John A. Blume Earthquake Engineering Center, Stanford University, Stanford, California, June 1981.

[32] P. C. Jennings, G. W. Housner, and N. C. Tsai, "Simulated Earthquake Motions," tech. rep., California Institute of Technology, Pasadena, 1968.

[33] C.-H. Loh and J.-C. Chang, "Cumulative Damage Parameters for Inelastic Systems Subjected to Earthquake Excitations: A Comparative Study," *Engineering Structures*, vol. 14, no. 3, pp. 152–162, 1992.

[34] J. Morrow, "Cyclic Plastic Energy and Fatigue of Metals," in *Internal Friction, Damping, and Cyclic Plasticity*, ASTM STP378, pp. 45–87, ASTM, 1965.

[35] V. V. Bertero, E. P. Popov, and H. Krawinkler, "Beam-Column Sub-Assemlages Under Repeated Loading," *Journal of Structural Engineering, ASCE*, vol. 98, pp. 1137–1159, May 1972.